TECHNISCHE UNIVERSITÄT WIEN

MASTER THESIS

Drone-based Investigations on Emissions of Biogenic Aerosols relevant for Heterogeneous Ice Nucleation

carried out at the

Institute of Materials Chemistry
TU Wien

under the supervision of

Univ.Prof. Dipl.-Chem. Dr.rer.nat. Hinrich Grothe

by

Paul Bieber, BSc
[redacted]

Vienna, 21.06.2021

DIPLOMARBEIT

Drohnen-gebundene Messungen biogener Aerosol-Emissionen relevant für heterogene Eis-Nukleation

ausgeführt am

Institut für Materialchemie
Technischen Universität Wien

unter der Anleitung von

Univ.Prof. Dipl.-Chem. Dr.rer.nat. Hinrich Grothe

durch

Paul Bieber, BSc
[redacted]

Wien, 21.06.2021

Eidesstattliche Erklärung: Ich erkläre hiermit an Eides statt, dass ich die vorliegende Arbeit selbstständig verfasst, andere als die angegebenen Quellen/Hilfsmittel nicht benutzt, und die den benutzten Quellen wörtlich und inhaltlich entnommenen Stellen als solche kenntlich gemacht habe.

Statutory declaration: I hereby declare that I have authored this thesis independently, that I have not used other than the declared sources/resources, and that I have explicitly marked all material which has been quoted either literally or by content from the used sources.

Abstract

Climate change is the result of physicochemical reactions taking place in the Earth's atmosphere. In contrast to greenhouse gases, the influence of aerosols on weather and climate is still associated with large uncertainties. Several aerosols particles can act as ice nuclei (IN) that trigger freezing of supercooled liquid droplets in atmospheric clouds. The resulting ice- and mixed-phase clouds have different albedo compared to liquid ones. Moreover, cloud glaciation leads to hydrological events (e.g., rainfall, snowfall, hail) and thus, shortens the lifetime of atmospheric clouds. Many IN with high characteristic freezing temperatures originate from biological organisms. Pollen grains, fungal spores and bacterial cells are examples of IN that can get airborne as biogenic aerosols (bioaerosols) and influence cloud processes in the troposphere. Indeed, most biological processes are highly complex and so is the bioaerosol formation. Flowering of blooming plants, humidity induced sporulation of fungi and wet bioaerosol generation during rainfall are three of many possible pathways of how biogenic IN are emitted from the land surface to the troposphere. Research on bioaerosol detection with ground-based and aircraft-assisted measurements has been established in the last decades. However, there is a big knowledge gap on the emission and transport of bioaerosol in the airspace above the land surface and below the aircraft sampling height. These emission-fluxes, and their seasonal and spatial variability, are absolutely essential to include the influence of bioaersols in model studies on climate change. To create experimental data, we developed a drone-based aerosol particles sampling impinger/impactor (DAPSI) system that can be attached to small scale drones in order to analyze bioaerosols right above the emission sources and its transport to higher altitudes. DAPSI samples aerosol particles *in-situ* with an impinger and a cascade impactor and thus allows further investigation of the ambient aerosol using freezing assays, fluorescence- and scanning electron microscopy in the laboratory. Furthermore, it monitors temperature, relative humidity, air pressure and particulate matter concentrations (PM_{10} and $PM_{2.5}$) with onboard sensors directly at the sampling spot. The impinger sampling unit was characterized with standardized aerosols (polystyrene latex spheres) and biogenic IN (*Betula pendula*). First test flights of the system were carried out during a field campaign in an alpine remote environment (Gosau, Austria, Europe). A bloom of IN in the vicinity of vegetation was observed after rainfall with concentrations around 10^3 L^{-1} active above -24°C. The emission was linked to several bioaerosols which contained IN in the nanoscale. Results point to high variability of bioaerosol emissions and the potential atmospheric influence. DAPSI is a ground-breaking tool to measure aerosol emissions and prepare experimental data for climate research.

Kurzfassung

Der Klimawandel resultiert aus physikochemischen Reaktionen, welche in der Atmosphäre stattfinden. Im Gegensatz zu den Treibhausgasen ist der Einfluss von Aerosolen auf das Klima weitgehend unklar. Verschiedene Aerosol-Partikel können in unterkühltem Wasser in troposphärischen Wolken Eisbildung auslösen. Dadurch entstehen Eis- und Mischphasenwolken mit einem unterschiedlichen Rückstrahlvermögen im Vergleich zu flüssigen Wolken. Weiters werden hydrologische Vorgänge (z.B. Regen, Hagel, Schneefall) oft auf Grundlage eines Gefrierprozesses ausgelöst. Viele hoch-aktive Eiskeime (EK) stammen aus biologischen Quellen. Zum Beispiel können biologische Aerosole (Bioaerosole) wie etwa Pollenkörner, Pilzsporen oder bakterielle Zellen Wolkenprozesse in der Troposphäre beeinflussen. Der Einfluss von Bioaerosolen auf Wetter und Klima ist nicht vollständig erforscht, da die Konzentrationen regional und saisonal stark variieren können. Die Blütezeit von Pflanzen, die feuchtigkeitsausgelöste Sporenbildung der Pilze, sowie die feuchte Bioaerosol-Entstehung während starker Niederschläge sind drei mögliche Pfade über welche biologische EK in die Troposphäre gelangen können. Jedoch ist die Bioaerosol-Formation ein sehr komplexer Prozess der neben physikalischen auch von biologischen Parametern abhängt. Da sich die Forschung auf Grundlage von bodengebundenen sowie Flugzeuggetragenen Messungen von Bioaerosolen entwickelt hat, existiert nach wie vor eine große Wissenslücke über die Emission und den Transport von Bioaerosolen im Luftraum zwischen den Bodenstationen und den niedrigsten Flughöhe der Flugzeuge. Um diese Lücke zu schließen haben wir ein Drohnen-gebundenes Aerosol-Partikel Sammel Impinger/Impaktor (DAPSI) System entwickelt, welches an kleinen herkömmlichen Drohnen befestigt werden kann und somit die Analyse von Bioaerosolen über den Quellen und den Transport in höhere Lagen ermöglicht. Mithilfe eines Impingers und eines Impaktors werden Aerosol-Partikel *in-situ* gesammelt und anschließend im Labor untersucht (d.h. Gefrierexperimente sowie Fluoreszenz und Raster-Elektronen Mikroskopie). Weiters werden meterologische Parameter sowie die Feinstaubkonzentration während des Fluges mithilfe einer eingebauten Sensorik aufgezeichnet. Der verwendete Impinger wurde im Labor mit Standard-Aerosolen (Polystyren Latex Kugeln) sowie biologischen EK (*Betula pendula*) charakterisiert. Die ersten Testflüge in den österreichischen Alpen (Gosau) verliefen erfolgreich. Die Emission von EK war nach Regenfällen besonders hoch (10^3 L^{-1} aktiv über -24°C) und konnte über mikoroskopische Analysen in Verbindung mit Bioaerosolen gebracht werden. DAPSI ist ein bahnbrechnendes Gerät für die Analyse von spezifischen Bioaerosol Emissionen, welches experimentelle Daten für die Klimaforschung liefern kann.

Preface

This Master thesis was supervised by Univ. Prof. Dr. Hinrich Grothe and carried out at the Technical University of Vienna (TU Wien). Results from the tool building and validation process and from the first field measurements in June 2019 were published in the following paper:

> P. Bieber, T. M. Seifried, J. Burkart, J. Gratzl, A. Kasper-Giebl, D. G. Schmale III, and H. Grothe. *A drone-based bioaerosol sampling system to monitor ice nucleation particles in the lower atmosphere.* Remote Sensing, 12(3):552, 2020.

The focus of that paper is led on technical details of the sampling methodology using rotary-wing drones as platforms. A follow-up paper focusing on the results from the second field campaign in August 2019 and a deeper characterization of the ambient aerosol was published by my colleague Teresa M. Seifried:

> T. M. Seifried, P. Bieber, A. T. Kunert, D. G. Schmale III, K. Whitmore, J. Fröhlich-Nowoisky, and Hinrich Grothe. *Ice nucleation activity of alpine bioaerosol emitted in vicinity of a birch forest.* Atmosphere, 12(6):779, 2021.

This paper focuses on the identification of biogenic aerosols emitted from birch surfaces inducing heterogeneous ice nucleation. The present thesis is based on the results of the published papers. Every adapted figure and text passage is cited properly. Overall, Teresa M. Seifried, was responsible for the management of the field campaigns, controlling a drone during the measurements, recording data during the campaigns, microscopic analytics, data acquisition and the writing of the second manuscript. I was responsible for the tool building process of the sampling setup, the validation process, controlling a drone during the measurements, the freezing assays, data acquisition and the writing of the first manuscript. In general, most parts of the presented work were carried out as a team. The term "we" always refers to the whole team, originating from the working group of Prof. Grothe and others. Therefore, many colleagues contributed to the results presented in this Master thesis. They are acknowledged in the following.

Acknowledgments

I would like to thank:

Univ. Prof. **Hinrich Grothe** for supervising me during my Master thesis, for reading and correcting this thesis and for his commitment to support young students during their early carrier. Especially for supporting me to present this study on two conferences in Boston, Massachusetts, USA (3rd Atmospheric Ice Nucleation Conference and American Meteorological Society 100th Annual Meeting) and online at the General Assembly 2020 of the European Geosciences Union (EGU2020).

Teresa M. Seifried for supervising me during my studies, for her motivation during work-intensive times and for sharing an ongoing interest in science related to physical-chemistry, environmental science and climate research with me.

Anna T. Kunert and **Janine Fröhlich-Nowoisky** from the Max Planck Institute for Chemistry, Department of Multiphase Chemistry, for their excellent input in cooperations, especially for measuring ice nucleation activity with their self-built freezing assay.

Prof. **Anne Kasper-Giebl** from the Institute of Chemical Technologies and Analytics, for contributing her knowledge in sampling and analyzing aerosols and for sharing the cascade impactor with our working group.

Prof. **David G. Schmale III** from the Virginia Tech University, School of Plant and Environmental Science for sharing his expertise in microbiology and in sampling aerosols with rotary-wing drones. Furthermore, for sharing his drones with our working group.

Julia Burkart and **Jürgen Gratzl** from the University of Vienna, Aerosol Physics and Environmental Physics, for assisting in the characterization of the self-built setup and for sharing their knowledge in bioaerosol science.

Karin Whitmore and the other members of USTEM (University Service center for Transmission Electron Microscopy) for assisting in scanning electron microscopy.

Vera Truttmann for providing the LaTeX template which was used to write this thesis.

Florian Kleissner for his technical advice regarding electronic equipment during tool building periods.

David Stinglmayr, **David Wimberger**, **Fung-Yee Poon**, **Deborah Steiner** and **Florian Reyzek** for assisting in laboratory work and field research.

Phillip Baloh for training lessons to fly drones and his contribution to research on ice nucleation.

Ayse Koyun, **Stefan Werkovits**, **Isatis Cintron** and **Johannes Mirwald** for interesting discussions during coffee breaks and party evenings.

My family for supporting me during my scientific carrier, especially my grandparents for their educational input during my childhood which led to an increasing interest in nature related science and technical engineering.

Diese Arbeit widme ich meiner Großmutter Gertrude Bieber.

Contents

1. Introduction

1.1. A Brief History of Aerosol-Cloud Interactions Research

"The sun, moving as it does, sets up processes of change and becoming and decay, and by its agency the finest and sweetest water is every day carried up and is dissolved into vapour and rises to the upper region, where it is condensed again by the cold and so returns to the earth. This, as we have said before, is the regular course of nature."

Aristotle, Meteorology, 350 B.C.

Until the early 20th century, only water molecules were considered as relevant in atmospheric cloud processes. In 1943, Vincent J. Schaefer (Figure 1.1, A), investigated the formation of ice in supercooled water droplets induced by foreign particles for the first time. He developed a cloud chamber which was a simple isolated box with black painted walls. A liquid cloud was produced very uncomplicated by cooling the box and placing in a moister cloth or by breathing out air into the box. After throwing tiny particles of dry ice into the chamber, supercooled water droplets started to freeze, resulting in an ice cloud (Figure 1.1, B). Thereafter, ice crystals grow and fall to the ground [1]. Based on that discovery, Schaefer and his college, Bernard Vonnegut started to study several aerosols interacting with supercooled water droplets [2].

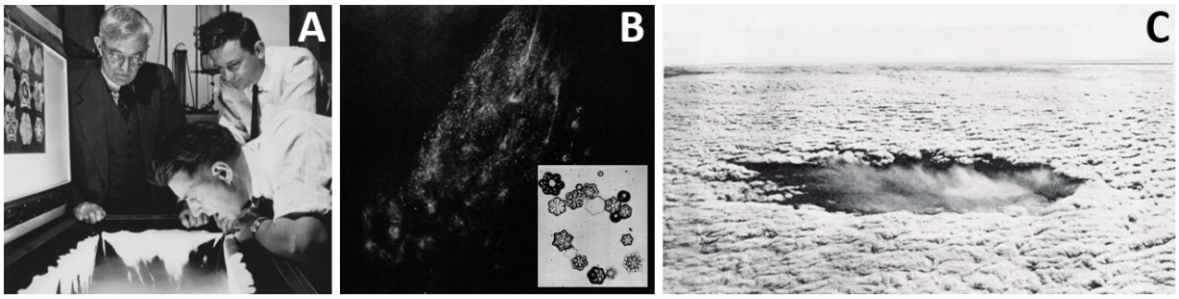

Figure 1.1.: Historical images: A) Irvin Langmuir, Vincent J. Schaefer and Bernard Vonnegut at their first ice nucleation experiments [a], B) light scattering on an ice cloud formed in the cloud chamber after inserting dry ice, adapted from [1], C) picture of a seeded cloud from above [b].

[a] Picture adapted from `https://mettech.cl/en/biblioteca/cloud-seeding-history/` downloaded on October 29th, 2020.

[b] Picture adapted from `http://www.nawcinc.com/photopages/SeedingEffects.htm` downloaded on October 29th, 2020.

In interest for military and agricultural usage (e.g., prevention of aircraft icing and elimination of thunderstorms producing hail), Vonnegut and Schaefer developed techniques for cloud seeding, a process whereat foreign particles (e.g., dry ice or silver iodide) are suspended in a selected cloud by dropping the particles of an aircraft [2, 3]. Thereafter, ice nucleation is triggered in supercooled cloud droplets, resulting in precipitation as seen in Figure 1.1, C [2]. In the 1950s, water resource manager recognized that cloud-seeding had the potential to be used in a weather-modifying way. More precise, seeding of wintertime clouds in mountainous areas could lead to more snowfall and therefore increase the water supply of an arid region [4]. Since cloud seeding experiments proliferated all around the globe, the necessity of understanding the scientific basis of cloud microphysics, especially ice nucleation, started to grow. One of the first approaches to understand freezing of supercooled water induced by aerosol particles, from a theoretical point of view, was presented by Neville H. Fletcher in a Faraday discussion paper [5]. In interest for artificial cloud seeding, but also in understanding natural cloud-processes, Fletcher proposed that size, molecular aspects and surface imperfections of aerosol particles contribute to their activity in ice nucleation. Later, Fletcher introduced the theory of active sites, whereat conical pits on the surface of aerosol particles are taken into consideration when explaining nucleation with mathematical models [6]. With the knowledge that some particles nucleate ice better than others, the question arised what aerosols play important roles in natural cloud-processes and what ice nuclei (IN) can be used instead of silver iodide for cloud seeding. It was in the early 70s when Russel C. Schnell and Gabor Vali discovered IN from decomposing vegetation and hence proposed a new world-wide source for atmospheric IN [7, 8]. Further investigations explained the IN to be a protein produced by the bacteria *Pseudomonas syringae* for survival benefits [9–11]. Beside *Pseudomonas syringae*, that was also used as a commercial product (Snowmax©) for snow-production in skiing areas, many other atmospheric IN were discovered over the last decades. For instance, soot, Sahara dust, volcanic ash and various biological particles (e.g., pollen, fungal spores or algae) turned out to nucleate ice at atmospheric conditions in supercooled droplets [12]. Taking into account that several aerosols are present in the atmosphere in spatial and temporal distribution and act as IN in a microphysical behavior, models can be introduced to calculate the influence of aerosols on weather and climate on a large scale. To do so, the number of IN present in the atmosphere has to be predicted first. Thereafter, it has to be included in fine-scale models that calculate aerosol-cloud interactions. Finally, the results can be expanded to larger scales and explain the climate of the future. This ongoing work started by Fletcher in the year 1962 [13], continued by William A. Cooper, 1986 [14], Michael P. Meyers et al., 1992 [15], and lasts until today with the models described by Paul J. DeMott et al., 2010 [16], John H. Seinfeld et al., 2016 [17] and others. Even though the knowledge about ice nucleation in clouds developed over almost 80 years, many questions remain unanswered. Most of which are highly related to climate change and include scientific and ethic thematic (e.g., the role of several aerosols in global warming, seasonal and spatial alteration of IN concentrations, weather modification to avoid dry-periods, etc.).

1.2. Atmospheric Processes

"One meteorologist remarked that if the theory were correct, one flap of a sea gull's wings would be enough to alter the course of the weather forever. The controversy has not yet been settled, but the most recent evidence seems to favor the sea gulls."

- Edward N. Lorentz, 1963, [18].

Indeed the Earth's atmosphere is a rather chaotic and complex system that includes many variables that make calculations of weather and climate challenging. However, with increasing computing power and scientific data, weather forecasts get better and predictions for climate become more reliable. To understand our atmosphere from a physical and chemical point of view, it can be seen as limited system similar to a common reaction flask from a chemistry laboratory (as drawn in Figure 1.2). Solar radiation is the driving energy source; gas molecules, cloud water and aerosol particles are the reactants; wind and convection is the stirring bar; and the resulting weather is the product [19]. Observing the weather over a longer time period yields the climate as end result. In this reaction system, the activities that take place in tropospheric clouds, are from high interest for atmospheric research. In dependency on its phase state, water in clouds scatters incoming and outgoing radiation and thus, can have cooling or heating effects to the planet [20]. Moreover, precipitation in any form (e.g., rain, hail, snowfall, graupel) is always the result of cloud-processes (i.e., cloud condensation and ice nucleation), which often involve foreign aerosol particles [17]. Therefore, a detailed view on the atmosphere and the reactions that take place in clouds involving aerosol particles is given in this chapter.

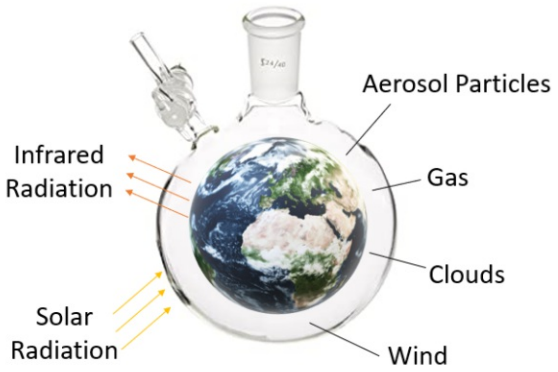

Figure 1.2.: The *reaction flask* of an atmospheric chemist.

1.2.1. The Earth's Atmosphere

Gas molecules and atoms above the surface of the Earth create the atmosphere of our planet. The pressure $p(h)$ of those gases decreases exponentially with increasing altitude h as described by the barometric formula

$$p(h) = p_0 exp(-\frac{Mg}{RT}h) \tag{1.1}$$

where p_0 is the pressure at ground level, M is the molecular weight of atmospheric gases, g the gravitational acceleration (9.807 m s^{-2}), R is the universal gas constant (8.314 J K^{-1} mol^{-1}) and T is the given temperature. Due to the defined pressure in each altitude and the interactions of atoms and molecules with radiation, a temperature gradient forms, which divides the atmosphere into several layers (see Figure 1.3, A). The varying average temperature is drawn as a black line in dependency of the distance from the Earth's surface (referred to as altitude). In the lowest layer, called **troposphere**, the temperature gradient has a linear dependency on the altitude. Starting from ground level, the temperature decreases with increasing height. In this region, warm air above the ground tends to expand due to the ideal-gas-law. Thus, the density gets lower and warm air streams to higher layers. This phenomenon, which is referred to as convection, leads to vertical mixing of gases and aerosols. In the **stratosphere**, the temperature gradient switches its direction leading to slow vertical mixing. After reaching the stratopause the gradient turns its direction again which leads to the **mesosphere**, where the layers are mixing rapidly in vertical direction. After reaching the coldest point of the atmosphere in the mesopause, the **thermosphere** begins. This layer is characterized by high temperatures since nitrogen and oxygen absorb solar radiation with short wavelength.[21]

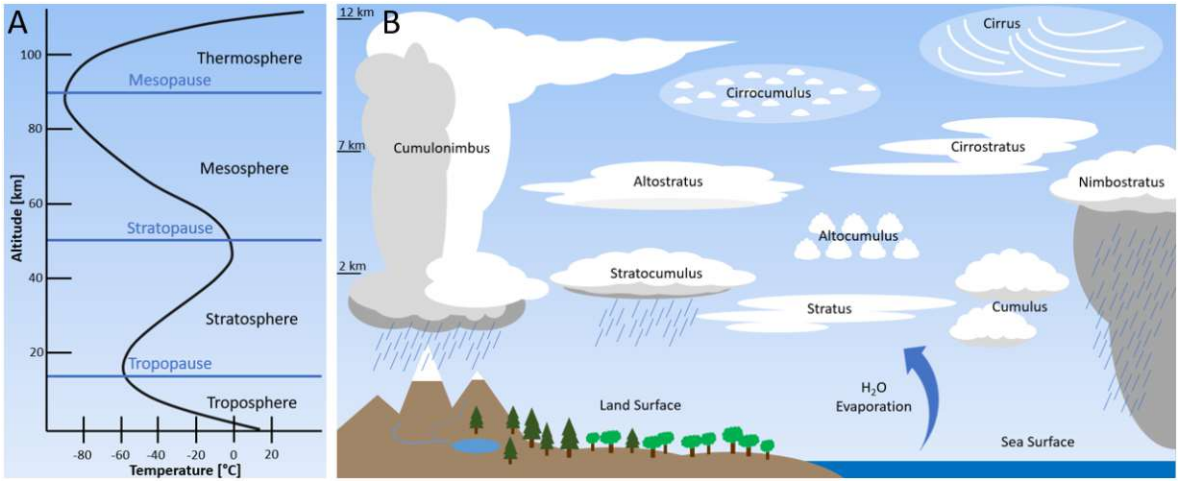

Figure 1.3.: A) The atmosphere and its layers in dependency of the altitude. Black line shows the temperature gradients through the layers. B) The troposphere and the hydrological cycle. Different forms of clouds are shown in dependency of the phase state and altitude.

Meteorology focuses on studies of the lower atmosphere (below 50 km of height). This regime enables the movement of water vapor from sea and land surfaces up to heights of

12 km due to convection. It can further be distinguished between the airspace were the movement of a flow is effected by the ground, referred to as planetary boundary layer (PBL), and above (free troposphere). In the PBL the air-stream is characterized by strong vertical mixing and turbulent changes of environmental parameters. In dependency on the pressure, temperature and presence of aerosols, water molecules change their phase state by adsorbing to a surface (i.e., condensation), evaporating from a liquid state, freezing, sublimating or thawing. Therefore, several types of clouds can be formed that are shown in Figure 1.3, B. The phase state of a cloud is from high importance for its light scattering properties and atmospheric lifetime. Clouds are characterized into four types, called low-level (**stratocumulus**, **stratus** and **nimbostratus**), mid-level (**altocumulus** and **altostratus**), high-level (**cirrus**, **cirrustratus** and **cirrocumulus**) and clouds with vertical development (**cumulus**, **cumulonimbus**) [22]. The most abundant cloud types are stratus, cumulus and cirrus clouds [22]. The development of a cloud starts from nucleation of vapor to liquid droplets and further nucleation to solid ice is resulting in ice or mixed-phase clouds. High focus in weather and climate modeling is given on the microphysical processes of cloud condensation and ice nucleation. Therefore, the nucleation process is explained from a thermodynamic basis in the following Section 1.2.2, cloud microphysics are described in the Sections 1.2.3 to 1.2.5, whereat the effects of ice and mixed-phase clouds on weather and climate are explained in Section 1.2.6.

1.2.2. Thermodynamic of Nucleation - A Theoretical Background

Homogeneous Nucleation

To describe atmospheric water and its phase transition (e.g., cloud condensation and ice nucleation), the laws of thermodynamics have to be taken into account. In a physical assumption, a defined volume of air from the atmosphere, including water (in any given phase states) and/or foreign substances (e.g., aerosol particles), is viewed as a theoretical system. According to the first law of thermodynamics the infinitesimal change of the inner energy, dU, of this given air parcel is defined by

$$dU = dQ + dW \tag{1.2}$$

where dW is the infinitesimal work that has been added to the parcel and dQ is the infinitesimal change of the heat. For a chemical reversible reaction, were $dQ_{rev} = TdS$ and $dW = -pdV$ is assumed, the first law of thermodynamics (1.2) can be modified as

$$dU = TdS - pdV + \sum_{i=1}^{k} \mu_i dn_i \tag{1.3}$$

where T is the temperature, dS the infinitesimal change of the entropy, p the pressure, dV the infinitesimal change of the volume, μ_i the chemical potential ($\mu_i = \frac{dG}{dn_i}$) of the component i

and dn_i the change of the mole number of i. Considering a chemical reaction taking place, the definition of the infinitesimal change of Gibbs free energy dG is given by the total differential

$$dG = -SdT + Vdp + \sum_{i=1}^{k} \mu_{\mathrm{i}} dn_{\mathrm{i}} \tag{1.4}$$

which describes the free energy change (absorbed or emitted) during the reaction that takes place in the air parcel. For a system with constant temperature and pressure, Equation 1.4 can be seen as

$$dG = \sum_{i=1}^{k} \mu_{\mathrm{i}} dn_{\mathrm{i}} \tag{1.5}$$

In case that only water molecules are present in the system (homogeneous reactions), only phases transitions can take place as stated by the following equations:

$$\mathrm{H_2O_{(g)}} \rightleftharpoons \mathrm{H_2O_{(l)}} \tag{1.6}$$

$$\mathrm{H_2O_{(l)}} \rightleftharpoons \mathrm{H_2O_{(s)}} \tag{1.7}$$

$$\mathrm{H_2O_{(g)}} \rightleftharpoons \mathrm{H_2O_{(s)}} \tag{1.8}$$

where the phase transition from gas to liquid (condensation) or solid (deposition) and the transition from liquid to solid (ice nucleation) is in focus for the formation and development of clouds. Those phase transitions have in common that a cluster of the new phase is formed at the beginning of the transition. This means, that n water molecules group and form a $\mathrm{H_2O}$ cluster that is the embryo for further growth of the new phase (the ice, liquid or gas phase).

$$(\mathrm{H_2O})_{\mathrm{n-1(cluster)}} + (m+1)\mathrm{H_2O_{(free)}} \rightleftharpoons (\mathrm{H_2O})_{\mathrm{n(cluster)}} + m\mathrm{H_2O_{(free)}} \tag{1.9}$$

For this reaction the Gibbs free energy which was defined in Equation 1.5 can be stated as

$$\Delta G = \mu_{cluster} \Delta n + \mu_{free} \Delta m \tag{1.10}$$

where $\mu_{cluster}$ is the chemical potential of the cluster that includes n molecules and μ_{free} is the chemical potential for free water molecules of the number m that can possible add to the cluster. Lets say that n water molecules are forming the cluster as shown in Equation 1.9, then $m = N_{start}$-n are the remaining water molecules in the free state, where N_{start} is the number of molecules at the beginning. Assuming that the cluster is from spherical shape, which is also true for water molecules in an ice cluster [23], the Gibbs free energy of the cluster formation can be defined. Therefore, the Gibbs free energy is a sum of mg_{free}, $ng_{cluster}$ and the surface energy of the cluster ($4\pi r^2 \sigma$), while the Gibbs free energy of the free molecules at the beginning of the reaction is $N_{start} g_{free}$ which leads to

$$\Delta G = mg_{free} + ng_{cluster} + 4\pi r_n^2 \sigma - N_{start} g_{free} \tag{1.11}$$

where g_{free} is the Gibbs energy for one free molecule, $g_{cluster}$ is the Gibbs energy for one molecule in the cluster, r_n is the radius of the cluster containing n molecules and σ is the surface tension. By substituting $m = N_{start} - n$, Equation 1.11 can be rewritten as

$$\Delta G = n(g_{cluster} - g_{free}) + 4\pi r_n^2 \sigma \tag{1.12}$$

For a spherical cluster the number of molecules is given by

$$n = \frac{4\pi r_n^3}{3\upsilon_{cluster}} \tag{1.13}$$

where $\upsilon_{cluster}$ is the volume which is consumed by one water molecule in the cluster. By using Equation 1.4 and assuming constant temperature and the volume to be ideal ($\upsilon = \frac{kT}{p}$) the difference of the Gibbs free energies for the molecules can be seen as $-kT \int \frac{dp}{p}$, where k is the Boltzmann constant. The integral yields the natural logarithm of the saturation, $S = \frac{p_{free}}{p_{cluster}}$, and thus the context can be stated as

$$g_{cluster} - g_{free} = -kT \ln(S) \tag{1.14}$$

Inserting 1.13 and 1.14 in 1.12 results in the **classical nucleation theory**, which was introduced by Volmer and Weber, 1926; Farkas, 1927; Becker and Döring, 1935; and others [24–26].

$$\Delta G = 4\pi r_n^2 \sigma - \frac{4\pi r_n^3}{3\upsilon_{cluster}} kT \ln(S) \tag{1.15}$$

This equation, which is based on an equilibrium assumption, can be used to describe phase transitions from water vapor to condensed water droplets (cloud condensation), from liquid water droplets to ice crystals (ice nucleation) in the atmosphere, or from several gas-molecules to nucleation-mode aerosols. The first term ($4\pi r_n^2 \sigma$) is often referred to as surface term (ΔG_S) while the second term ($-\frac{4\pi r_n^3}{3\upsilon_{cluster}} kT \ln(S)$) is referred to as volume term (ΔG_V). For $S < 1$ the volume term becomes positive and therefore no nucleation can take place. However at supersaturation ($S > 1$) the volume term is negative. This means that for small radii the positive surface term is dominating the equation, while for larger radii (i.e., larger clusters) the volume term, becomes the dominated part. In Figure 1.4 this relation is visualized.

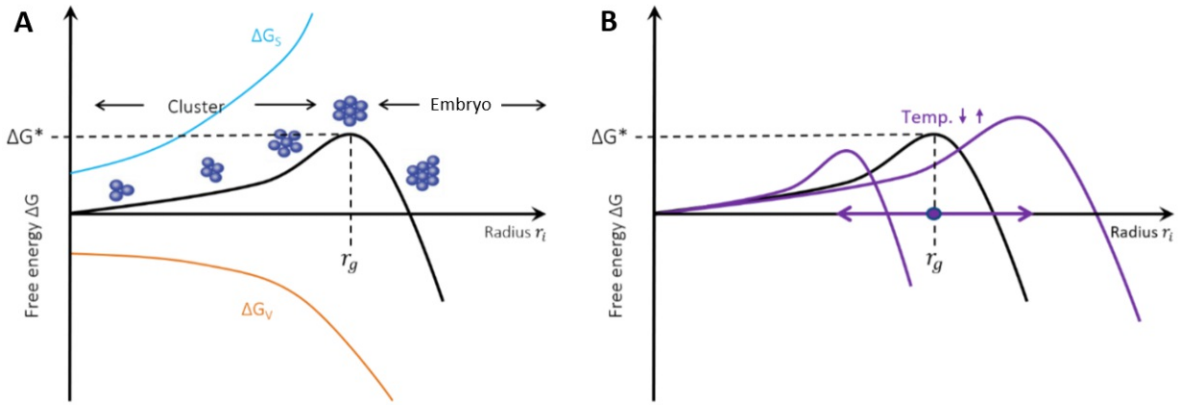

Figure 1.4.: Visualization of the classical nucleation theory for $S > 1$: A) surface term (blue line) volume term (orange line) and the Gibbs free energy (black line) against the radius, B) temperature dependency.

As shown in Figure 1.4, A the cluster needs to reach a critical size to become an embryo (i.e. the stable origin of a solid or liquid phase). Thereafter, the phase can grow during diffusion. To define this critical diameter, r_g, the maximum of the curve is calculated by setting $\frac{\partial G}{\partial r} = 0$. Hence, the critical radius is defined by

$$r_g = \frac{2\sigma \upsilon_{cluster}}{kT \ln(S)} \tag{1.16}$$

The surface tension is indirect correlated to the given temperature, as known from the rule of Eötvös [27]. Thus, for higher temperatures the critical radius is larger while for lower temperatures the radius becomes smaller as seen in Figure 1.4, B. The Gibbs free energy at the point of the critical radius, (ΔG^*; i.e., the energy amount that has to be overcome for the reaction to take place) is given by

$$\Delta G^* = \frac{16\pi\sigma^3 \upsilon_{cluster}^2}{3(kT \ln(S))^2} \tag{1.17}$$

This equation can be seen as an explanation why meta-stable phases are preferable formed during a nucleation process, when they have a smaller surface tension than the stable form.

For a kinetic approach of explaining nucleation and its time dependency, the rate describing how many embryos form in a given time and space interval, referred to as nucleation rate is from interest. Therefore, an Arrhenius reaction velocity for the formation of clusters according to 1.9, can be stated by

$$\frac{dN_i}{dt} = \alpha_{i-1} N_{i-1}(t) - \beta_i N_i(t) - \alpha_i N_i(t) + \beta_{i+1} N_{i+1}(t) \tag{1.18}$$

where N_i its the number concentration of clusters containing i molecules, α is the forward, β is the backward reaction rate constant and t is the time. The equation explains the change of the number concentration as a sum of clusters with $i-1$ molecules getting larger plus

clusters of the size $i+1$ getting smaller minus clusters of the size i growing or shrinking. This dynamic system is visualized in Figure 1.5.

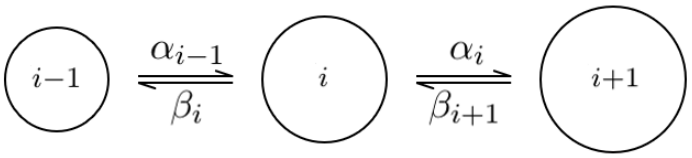

Figure 1.5.: Nucleation of a cluster with i molecules.

Hence, the nucleation rate, J, which can be seen as the reaction rate for the step from i to $i+1$, can be defined as

$$J = \alpha_i N_i - \beta_{i+1} N_{i+1} \tag{1.19}$$

At an equilibrium point e, the number of clusters, referred to as N_i^e, is given by a Boltzmann distribution as stated in

$$N_i^e = N_{free} \exp(\frac{-\Delta G_i}{kT}) \tag{1.20}$$

where N_{free} is the number of free molecules in the system and G_i is the Gibbs free energy of the cluster as explained above. The quantitative relation of the nucleation rate and the Gibbs free energy and the temperature can be stated as

$$J = A \exp(-\frac{\Delta G^*}{kT}) \tag{1.21}$$

according to Arrhenius. Thereby, A is a pre-exponential parameter and can be estimated by performing nucleation experiments.

Heterogeneous Nucleation

For heterogeneous nucleation, where a surface of a foreign particle is involved, the classical nucleation theory can be modified using a correction factor $\varphi < 1$ that is responsible to reduce the Gibbs free energy of the reaction. Thus the heterogeneous nucleation rate J_{het} can be stated as

$$J_{het} = A \exp(-\frac{\varphi \Delta G^*}{kT}) \tag{1.22}$$

with,

$$\varphi = \frac{(2+m)(1-m)^2}{4} \tag{1.23}$$

where m is the cosine of the contact angle that is given by the Young Equation

$$m = \cos\theta = \frac{\sigma_{SV} - \sigma_{SL}}{\sigma_{LV}} \tag{1.24}$$

Thereby, the contact angle, θ, is defined with the surface tensions between solid-vapor, σ_{SV}, solid-liquid, σ_{SL}, and liquid-vapor, σ_{LV}. In Figure 1.6, A, the contact angle between a particle and water is shown, while in B the reduced energy barrier is visualized.

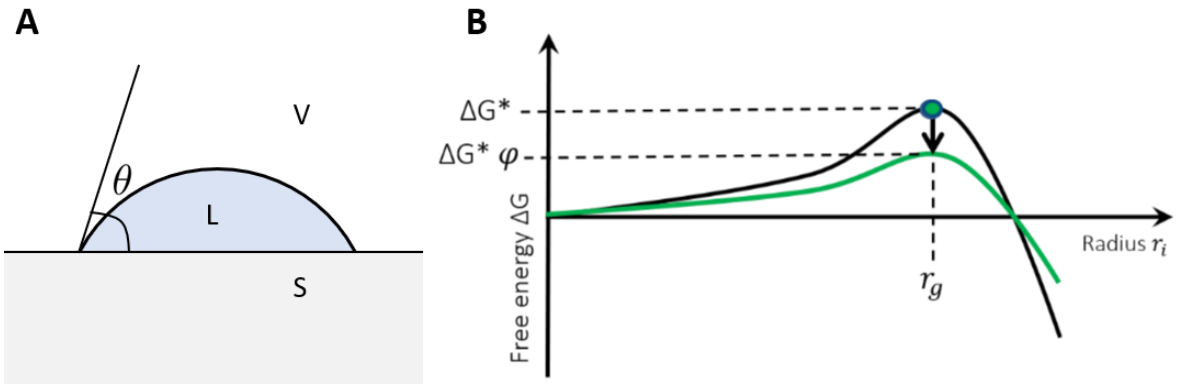

Figure 1.6.: Illustration of the modified classical nucleation theory for heterogeneous nucleation. A) Drawing of a liquid water droplet (L) on a solid surface (S) surrounded by vapor (V) showing a contact angle θ. B) Energy reduction of the Gibbs free energy for heterogeneous nucleation.

Even though most common theories developed to describe ice nucleation and cloud condensation are more complex than the contact angle theory, the idea of reducing the energy barrier, as in heterogeneous catalysis, stays valid for most nucleation theories. A detailed description on cloud condensation and ice nucleation is given below, where the focus is set to theories that explain heterogeneous freezing in the troposphere.

1.2.3. Cloud Condensation

Due to the kinetically hindered formation of a large cluster, relative humidity has to be above several hundreds of percentages and the temperature has to be below relevant tropospheric temperatures, for pure water to condensate without foreign substances [24, 26, 28] (i.e., homogeneous nucleation of water vapor). In clouds those parameters are not present at atmospheric conditions. However, water condensation takes place on so called cloud condensation nuclei (CCN) (i.e., heterogeneous nucleation of water vapor). At low temperature and relative humidity above 100% (supersaturation), water vapor starts to adsorb on solid surfaces of CCN. The ability of a particle to serve as CCN depends on its size, chemical composition and the local supersaturation.

Above a supersaturation of 400% every aerosol particle is able to serve as CCN [29]. Mostly, hygroscopic and polar substances tend to be strong CCN, condensing water at supersaturation below 1%. In the $\varkappa$-Köhler Theory a single hygroscopicity parameter is used to describe the ability of CCN to condense water at several supersaturations [30]. For instance κ=0.61 for $(NH_4)_2SO_4$, 1.28 for NaCl and 0.04 for α-pinene [30]. Generally, CCN are always present in our atmosphere in concentrations of about 10^2 to 10^3 cm^{-3}, measured at continental and marine environments [31]. In Figure 1.7 the general pathways of cloud mycrophysics are shown. When supersaturation at a given environment is high enough, water vapor forms droplets on the surface of CCN which can be either soluble or non soluble particles. Thus, clouds of liquid state appear in that environment. Depending on the altitude of the cloud, the condensed water can have a temperature above or below 0°C. If conditions are below 0°C, liquid droplets can turn into solid ice and thus, turn clouds into ice or mixed-phase clouds (cloud glaciation). This process can either take place with or without foreign particles, as described in Section 1.2.4 and 1.2.5.

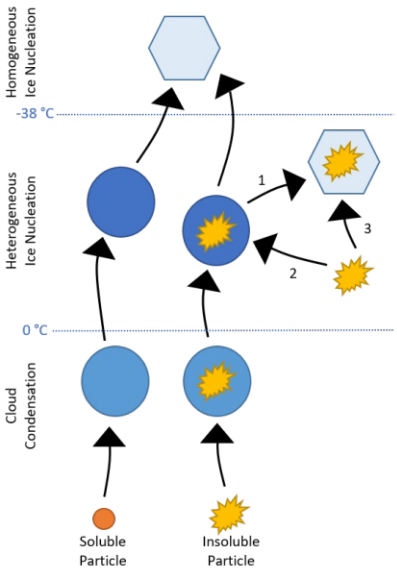

Figure 1.7.: Schematic illustration of cloud microphysics including cloud condensation, heterogeneouse ice nucleation (1: Immersion freezing, 2: Condensation freezing, 3: Deposition freezing) and homogeneouse ice nucelation.

1.2.4. Homogeneous Ice Nucleation

Homogeneous ice nucleation is referred to the phase transition from liquid to solid within the bulk of water. The phases are at an equilibrium at 0°C and atmospheric pressure (atm), as shown in the phase diagram of water (Figure 1.8, A, green dot). The phase diagram shows the typical anomalous properties of water, i.e. the pressure at the equilibrium between liquid

and ice decreases with increasing temperature. Due to the strong hydrogen bonds of water, the heat of fusion (333.55 J g^{-1}) and the surface tension is quite high (72.75 mN m^{-1}) [32]. Thus, the formation of a solid phase is based on the abundance of an ice embryo. This embryo evolves out of clusters as described above (Section 1.2.2) by the classical nucleation theory. Since the building of a critical cluster is limited kinetically, water droplets reach a supercooled state, i.e., a metastable liquid state. An example is given in Figure 1.8, A yellow dot). After a cluster reaches the critical nucleus size, the solid phase can grow on the embryo and the thermodynamically stable state occurs. During this process heat of fusion is released to the environment.

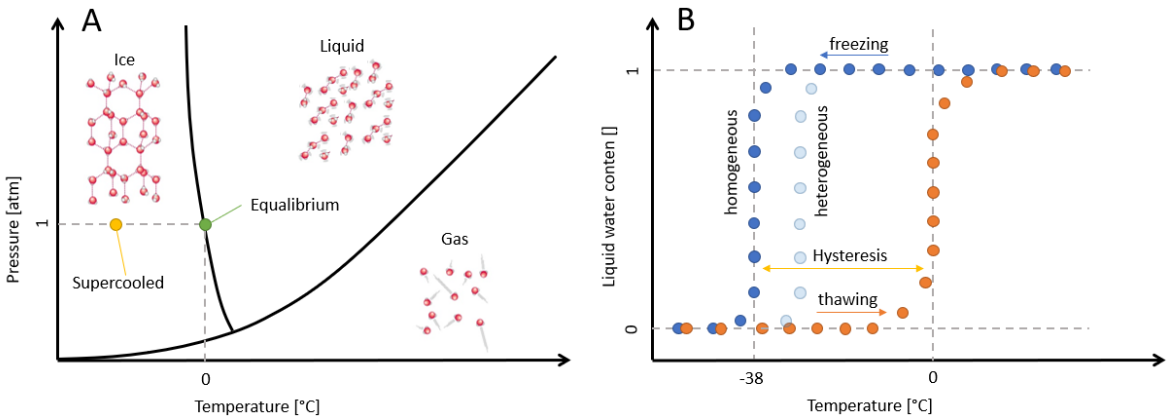

Figure 1.8.: A) Phase diagram of water and B) freeze-thawing hysteresis of an ensemble of water droplets.

For the freezing of an ensemble of N water droplets, the fraction of frozen droplets ($f_{ice} = \frac{n_{frozen}}{N}$) can be seen as a stochastic process where the time (t) and droplet volume (V) dependency can be stated as

$$f_{ice}(t, V) = 1 - exp(-J_{hom} V t) \tag{1.25}$$

where J_{hom} is the homogeneous nucleation rate as explained in Section 1.2.2 [12]. For parameters as found in a liquid cloud, the homogeneous freezing point is around -38°C [33]. Cooling the water droplets with a defined cooling rate would result in a freezing spectra as shown in Figure 1.8, blue dots. Reheating the same ensemble of water droplets would give a thawing spectra around 0°C, at the equilibrium point of water/ice, as indicated by the orange dots. A hysteresis that large (38°C difference) can be found when the volume of the individual water droplets is in the size of a few pL [33] since the probability of critical clusters formation is volume dependent (as seen in Equation 1.25). However, in atmopsheric clouds, IN are often present that induce heterogeneous ice nucleation and shift the freezing curve to a higher temperature (light blue dots).

1.2.5. Heterogeneous Ice Nucleation

Heterogeneous ice nucleation is referred to every freezing process that involves a foreign substance. As stated in Section 1.2.2, the involvement of a foreign substance can reduce the energy barrier and trigger nucleation at a higher temperature (see Figure 1.8, B). In general, four different modes of heterogeneous freezing in the atmosphere are known [34]:

1. **Deposition Freezing**: Involves an IN, whereat the ice crystal grows on the surface by re-sublimation as shown in Figure 1.7, path 3. This requires the environment to be supersaturated with respect to ice. However, new findings suggest that the condensation in pores and subsequent freezing (i.e., condensation freezing) occurs more likely during atmospheric transitions from water vapor to ice crystal than deposition freezing [35].

2. **Condensation Freezing**: Involves the condensation of supercooled liquid, often in a pore like structure of the IN (also referred to as pore condensation freezing). This mode is shown in Figure 1.7, path 2 plus path 1. The IN acts at first as CCN below 0°C and triggers the freezing process during the condensation process.

3. **Immersion Freezing**: Involves an immersed IN in the liquid phase as shown in Figure 1.7, path 1. The IN is therefore suspended in water at temperatures above 0°C and after the temperature reaches a defined subzero value, the freezing is triggered. This process is shown in Figure 1.8, B as light blue dots in comparison to homogeneous freezing as dark blue dots.

4. **Contact Freezing**: The immediate triggering of freezing during contact with foreign particles can be described as contact freezing. If those particles are ice, the freezing process is called secondary ice production.

In respect to the total number concentration of atmospheric aerosols, the number of IN is quite low. In most studies only one particle in one million aerosol particles tends to be an efficient IN [34]. To explain, why a particle acts as IN several theories have been developed. Classically, the particle has to be insoluble, expand a minimum size and fulfill several other requirements (i.e., chemical bond requirement, crystallographic requirement and active site requirement) [34]. The stochastic description as given for a homogeneous freezing event, stated in Equation 1.25, can be modified for immersion ice nucleation as

$$f_{ice}(s,t) = 1 - exp(-J_{het}st) \tag{1.26}$$

where J_{het} is the heterogeneous nucleation rate, as derived in Section 1.2.2, and s is the surface area of the immersed particle [12]. A detailed description on classical models is given in literature [12, 34]. From a chemical point of view, the freezing process is often referred to as time independent and the theory of active sites is taken into account. Assuming, that an IN nucleates ice at a given temperature and the time is of secondary importance, $J_{het}t$ can be substituted with $n_s(T)$ and the freezing process can be described as

$$f_{ice}(T) = 1 - exp(-n_s(T)s) \tag{1.27}$$

where $n_s(T)$ is the number of active sites per surface area triggering freezing at the temperature T (active site density) [12]. To explain what chemical requirements need to be fulfilled to build an active site, several concepts have been introduced. For example, Fukuta 1966, studied organic molecules and suggested that organic crystals tend to nucleate ice efficiently when they include (O-H)-groups with rotational symmetry [36]. Thus, the hydroxyl-groups can be fixed when pointing in the direction of the surface and therefore interact with water molecules in the liquid bulk. Moreover, it is stated that the geometry of the IN is from high importance, since the atoms on the surface of an IN can make up the crystallographic lattice of ice [34]. In a more detailed description Niedermeier et al., 2011 suggest the active sites to be spots on the IN similar to the black spots on a soccer ball [37]. In the soccer ball model both, the stochastic- and the time-independent active site theory, are included. For biological IN, the protein that nucleates ice of *Pseudomonas syringae* is studied very precisely. Kajava and Lindow, 1993, suggest the active site of the protein to be a large planar site that serves as a template for water molecules to orientate in an ice like lattice [38] as depict in Figure 1.9, A and B. This theory is expanded for biological macromolecules by Pummer et al., 2015. They suggest ice nucleating macromolecules to be templates for water molecules to orientate in an ice like structure as seen in Figure 1.9, C. These findings rule out the size and solubility criteria as stated above by classical theories explaining heterogeneous ice nucleation.

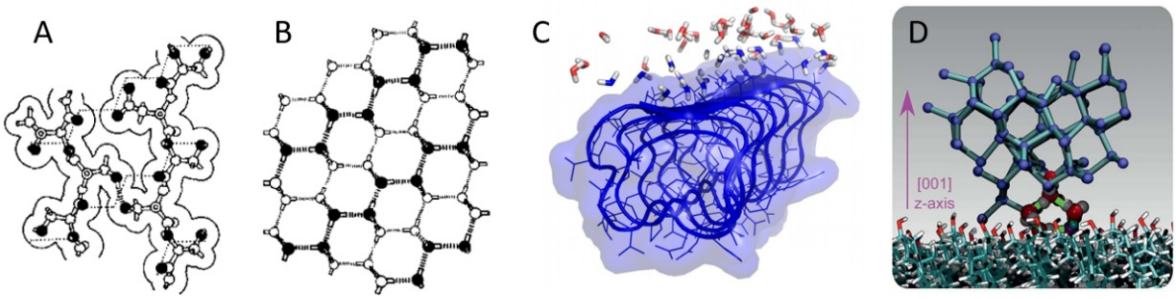

Figure 1.9.: Model studies for heterogeneous ice nucleation: A) Structure of the ice nucleating protein of *Pseudomonas Syringae* fitting the lattice structure of ice in B), figures adapted from [38]. C) Model of water molecules matching the nucleation site of an ice nucleating macromelcules, figure adapted from [39]. D) Model study of heterogeneous ice nucleation on cholesterol, showing cages formed out of water molecules and terminal hydroxyl groups. Figure adapted from [40].

The theory of matching ice like sites is turned upside down by new studies, for example of Sosso et al., 2018 [40]. Their model, regarding cholesterol as IN, shows that the surface is included in the formation of the cluster, rather than being just an ice-like template mimicking the lattice structure (see Figure 1.9, D). In more detail, the growth of the solid phase starts from molecular cages that involve water molecules and terminal hydroxyl groups of the surface from the cholesterol crystal. These cages include 5- and 6- bonded hydrogen rings that induce the formation of hexagonal or cubic ice.

1.2.6. Effects of Ice Nuclei in Clouds on Climate

As simplified in Figure 1.2, the energy budget of the planet Earth is the difference of the incoming solar radiation (SR) and the emitted radiation, which is (because of its common wavelength) referred to as infrared or long-wave radiation (LR). Besides atmospheric gases, aerosol particles and clouds interact with both, LR and SR. The interaction can have a high variety of different outcome, depending on the geometry of the particle and the wavelength of the radiation (see Figure 1.10).

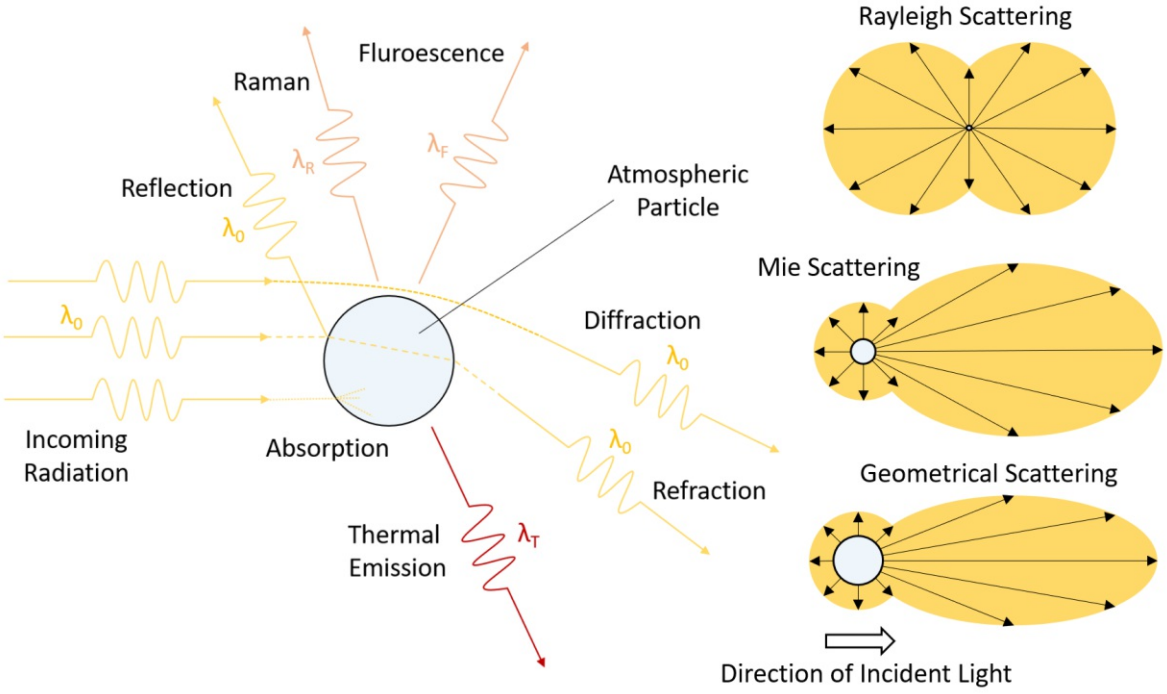

Figure 1.10.: Possible interaction of radiation with atmospheric particles.

The interactions can be divided into two main classes, namely elastic scattering (reflection, diffraction and refraction) and inelastic scattering (Raman-scattering and fluorescence) [41]. The elastic scattering procedure is highly relevant for the atmosphere, whereat the Mie-Theory can be taken into account to describe this physical process. Thereby, the parameter α is used to describe the nature of the scattering, as stated by

$$\alpha = \frac{D\pi}{\lambda} \tag{1.28}$$

where D is the diameter of the particle and λ is the wavelength of the radiation to be scattered. For $\alpha << 1$ (i.e., particles with a diameter much smaller than the wavelength of the incident light such as atoms of molecules) Rayleigh scattering is dominate, for $\alpha \approx 1$, the scattering is called Mie-scattering while for large particles with $\alpha >> 1$, geometrical scattering is the relevant physical effect [41]. The average diameter of water droplets in clouds is between 10 and 20 µm [22]. This size is responsible for Mie- scattering of mainly IR

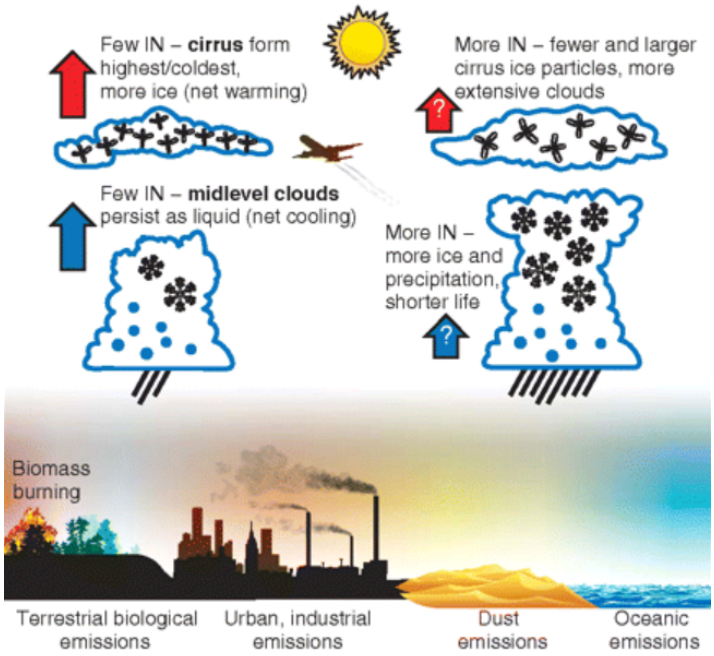

Figure 1.11.: The effects of IN in clouds on climate. Figure adapted from DeMott et al., 2010 [16].

radiation and geometric scattering of visible light by cloud droplets. Hence, the scattering efficiency of a cloud in the atmosphere is highly dependent on the size of its droplets, the number concentration and the phase state (i.e., the geometrical factor and refraction index). Thus, the cooling or heating effect of clouds in our atmosphere related to the Earth's surface depends on their microphysical state. In general, it was observed that the global cloud forcing tends to be a cooling effect [20]. However, there is a large uncertainty for ice and mixed-phase clouds and for the influence of IN on the albedo as described by Seinfeld et al., 2016 [17]. In their theory, a high number of efficient IN leads to higher nucleation rates. Hence, the resulting ice phase in clouds tends to have larger ice crystals with a lower number concentration. This effect is visualized in Figure 1.11, where midlevel mixed-phase clouds are predicted to have a cooling effect while cirrus clouds are reported to have a heating effect on the global energy budget. Beside the effect on the global albedo, IN also lead to more precipitation when present in mixed-phase clouds, since rain, snow or other forms of precipitation are based on the predominate existence of ice in clouds [16, 17]. Thus, the number concentration of IN is rather important in understanding the envelopment of mixed-phase clouds. In detail, the time and location of the cloud when it forms precipitation is valuable for weather forecast. The global influence on the hydrological cycle is from further importance when it comes to dry periods forced by global warming.

1.3. Biogenic Aerosols

1.3.1. The Biosphere

The biosphere of our planet describes the part of Earth's crust, water and atmosphere that supports life [42]. Reaching from deep sea levels and parts of the lithosphere [43] up to high altitudes in the atmosphere [44], biological organisms have populated nearly every space where environmental conditions are suitable. The Five Kingdoms of life reach from prokaryotic microorganisms (bacteria and archaea) to uni- and poly-cellular eukaryotes (e.g., fungi, plants, animals) [45]. Prokaryotic microbes lack of a nucleus membrane in their cellular structure, compared to eukaryotic cells. A simple cellular structure enables bacteria and archaea to cultivate very harsh environments. An extreme example is given in the Yellowstone National Park, where a high biodiversity can be found in the Hot Springs (i.e., thermal lakes with temperatures up to 95°C and high concentrations of solutes, shown in Figure 1.12) [45]. Organisms dealing with extreme conditions can also be observed in the cryosphere (i.e., the part of the Earth's surface characterized by the presence of frozen water). By analyzing ice samples, a large amount of living bacterial cells (10^3 to 10^5 cells per mL) can be found in Arctic sea ice [46], in ice on the South Pole [47] and even in glaciers on the Mount Everest in the Himalaya [48].

Figure 1.12.: Microorganisms have populated every possible niche on Earth including the Hot Spings in the Yellowstone National Park. Photograph taken by Hinrich Grothe.

Even though heat and frost stable microbes populated the hottest and coldest habitats, most forms of life prefer milder conditions. Especially near the land surface or the ocean surface, biotic (i.e., living) and abiotic (i.e., nonliving) factors are beneficial for many organisms. Atmospheric gases filter deadly UV-radiation from SR, enabling photosynthetic active organisms to spread. Algae and cyanobacteria float below the sea surface, while plants, liches and others prefer a solid ground on the land surface and form the terrestrial vegetation. Furthermore, heterotroph organisms (fungi, animals and many bacteria) feed on autotrophic ones and thus, the number of cells is enriched near surfaces. Floating cells

that adsorb on a surface tend to multiply when nutrients are available. Thereafter, so called bio-films grow on nearly every mers and sub-mers surface [49]. Multi-cellular organisms colonize very beneficial niches and even increase the available surface. Thus, more bio-films can be developed and the space for life expands (e.g., on the surface of leaves (phylosphere) or roots (rizosphere) of trees). An enriched environment of biological cells is likely to interact with atmospheric processes by emitting biogenic aerosols. Many biogenic aerosols are formed near the land surface. Possible mechanisms on biogenic aerosol generation are wind induced aerosolization, rain induced splashing mechanisms, or the formation of secondary aerosols from the gaseous compounds emitted from vegetation [50–52]. Figure 1.13 shows the average simulated concentration of bacteria, fungal spores and pollen around the globe. It can be observed, that about 10^5 bacteria, 10^4 fungal spores and 10^2 pollen are dominantly present in one m^3 of atmospheric air, whereat the land surface contributes the most to the emission of those aerosols [53]. Thus, the biosphere expands not only to deep oceans, frozen pole caps and hottest springs, but also from the PBL to the free troposphere. A detailed view on different types of biogenic aerosols is given in Section 1.3.2.

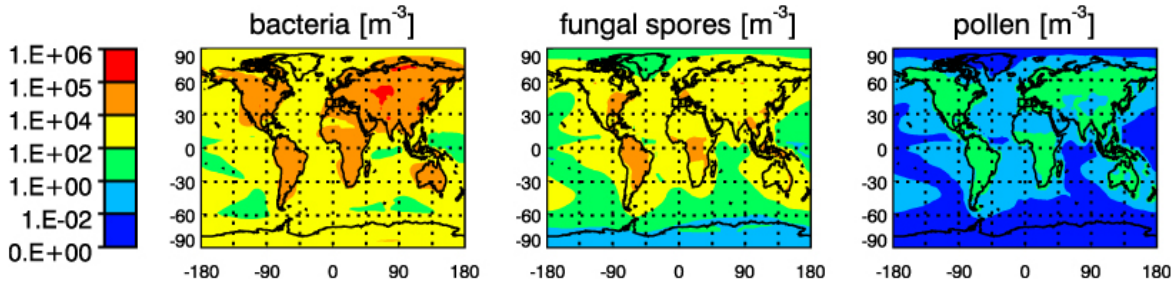

Figure 1.13.: Simulation of global bioaerosol concentration near land or sea surface. Figure adapted from [53].

As Charles Darwin stated in the 19th century, evolution is based on the survival of the fittest variations of organisms [54], and such contribute to the life within our biosphere today. Seasonal temperature variance is one of several stress factors that organisms have adapted to. When temperature drops below 0°C, water within biological cells tend to freeze. Uncontrolled cellular freezing events (i.e., freezing of cytoplasm) harm organisms and lead to deadly injuries, since their cellular structures get destroyed by ice crystals. Many multi-cellular organisms that deal with frost (e.g., insects and polar fishes) have enveloped freezing prevention by accumulating soluble polyols, lowering the freezing point by the colligative effect, and by anti-freezing proteins, that control the growth of ice crystals [55]. Controversially, plants have IN within their extracellular space to trigger heterogeneous freezing events intentionally [56]. That allows a controlled freezing of an intact tissue without freezing injuries, by increasing the nucleation rate (heterogeneous freezing) and further reducing the growth rate of the crystals. Consequentially, many plants in regions with harsh winter seasons include IN within their cells [57, 58]. Another evolutionary benefit is drawn for pathogenic bacteria and fungi that induce heterogeneous ice nucleation on the surface of

their substrate with particular IN. Thereafter, growing ice crystals harm cell-walls of plants and provide nutrition access to the pathogens [10, 59, 60]. To sum up, the biosphere expands over the whole planet and includes many organisms that biosynthesize IN for survival benefits.

1.3.2. Primary and Secondary Biogenic Aerosols in Heterogeneous Ice Nucleation

By definition an aerosol is a suspension of fine solid or liquid particles in gas [61]. Aerosols can be categorized in several size modes according to the mean diameter of the suspended particles (aerosol particles). The size of aerosol particles is an important parameter in several physical descriptions of that aerosol [61]. Thus, understanding the properties of several aerosols requires to perceptive the physical behavior of particles within a certain size range. For physical description, aerosol particles are often assumed as spheres, with a density of 1 g cm^{-3}. The corresponding diameter is referred to as aerodynamic diameter (d_p) [62]. Figure 1.14, shows a scale bar for common aerosol particles, found in the troposphere that include biotic (pollen grains, fungal spores, bacteria, viruses, proteins), organic (secondary organic aerosol) and inorganic matter (soot, sea salt aerosol, mineral dust). The size range, from gas molecules to large coarse-mode particles, expands over 7 orders of magnitudes. Thereby, aerosol particles in the size range between 0.001 to 1 µm are generally called fine and ultrafine aerosols while particles larger 1 µm are referred to **coarse-mode** aerosols. Further, the fine-fraction can be subdivided into **nucleation-mode**, **Aitken-mode** and **accumulation-mode** particles according to their diameter as shown in Figure 1.14 [63]. Another distinction can be made between particles that are emitted directly into the troposphere (e.g., pollen grains, fungal spores and sea salt) or particles that are formed within the troposphere out of gas molecules (secondary particles). The formation of nucleation mode particles is described as nucleation from clusters of molecules (e.g., water, sulfuric acid, ammonia and organic compounds). Therefore, the classical nucleation theory (see Section 1.2.2) can be taken into account. A typical growth rate for nucleation mode particles is around 1-20 nm h^{-1} [64]. The formation of nucleation mode aerosol is beneficial in areas where the surface area of pre-existing particles is low. With high preexistence of aerosol surfaces the formation of Aitken-mode and accumulation-mode aerosol is preferable. Thus, the molecules are transported to the surface via diffusion and further accommodated to the surface of foreign aerosols. Moreover, liquid phase diffusion, solubility or chemical reaction processes (i.e., heterogeneous reactions) can lead to further growth of the particles [64]. The coarse-mode fraction of aerosols is mainly generated via mechanical processes. Thereby, wind-blown dust, biogenic emission or anthropocentric pollution are three of the main sources. Considering the time interval where an aerosol stays airborne in the troposphere, the deposition flux F, for dry deposition, can be described as

$$F = v_g c \tag{1.29}$$

where c is the concentration of the aerosol and v_g is the sinking velocity. This process is highly size dependent and only valid for accumulation-mode particles. The actual deposition mechanism for ultra fine particles (i.e., nucleation-mode and Aitken-mode) is due to Brownian diffusion, whereat for coarse-mode particles, impaction and gravitational sedimentation has a higher impact [64]. Furthermore, aerosol particles, especially accumulation-mode, are often removed via wet deposition from the troposphere during rainfall. However, the deposition rate is an efficient parameter to describe a quantitative connection between the sinking velocity and the concentration of airborne aerosols. Thus, F is from further interest for an evaluation of the impact that aerosols have on atmospheric processes.

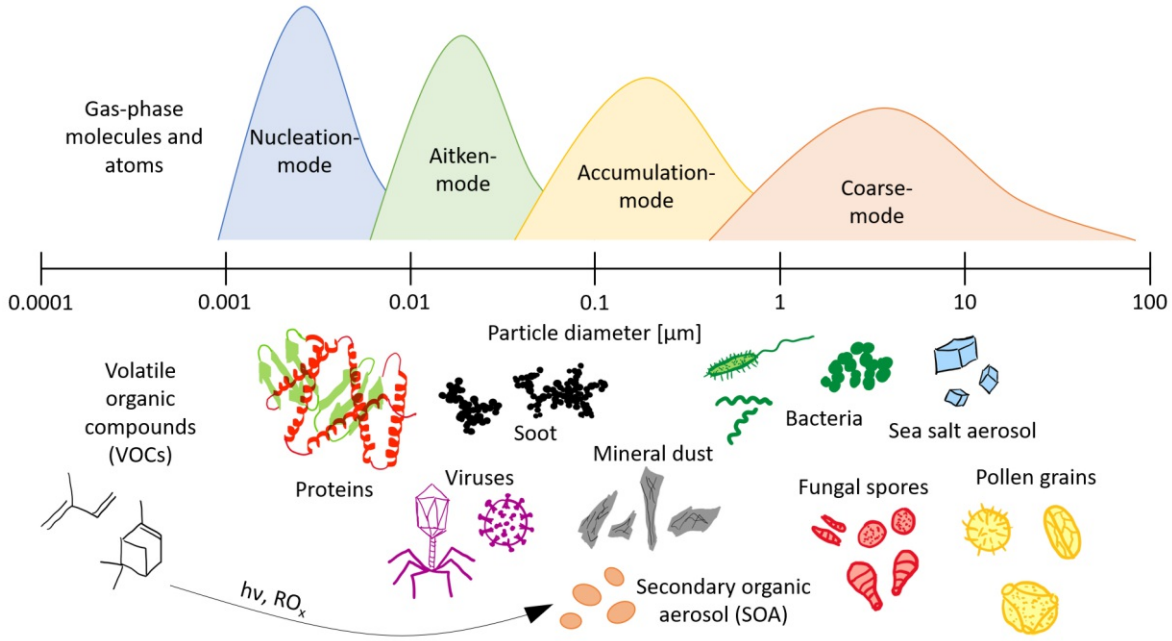

Figure 1.14.: Compostion of several aerosols and aerosol modi.

Aerosols from biological origin, referred to as bioaerosols [61], range from the size of proteins (~10 nm), towards viruses (~50 nm), bacteria (~1 µm) and fungal spores (~5 µm) to pollen (~30 µm) [50]. Bioaerosol can be generated in various ways, either natural (e.g., pollination, sporulation, rain induces aerosol generation, sea spray aerosol generation) or anthropogenic (e.g., harvesting). Most common bioaerosols are discussed in detail below.

Pollen Grains and Sub-Pollen-Particles

Pollen grains are the male gametophytes of plants and thus, a part of the sexual reproduction mechanisms. Pollen can either be transported in the air as bioaerosols via wind motion or via shutteling on insect or bird bodies. Airborne pollen contribute to the large size fraction of coarse-mode aerosols, having diameters between 20 and 100 µm [51]. Detailed microscopic

pictures of pollen from *Betula pendula* are given in Figure 1.15, A and B, while a schematic comic of the structure is given C. Pollen grains exhibit pores that are used for germination after deposition on the female gametophyte. Furthermore, the capsule, consisting of different layers (coat, exine, intine), encloses the cytoplasm which includes starch granules, the vegetative and generative nucleus [65].

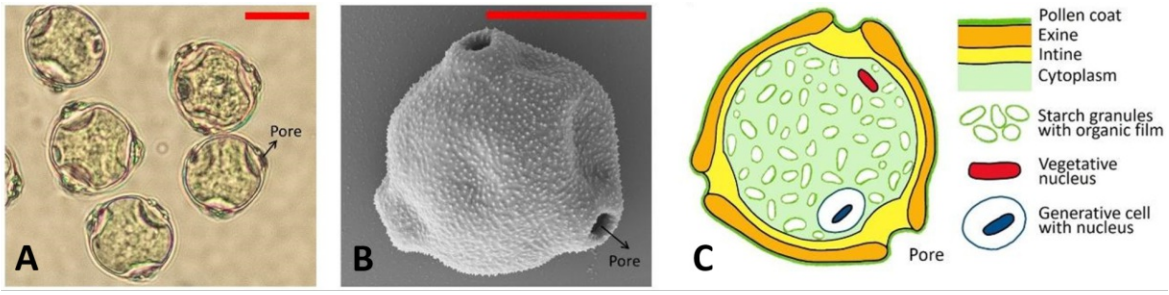

Figure 1.15.: Illustration of pollen grains and their inclusions: A) Light microscopic and B) SEM image of pollen grains. Pores are marked with an arrow, red scale bar is 10 µm. C) Schematic comic of a pollen grain cross section. Figure adapted from Burkart et al., 2021 [65].

Pollen of silver birch (*Betula pendula*), scots pine (*Pinus sylvestris*), common juniper (*Juniperus communis*) and many other species are known to nucleate ice at around a mean freezing temperature (MFT) of -20°C [66, 67]. Even though the annual emission is ~50 Tg year^{-1}, the deposition velocity of such large coarse-mode fraction is high (due to gravitational sedimentation) and the availability is limited temporally to pollination periods. Therefore, the concentration in the atmosphere remains quite small (~10^2 m^{-3}) compared to fungal spores and bacteria (see Figure 1.13) [53]. However, pollen grains tend to rupture when relative humidity expands over a certain threshold (i.e., pollen bursting) [68] or mechanical forces destroy the pollen grains wall [65]. During pollen bursting, water molecules that are adsorbed on the surface, tend to diffuse through the pollen capsule attracted by the lower chemical potential of the solution inside the grain. Thereafter, the pressure in the capsule rises (osmotic pressure), till a limit is exceeded and the grain release cytoplasm through its pores. Thus, biogenic material that includes starch granules, referred to as sub-pollen-particles (SPP), and macromolecular matter is released to the environment. The size of SPP is < 1 µm and it is assumed, that SPP nucleate ice at temperatures typical for pollen [69]. Pummer et al., showed that the macromolecular ingredients of birch pollen are IN in the nanometer size range [39, 67]. Furthermore, Burkart et al., 2021 suggest that SSP are possible shuttles of macromolecular IN to be transported into the free troposphere [65]. Thus, the sinking velocity of those IN would be orders of magnitude lower as for pollen grains and the atmospheric relevance would increase tremendously. Very recently, it has been shown that the release of IN from birches is not limited to the pollination period [57]. Seifried et al., 2020 presented the availability of extractable macromolecular IN on the surface of *Betula pendula* [70]. It has been shown, that rain droplets wash off IN from leaves,

wood and bark of birches very efficiently. Thus, aerosolization during impaction of rain droplets on vegetation can be taken into consideration. Eventually this is another important source from plants regarding IN emission beside pollination.

Fungal Spores

Fungi are eukaryotes organisms, with a high variance of different mono- or multi-cellular species. Multi-cellular fungi produce filamentous hypha and reproduce sexual or asexual by the emission of spores. Those can be characterized into three types of sexual spores, while ascospores are released from an ascus (i.e., longitudinal tube), basidospores from an basidium (i.e., pedestal on fruiting body) or teliospores from a telia (produced by rust fungi) [51]. In an asexual stage, fungi can spread conidiospores (produced in a hyphal section called conidiophores) [51]. The size of fungal spores varies most frequently between 2 to 10 µm [71], while the shape is often ornamented, spherical, elongated or cylindrical [72]. Calhim et al., 2018 suggest that the shape of spores is evolutionary driven to a preferred substrate for a given fungi species (e.g., ornamented spores tend to reach lower soil layers as roundish shaped). Therefore, the diversity of shape and size from fungal spores is almost as high as the diversity of fungi themselves. Many fungi are known to contain IN with high freezing temperatures (MFT ~ -6°C), some of which are in the macromolecular size range [60]. To name a few species, *Fusarium acuminatum*, a plant pathogen [60, 73], *Mortierella alpina*, a widespread soil fungi [74] and *Endocronartium harknessii*, a rust fungi found in pines [75], are discussed as possible contributors to atmospheric cloud glaciation in literature. Fungal spores are rated as major contributors to the bioaerosols' mass, with an annual emission of ~50 Tg $year^{-1}$, an average number concentration of 10^3 to 10^4 m^{-3} in atmospheric air and emission-fluxes of 200 $m^{-2}s^{-1}$ on land surface [51].

Bacteria

Bacteria are among the most intense studied bioaerosols in atmospheric ice nucleation due to the early discovery of *Pseudomonas syringae*, a plant pathogen that nucleates ice at -2°C [9–11]. Additionally, many other bacteria, to name a few *Pseudomonas fluorescens*, a fluorescent bacterium found in soil and water, *Erwinia ananas*, a plant pathogen growing on several fruits, and *Xanthomonas campestris*, another plant pathogen found on cruciferous vegetables, have been isolated as efficient IN [76]. The abundance and biodiversity of bacteria producing efficient IN within the decomposing ecosystem is tremendous. A simple leaf litter sample which was previously analyzed in the 1970's by Schnell and Vali [7] and Maki et al., [9] turned out to include 1170 bacterial colonies, many of which including macromolecular IN similar to macromolecular IN from pollen and fungi [77]. In the atmosphere bacteria are present in concentrations about 10^4 m^{-3} [78] and tend to have the largest global number concentration compared to fungal spores and pollen (see Figure 1.13). In the free troposphere, viable

bacteria can be found up to heights of about 70 km [79]. Due to their small aerodynamic diameters (~1 µm), bacteria have a low sinking velocity and thus travel long distances up to thousands of km [51]. Moreover, bacterial IN have been detected in several freshwater lakes [80, 81], melted snow-water [82], rain droplets [83] and in atmospheric cloud water [84], indicating their permanent occurrence in the hydrological cycle. With an annual emission of around 1 Tg $year^{-1}$ (below pollen and fungal spores), but the highest number concentration, emission-fluxes of around 250 m^{-2} s^{-1} and highest heterogeneous freezing temperatures, bacteria are rated as the major source of biological IN in cloud glaciation [51, 53, 85].

Viruses

A biological virus is a submicroscopic infectious agent (multiplying in host cells only), that contains genetic information (RNA or DNA) which is surrounded by a protein coat. The forms of the capsule can vary in size (20-300 nm) and shape (spherical, icosahedral, helical, etc.). In general, viruses are known to cause diseases in animals and can spread globally, such as during the Spanish flue or COVID-19 pandemic. On a global scale, viruses are the most abundant microbes in ocean water assuming a total number around 10^{30}, with an average concentration of 3 10^{9} L^{-1}, and the second highest contributor to biomass in the world (next to prokaryotes) [86]. Even though, viruses can be found in aerosols above the Earth's surface [87, 88], their contribution to heterogeneous ice nucleation in the atmosphere might be low, since investigated viruses nucleate ice around homogeneous freezing temperatures [89]. However, calculated deposition rates are around 10^{9} m^{-2} per day [90] and thus, indicate high concentrations of viruses in the atmosphere. Thereafter, not many results are present at the time in literature and the effect of viruses and biogenic macromolecules that stick to aerosol particles in form of dust, soil or others could be underestimated.

Biological Nano-IN on the Surface of Aerosol Particles

It can be assumed that around 69% of viruses and 97% of bacteria are attached to dust or organic aggregates within atmospheric aerosols [90]. Dust, being covered with biological matter tends to nucleate ice up to four orders of magnitude more efficiently than "sterile" dust [91]. Therefore, the freezing temperature of soil aerosol might be underestimated in atmospheric models due to biological coating. Bacteria, pollen and fungal spores contain IN mostly in the macromolecular size range around several hundreds of kDa [39, 60, 77]. Further, these IN are easily extractable during rainfall [70] and can be float into the soil territory. O'Sullivan et al., 2015 suggested that there is a reservoir of nano-IN within the soil of the biosphere [92]. They hypothesize that nano-IN, attached to agricultural soil, can get aerozolized (e.g., during agricultural land-use) and expand the concentrations of pollen, fungal spores, bacteria and other biogenic IN by orders of magnitude. These IN are not included in atmospheric models such as described by Hoose et al., 2010 [53] or DeMott et al., 2010 [16]. However, the basic knowledge of those nano-IN is still rather limited and more

research is needed to calculate the abundance and impact on cloud glaciation.

Secondary Organic Aerosols

Secondary organic aerosol (SOA) is organic matter that forms from volatile organic compounds (VOC) within a gas phase reaction [93, 94]. In more detail, such gas-particles conversions include nucleation (see Section 1.2.2), condensation, heterogeneous and multiphase chemical reactions [95, 96]. Consequently, biogenic gases can produce biogenic SOA [50]. Biogenic VOC (e.g., ethylene, methyl salicylate, methyl jasmonate or isoprene) are known to be released by plants induced by biotic or abiotic stress factors [94, 97]. Since VOC emission is based on complex biological mechanisms [97], the study of SOA as general aerosol particles is rather complicated. However, it can be stated that isoprene, one major contributor of VOC from plants, points out with an annual emission of 500 Tg year^{-1} [94]. Thus, only a percentage of isoprene beeing converted into SOA would yield organic mass comparable to fungal spores, pollen or bacteria as aerosol. Andreae and Crutzen, 1997, estimated the emission of SOA around 30 to 370 Tg year^{-1} [98], while Hallquist et al., 2009 assumed the biogenic amount to be 12 to 70 Tg year^{-1} [95]. The size of SOA, when fully enveloped is well below 1 µm and around 200 nm [93, 99] contributing to the accumulation-mode fraction of aerosol particles. SOA tends to be ice nucleation active at low temperatures ($<$ -25°C, [100]) or even completely near homogeneous temperatures (-38°C) [101]. Compared to biological IN, with well defined high freezing temperatures, the role of SOA as atmospheric IN is very unclear due to the high variance of possible VOC as precursors [95].

2. Motivation of the Thesis

Very recently, over 11 000 scientists from around the globe highlighted the urgent threat of global warming for life on Earth [102]. The temperature on the land surface was 1.53°C higher from 2006 to 2015 than from 1850 to 1900 [103], leading to drastic changes in many ecosystems. Figure 2.1 shows the measured and modeled global temperatures over the last 60 years reported by the Intergovernmental Panel on Climate Change (IPCC) [104].

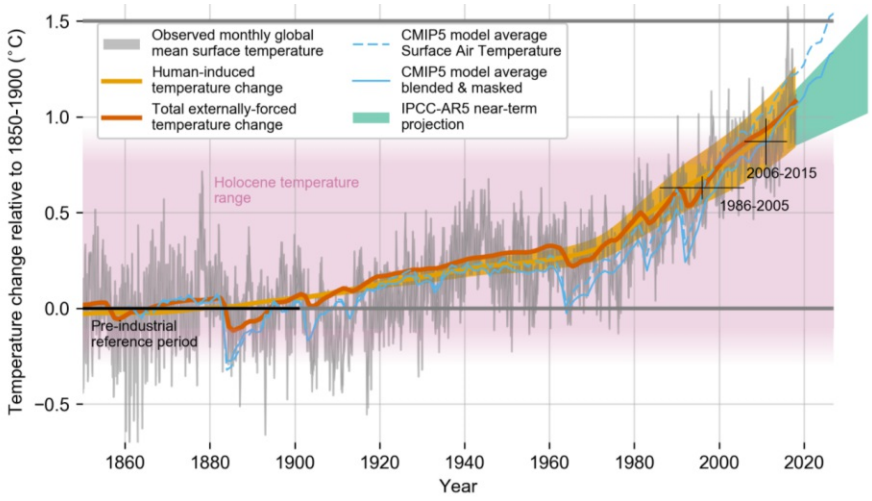

Figure 2.1.: Measurements and model predictions of global warming, reported by the Intergovernmental Panel on Climate Change (IPCC). Figure adapted from [104].

Today around 12% to 14% of the global ice free land surface is covered with croplands for agricultural usage, while artificial fertilization influences nearly every ecosystem on Earth [103]. The land-use caused a shrinking of global biodiversity of about 11% to 14% [103]. Models predict that climate change will decrease important community types, such as alpine habitats, subalpine spruce-fir forest or the maple-beech-birch forest [105]. In the European Alps, the effect of climate change is even more pronounced than in the northern hemispheric land surface [106]. A change of the (regional) land surface vegetation leads to different emissions of bioaerosols from plants, fungi and bacteria. According to the IPCC, the physical understanding of aerosol-cloud interactions is rather limited. Heterogeneous ice nucleation induced by aerosols leads to changes in albedo and life-time of ice and mixed-phase clouds as explained more precise in Chapter 1. Clouds and aerosols contribute to the largest uncertainties of estimating and interpreting the Earth's energy budget [107]. Furthermore, about 45% of the variance of aerosol forcing on climate change models originates from

natural emission sources [108]. This has motivated this empirical study on the emission of bioaerosols. Measurements above vegetation should lead to a better understanding of seasonal and spatial variations in bioaerosol generation. A physico-chemical characterization of sampled bioaerosol reveals the effects on atmospheric processes. The overall goal of this research is to contribute to a better understanding of bioaerosol emissions from alpine regions, regional climate and the feedback mechanisms between the biosphere and the atmosphere.

2.1. State of the Art

Most measurement techniques for atmospheric aerosols depend on ground-based or aircraft-based sampling devices (e.g., [109–112]). Thus, the sampling procedure is either stationary, fixed with a defined altitude and location, or limited by a minimum operational height for airplanes. Since the vertical profile of an aerosol species can be rather complex, the information between ground and aircraft heights gets lost using conventional sampling methods as illustrated in Figure 2.2. This information is from significant importance when calculating model parameters such as emission-fluxes of bioaerosols.

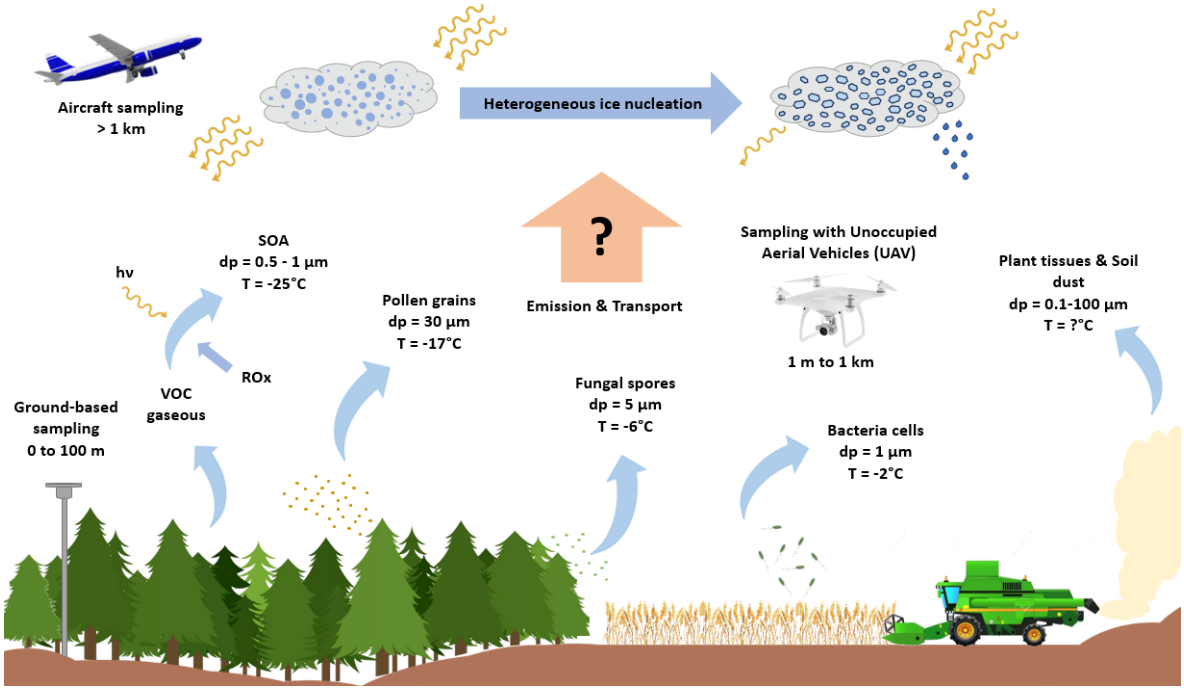

Figure 2.2.: Schematic comic of bioaerosol generation, its influence on ice nucleation (aerodynamic diameter (d_p) and average freezing temperature (T) is given) and measurements of bioaerosols using aircrafts, ground-based sampling devices and unoccupied aerial vehicles (UAVs) are illustrated.

New technologies using unoccupied aerial vehicles (UAVs) enable the sampling of bioaerosols in heights between 1 m and several hundred meters above ground level [113–119]. For instance, Crazzolara et al., 2019 reported the usage of a rotary-wing drone to sample bioaerosol (e.g., pollen) in the PBL [119], while Schmale et al, 2008, focused on aerobiological sampling of culivable microbes with fixed-wing drones above corn fields [115]. These studies highlight the strength of UAVs to be used for investigations on specific biogenic emissions of aerosols.

2.2. Goal of the Thesis

On particular interest for biogenic emission of IN is frost resistant vegetation. We focused on the analyzation of birch, pine and other cold resistant plants and their ability to release IN to the atmosphere (e.g., during pollination periods) in previous studies [39, 57, 58, 67, 70]. Very recently, Seifried et al., 2020 reported the release of nano-IN (< 0.2 µm) from birches during rainfall events [70]. To estimate the impact of such nano-IN on cloud glaciation we focused a field campaign on a remote spot in the Austrian Alps. **The goal of this thesis was the development of a sampling device for airborne biogenic IN above emission sources, that can be attached to commercial UAVs.** The device should be of minimum weight (capable for small scale UAVs), sample airborne IN with accurate efficiency and further measure meteorological parameters during the flight time interval. The aerosol should get analyzed using freezing assays and microscopic techniques (fluorescence microscopy and scanning electron microscopy). Findings should answere the questions if airborne biogenic IN can be found in high concentration (above the average continental background concentration) in the vicinity of frost resistant vegetation (e.g., after rainfall events or during pollination periods).

3. Methodology

In general, this chapter includes the description of the self-built sampling device, information of the field campaign and all analytical aspects of the investigations performed during this thesis. For some methods, a theoretical knowledge gives the advantage to understand the procedure properly. Therefore, a short theoretical note is given when necessary. However, for a detailed basic description the interested reader is refereed to appropriate literature provided in books and papers. Figure 3.1 gives an overview on the flowchart of the methodology. In short, a bioaerosol gets sampled with the drone-based aerosol sampling impinger/impactor (DAPSI) setup, that can be suited on remote controlled UAVs. Impactor foils get analyzed with microscopic techniques, while impinger samples are used for freezing experiments. In addition to the sampling procedure, online measurements of environmental parameters are performed using optical and electrical sensors driven by an onboard computer.

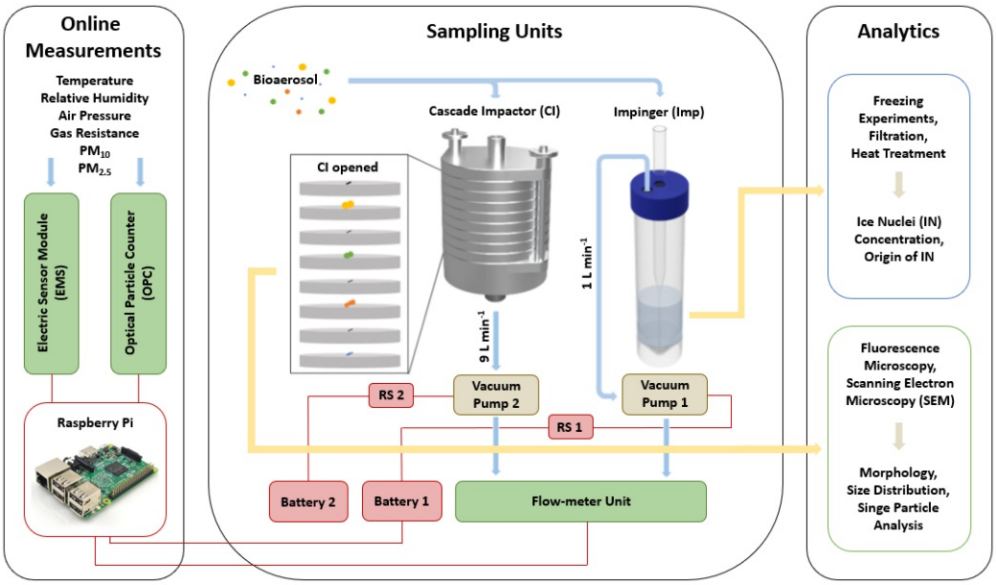

Figure 3.1.: Schematic drawing of the sampling principle, partly adapted from Bieber et al., 2020 [120]. Bioaerosol is sampled in a cascade impactor (CI) and an impinger (Imp). Both sampling systems are connected to vacuum pumps that get adjusted by a flow-meter, and switched on and off by remote switches (RS 1 and RS 2). Analytical analyses are carried out by microscopy and freezing assays. Online measurements are performed with an optical particle counter (OPC) and an electric sensor module (ESM) controlled via a Raspberry Pi onboard computer.

3.1. Tool Building

The self-built system DAPSI consist of two sampling units, namely an impinger (Imp), that samples aerosols in aqueous solution and a cascade impactor (CI) that samples aerosols on impaction stages. Each sampling setup can be attached to small scale UAVs, such as DJI Phantom 4 rotary wing drones (see Figure 3.2). These sampling devices (visualized in Figure 3.1) soak in an aerosol at the spot of interest, in our case a bioaerosl in the vicinity of alpine vegetation. Thereafter, the sampled bioaerosol can get analyzed by microscopic techniques and freezing assays (see Section 3.4). A detailed description of the Imp and CI is given in Section 3.1.1. To gain information on the meteorological data of the sampling period in high resolution (temporal and spatial), one drone was equipped with sensors (optical particle counter and electric sensor module) and an onboard computer (Raspberry Pi). The hard- and software of the measurement devices are described in Section 3.1.2 and 3.1.3.

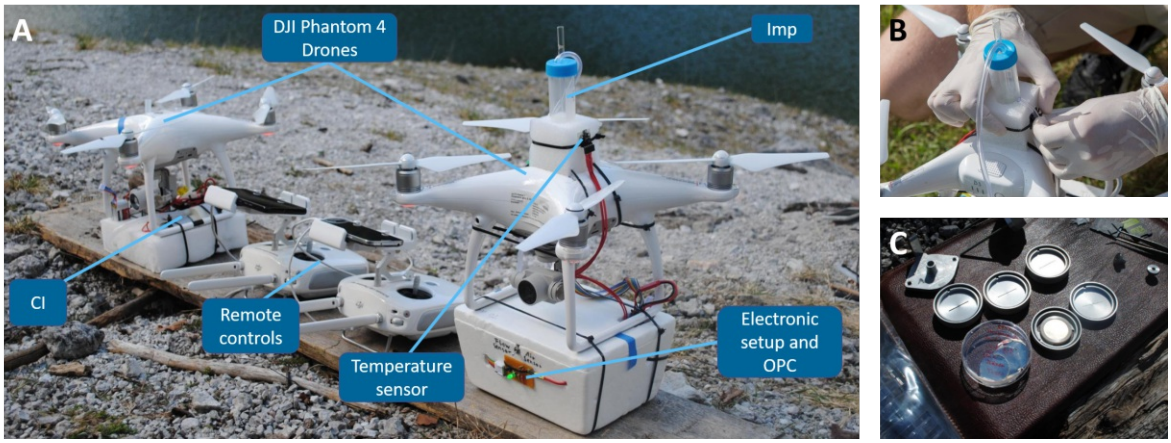

Figure 3.2.: A) Photograph of the sampling units attached to DJI Phantom 4 drones. On the left side one drone is shown which carries the cascade impactor (CI) setup and on the right a drone which carries the impinger (Imp) system. B) Imp system on top of the drone. C) CI opended during the exchange of the foils.

3.1.1. Sampling Devices

Cascade Impactor

For the size resolved sampling procedure, a light-weight CI is used (personal impactor, SKC Ltd., Great Britain). This impactor (visualized in Figure 3.1) samples aerosol particles on four stages (A,B,C and D) with well defined cutoff diameters (2.5 µm, 1.0 µm, 0.50 µm and 0.25 µm). To load the stages prior to every measurement, pre-baked aluminum foils are used (>3h, 460°C). This enables a direct investigation via fluorescence microscopy and a further procedure to electron microscopy as described later. The needed air flow (9 L min^{-1}) is produced by an electric pump which is adjusted with a potentiometer and a self-built flow-meter (see Section 3.1.2). The inlet of the vacuum pump is connected to the outlet

of the CI, while the inlet of the impactor is connected to the top of the UAVs casing via polyvinyl chloride (PVC) tubes. The sampled particles on the aluminum foils and the blank control sample are kept at room temperature in sterile petri dishes. The petri dishes are sealed with Parafilm© to avoid gas exchange and contamination prior to analysis. The sampling principle of an CI is described in the following *Theoretical note*. A picture of the opened CI during the field campaign is shown in Figure 3.2, C.

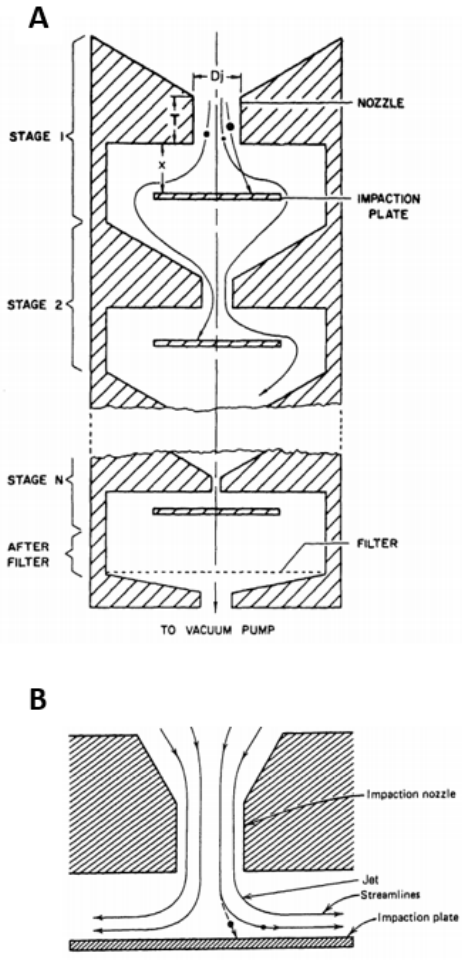

Figure 3.3.: Sampling principle of an cascade impactor: A) a drawing of a cascade impactor with N stages, B) airstream of a well defined stage with particles imapcting. Figure adapted from Hinds, 1999 [121].

Theoretical note:

An aerosol particle has a curviliniar motion when following a curved path [121]. This motion can be characterized by a dimensionless number, the Stokes Number, Stk, as stated by

$$Stk = \frac{\tau U_0}{d_c}, \text{ for } Re_0 < 1 \tag{3.1}$$

where U_0 is the undisturbed velocity, τ the time a particle needs to adjust to a change of accelerating forces and d_c the distance that is available for the adjustment. This equation is valid for laminar flows, i.e., when the Reynolds number is smaller 1 ($Re_0 < 1$). There are two possible extreme outcomes when a particle is forced into another direction within a gas stream: 1., for $Stk >> 1$, the particle continues to move in a straight line when the gas turns its flow direction and 2., for $Stk << 1$, the particle follows the stream line perfectly [121]. In case of an impactor with a rectangular nozzle, d_c can be rewritten as the half-width of the jet's stream divided by two. Furthermore, τ can be replaced by the properties of a given particle (i.e., a function of the aerodynamic diameter, the density and others) and therefore, the Stokes number is a function of the geometry of the impactor and the characteristics of the aerosol particle. By designing a geometric defined nozzle and a corresponding impaction plate (Figure 3.3, B), the collection of aerosol particles with defined aerodynamic diameters is achieved. In practice, the cutoff diameter of an impaction system is given, which defines the particle diameters at which around half of the particles impact and the other half follows the stream. This assumption however, includes that every particle tends to be of spherical shape and has a density of 1 g cm^{-3}. For an improved sampling procedure, CI are developed where several cutoff stages are given to collect particle fractions with defined diameters (Figure 3.3, A).

Impinger

To sample IN in aqueus solution, a self-built Imp is used seated on top of the UAV (see Figure 3.2 A and B). In general an Imp follows the same physical laws as described above for an CI, but with the difference that the "impaction stage" is liquid [122]. This enables a better matrix for freezing assays (no further need of sample preparation) and is also from interest when microbes should get colonized afterwards. The self-built Imp consists of a sterile vial (centrifuge tubes, screw c., 50 mL, Brand, Germany) that is modified by drilling a hole in the cap to fit a glass pipette (Pasteur pipettes without cotton stopper, Roth Germany) and a second hole to get connected with a PVC tube to the vacuum pump (see Section 3.1.2). After filling the Imp vial with 15 mL of ultrapure water (produced by Millipore(R)SAS SIMSV001, Merck Millipore, USA), the pipette tip immerses 30 mm into the water. The nozzle of the tip has an inner diameter of around 1 mm, which gives a cutoff diameter for particles around 1 µm and a high sampling efficiency according to literature [122]. The actual sampling efficiency was determined empirically as described in Section 3.2. Prior to every sampling period, the vial and pipette of the Imp are changed to a sterile one and 15 mL of new water are filled in. For sampling aerosols, the air-flow is set to 1 L min^{-1} by controlling the pump via a potentiometer and measuring the flow via the flow-meter as described below. After launching the drones, the Imp setup is turned on via a remote switch (RS) to avoid contamination during the start or landing periods, since the propellers blow off dust particles when the UAV is near the ground.

3.1.2. Hardware

The complete hardware of DAPSI consists of four main parts, namely the controlling unit for the Imp (CUImp), the controlling unit for the CI (CUCI), the sensor unit (SU) (optical particle counter, electric sensor module and Raspberry Pi) and the flow-meter unit (FU). An overview of the connection is given in Figure 3.1, whereas a detailed circuit diagram is given in the Appendix A. In Figure 3.4 the CUImp and SU are depicted, whereat in Figure 3.5 the hardware of CUCI and FU are shown.

Impinger Control Unit

To create the necessary airflow (1 L min^{-1}) a vacuum pump (DC: 12 V, Delaman, China) is connected via a PVC tubing to the Imp. This pump is powered with an external battery (1000 mAh, 11.1 V, Wellpower, Lindinger, Austria). To adjust the power of the pump, the voltage is regulated via a 100 Ω potentiometer (4 W, AB Elektronik, Germany). Furthermore, the circuit includes a RS (Fernbedienung 1K Schaltfunktion, Wiltec, Germany), that can be turned on and off via a corresponding remote control. This enables the control of the Imp during sampling flights. All of the electric setup is placed into a

light polystyrene box to protect the equipment during the flight, and the box is mounted below the drone (see Figure 3.2, A) with cable wires. The opened box including the battery, remote switch, potentiometer and vacuum pump of the CUImp is depict in Figure 3.4, A.

Sensor Unit

The SU is included in the package of the CUImp as shown in Figure 3.4, A. The core of the SU is a Raspberry Pi onboard computer (Pi; Raspberry Pi 3 model B, Raspberry Pi Foundation, Great Britain), that is programmed to record and store data from the sensors and a note when the Imp is turned on. An optical particle counter (OPC; SDS011, Nova Fitness Co., China) is used to monitor the concentration of particulate matter, smaller 10 µm and 2.5 µm (PM_{10} and $PM_{2.5}$) during the sampling period (see Figure 3.4, B). The OPC is connected via an universal serial bus (USB) to the Pi. Furthermore, an electric sensor module (ESM; SEN-BME680, Joy-it, Germany) is mounted on top of the UAV next to the Imp (see Figure 3.4, C). The ESM is connected to the Pi via an inter-integrated circuit (I^2C) bus and measures relative humidity, temperature, pressure and the gas resistance. To control the SU during the field campaign (no desktop and keyboard present for the Pi), a self-built control-panel is installed on the outer side of the polystyrene boxing and connected to the Pi (see Figure 3.4, D). This includes a button to turn on and off the recording status of the measurements and a light-emitting diode (LED) that blinks when the system is in standby and gives a constant signal when the Pi is recording. Additionally, a switch is mounted on the outside to start the recording of values from the FU during the flow adjustments. A detailed description of the software is given in Section 3.1.3.

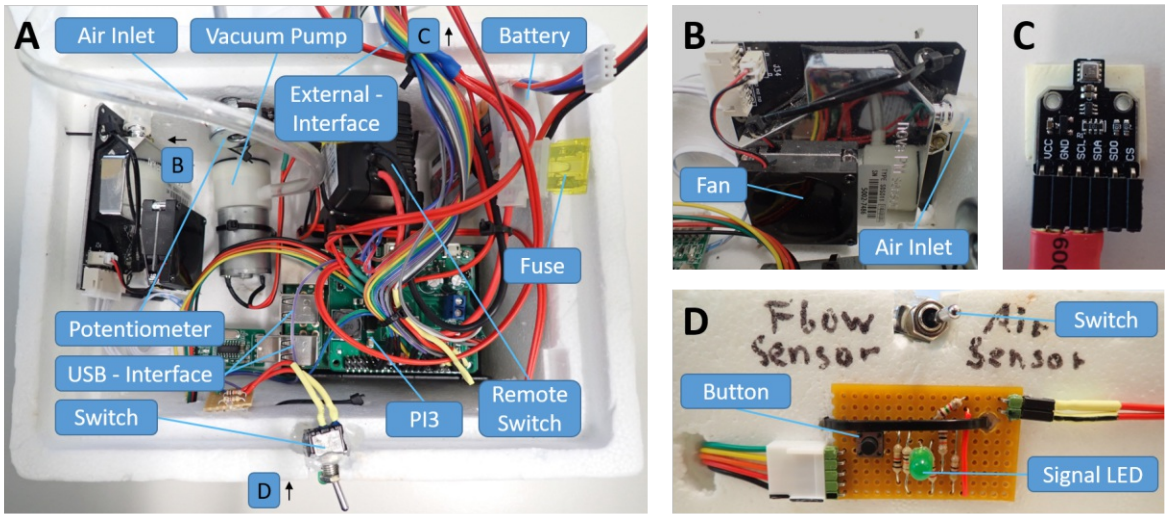

Figure 3.4.: Photographs of impinger control unit (CUImp) and sensor unit (SU): A) Overview, B)Optical particle counter (OPC), C) Electric sensor module (ESM) and D) Control panel.

Cascade Impactor Control Unit

The CUCI is quite similar to the CUImp, however, their is a slight difference in the used vacuum pump. Since the CI requires 9 L min^{-1} to sample the aerosol particles with size resolution, a more powerful pump is required (DC 12 V, Hilitand, China). The adjustment of the air-flow is carried out, as for the CUImp, with a 100 Ω potentiometer (4 W, AB Elektronik, Germany) and a lithium polymer battery functions as energy source (1000 mAh, 11.1 V, Wellpower, Lindinger, Austria). Also, a RS (Fernbedienung 1K Schaltfunktion, Wiltec, Germany) is included to turn the CI on and off while flying the drone. The setup plus the CI itself is embedded in a polystyrene bulk, that is properly to fit the equipment as shown in Figure 3.5, A.

Flow-meter Unit

To adjust the flow-rate for the Imp and CI a light-weight flow-meter unit (FMU) is built to be used in the field campaign prior to the sampling procedure. It is designed to be connected to the Pi during calibration and to be disconnected again before starting the flight (this was necessary to keep the weight of the airborne equipment as low as possible). The air-flow is assumed to be stable during the measurement and the influence of the changes in air pressure is assumed to be negligible when flying at low altitudes. The FMU consist of a flow sensor (AWM5102 VN, Honeywell, USA) that is placed inside a plastic box (see Figure 3.5, B and C). The analog signal is transferred into a digital one by using a 10-bit analog to digital converter (ADC; MCP3008-I/P, Microchip, USA) on an additional circuit board. An extra button is included on the board to send a signal to the Pi, when it should start to record values (as described in Section 3.1.3). The measured values are shown on a liquid crystal display (LCD; SBC-LCD 16 x 2 Display-Module, Joy-it, Germany). This enables the adjustment of the flow-rate during the field measurement. The flow-meter was validated by controlling the measured values in the laboratory with an analog flow-meter.

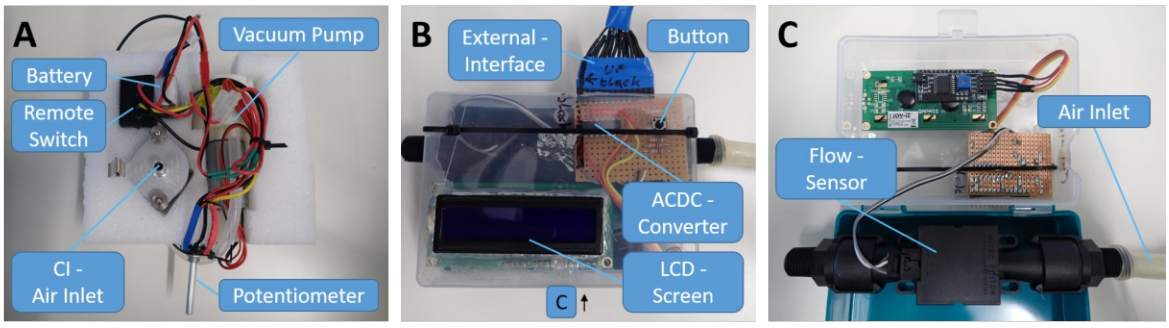

Figure 3.5.: A) Photographs of the hardware of the cascade impactor control unit (CICU) setup. B) Photograph of the flow-meter unit (FMU) and C) Inner life.

3.1.3. Software

The software for the raspberry Pi onboard computer is written in Python. Generally, it should fulfill three tasks: 1., control the FMU (i.e., the flow-sensor and the LCD) and save the measured values, 2., control the ESM and OPC and save the data, and 3., record the time of the Imp turned on and off via the RS. A flow-diagram is shown in Figure 3.6 and the full source code can be found in the supplementary material (Appendix B). The script is started automatically after the Raspberry Pi is turned on. This enables the operation of the device with the control panel (no desktop and keyboard needed). After stating the script, it asks if the toggle switch is turned to "Flow-measurement" or not. If that is the case, the script starts the air-flow measurement and prints values on the LCD. When the button for storage is pressed, the values are stored on the USB-stick. If the flow-switch is on "No", the script runs the sensor measurements for the ESM (temperature, pressure, relative humidity and gas resistance) and OPC (PM). Thereby, the signal of the Imp circuit is permanently asked and if the Imp gets turned on, the data are saved with "Imp ON". While this is not the case (i.e., during starting and landing periods) the information "Imp OFF" is added to the data of temperature, pressure, relative humidity, gas resistance, $PM_{2.5}$ and PM_{10} values. The resulting frequency of the environmental data is around 0.5 Hz.

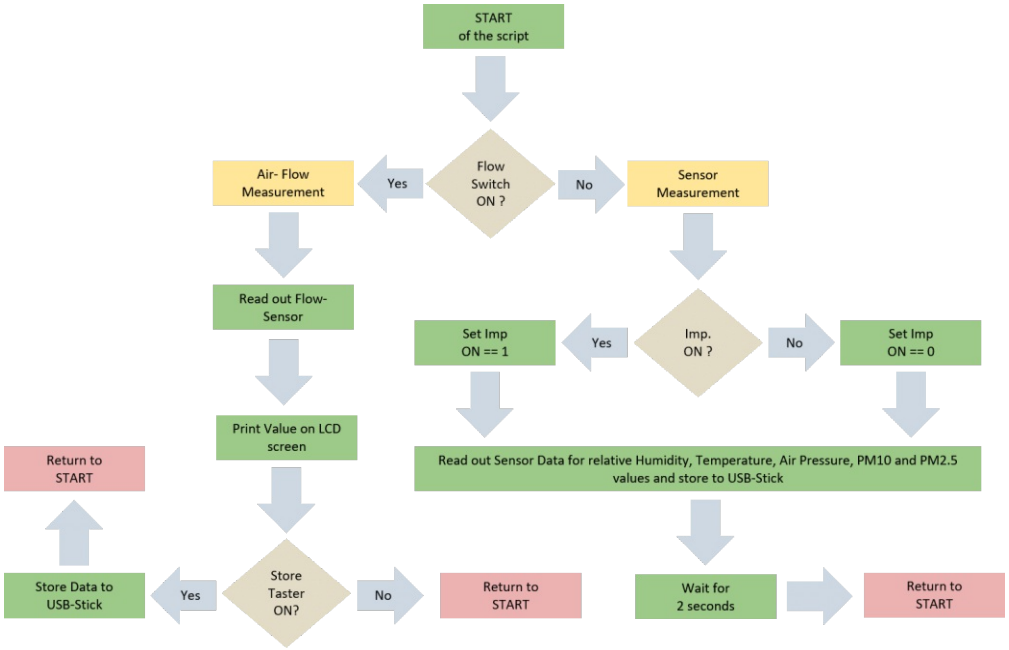

Figure 3.6.: Flowchart of the software script of the main program running on the Raspberry Pi 3 written in Python. Green: Command; Yellow: Start of Sub-Program; Brown: Query; Red: Return to start. Figure adapted from Bieber et al. 2020, [120].

3.2. Characterization of the Impinger

To gain information about the sampling efficiency of the Imp, two characterization experiments were performed. The first experiment focused on standardized polystyrene latex spheres, while the second experiment was carried out with biological IN extracted from *Betula pendula* pollen grains. Both efficiency test were published in Bieber et al., 2020 and thus, the following text passages (Section 3.2.1 and 3.2.2) are adapted from the paper [120].

3.2.1. Sampling of Standardized Aerosol Particles

In order to determine the sampling (i.e., removal) efficiency of the impinging system, polystyrene latex (PSL) spheres (Postnova Analytics, USA) were used as standardized aerosol particles. Similar tests have been described previously for other 3D-printed impinging systems [113]. Three droplets of PSL with 2 µm diameter were added to 100 mL ultrapure water, and an atomizer (Constant Output Atomizer Model 3076, TSI Incorporated, USA) was connected to the suspension and to purified compressed air. The created aerosol passed through a diffusion drying tube with 1.2 L min^{-1} and was then measured with an OPC (Model 1.109, Grimm Aerosol Techniques, Germany). After the particle concentration had stabilized for several minutes, the Imp was connected and the particle concentration after the Imp vial was measured again for another 10 min. Experiments were repeated with PSL spheres of 0.6 µm diameter. [120]

3.2.2. Sampling of Biological Ice Nuclei

To determine the sampling (i.e., removal) efficiency for biological IN from aerosols, we suspended 250 mg of birch pollen (*Betula pendula*, Thermo Fisher Scientific, USA) in 50 mL ultrapure water. After 6.5 h, the suspension was centrifuged, and the pollen grains were filtered off using syringes (5 mL Soft-Ject(R), Henke-Sass Wolf, Germany) and sterile filters (0.2 µm cellulose acetate filter, VWR International, USA). The obtained solution, birch pollen washing water (BPWW), containing IN [67], was atomized by using cleaned compressed air and an atomizer (same set-up as described Section 3.2.1). Aerosols were dried with a diffusion drying tube and then sampled with a flow-rate of 1 L min^{-1} with two Imp vials in a row. Ice nucleation activity was measured as described later in Section 3.4.1 and the efficiency was calculated by comparing the number of ice nucleation active particles sampled in each vial. [120]

3.3. Field Campaign

The field campaign took place in the year 2019 in Upper Austria (UA), Austria, Europe. It was split into two parts, whereat the first sampling days (referred to as UA1 and UA2) took place in the spring season (3rd and 4th of June 2019) and the second sampling period took place in summer (21th to 23th of August 2019). All measurements were carried out at the same location, next to a remote alpine lake (Hinterer Gosausee) situated near to the village Gosau. A satellite picture of the sampling site is shown in Figure 3.7, A, the investigated spot is encircled blue [a].

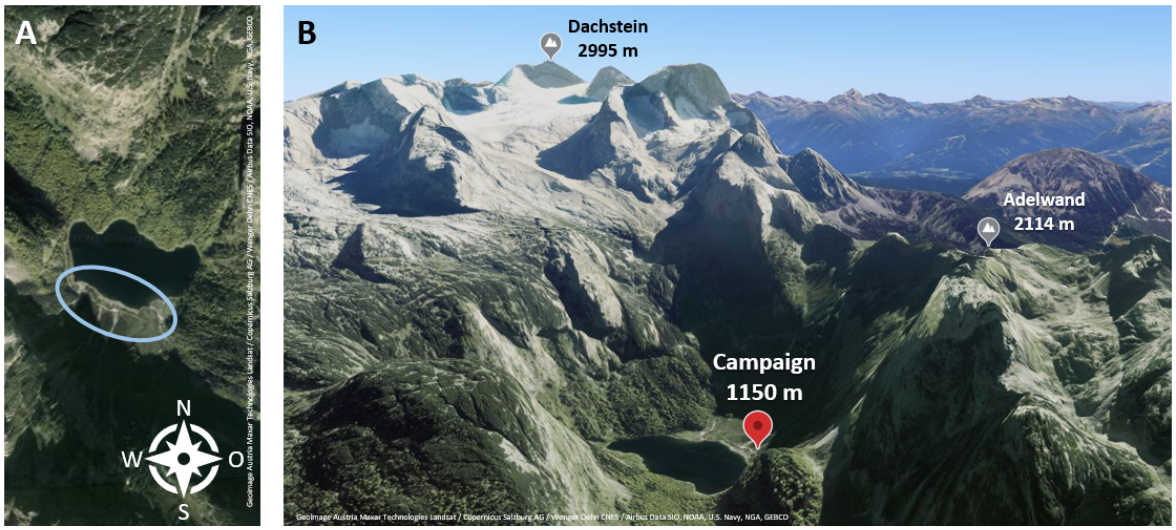

Figure 3.7.: Sampling location of the field campaign. A) Bird view of the sampling spot encircled in blue. B) 3D view of the sampling spot provided by Google Earth. Figures are partly adapted from Bieber et al., 2020 [120] and Seifried et al., 2021 [123].

The lake at an elevation of 1150 m is situated in an remote valley (as seen in Figure 3.7, B) surrounded with mountains (e.g., Dachstein, Adelwand) and thus the direct influence of anthropogenic emission sources is expected to be low. Furthermore, trees of the species *Pinus sylvestris*, *P. mugo*, *Betula pendula* and other cold resistant plants grow in high numbers around the lake. During UA1 and UA2, birches were still in their flowering period since the snow coverage of the alpine location lasts till early summer days and keeps the birches in a state of winter hardness. Thus, pollination was expected to contribute to the ice nucleation activity of the aerosol. For the second sampling period, rainy and wet days were chosen, since high relative humidity and the impact of rain droplets can increase the number concentration of bioaerosols and IN [124, 125]. Due to the rainfall on UA3, the drones were not flyable so samples were taken with the setup placed on ground. Furthermore, the wind on UA4 and UA5 was too strong for the drone carrying the CI to be controlled in a safe manner (the CI setup is at the upper limit of the weight which the drone can carry).

[a] GPS coordinates are 47.50°N, 13.55°E

Therefore, CI samples were collected ground-based whereas the Imp samples were collected from ground and airborne. The airflow of the sampling units were calibrated prior to the usage every day. In Table 3.1 all flight data are shown, including the flow calibration values, the sampled zone and the sampled air volume.

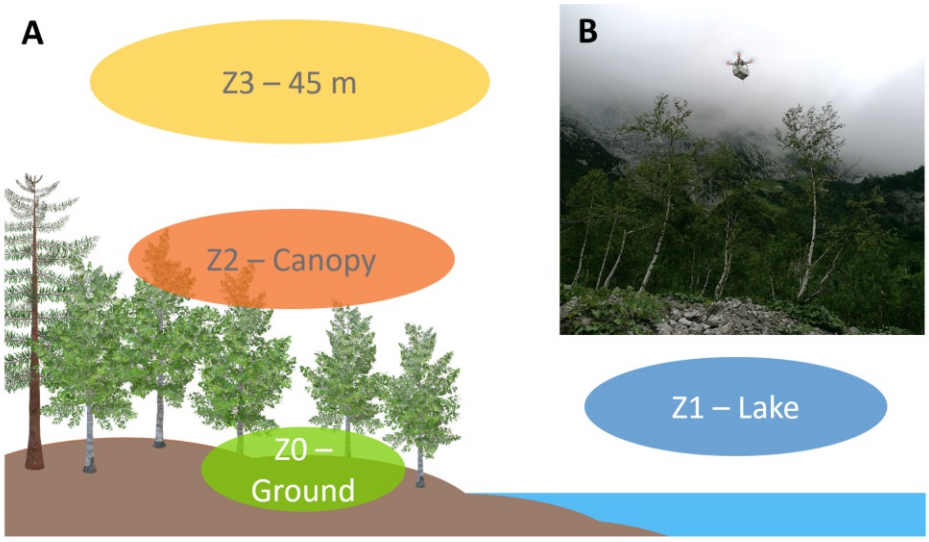

Figure 3.8.: Schematic drawing of the sampling strategy including the zones 0 to 3 (Z0 to Z3) illustrated in A), and picture of sampling procedure in Z2 with the drone in B). Figures partly adapted from Seifried et al., 2021 [123].

To gain information about the emission of bioaerosols, the investigated air parcel was divided into zones as drawn in Figure 3.8, A. The first sampling zone (Z1) was above the alpine lake around 130 m off shore, since the air above the lake is assumed to be mixed well and referred to the general concentration within the air parcel. Zone 2 (Z2) was chosen to be above the canopy of the birches (primary emission source) and zone 3 (Z3) was in a height of around 45 m. During UA3, UA4 and UA5 an additional ground-based zone below the canopy of the birches (Z0) was added to the procedure since the weather was likely to induce the emission of fungal spores and other bioaerosols from soil. A picture of the drones' sampling flight in Z2 is shown in Figure 3.8, B. A video of the drone flying during the sampling procedure is uploaded in the digital attachment of Bieber et al., 2020[b].

[b]Download under `http://doi.org/10.5281/zenodo.3588399`

Table 3.1.: Flight data of the field campaign including two sampling periods (UA1-UA2 and UA3-UA5).

Sample ID	Date	Approached Zone	Start Time (CEST)	Duration [min]	Flow-Rate ± SD [L min^{-1}]	Sampled Air Volume [L]
UA1 Imp1	3 June 2019	1	17:30	10	1.05 ± 0.03	10.5
UA1 Imp2	3 June 2019	2	16:30	10	1.01 ± 0.03	10.1
UA1 Imp3	3 June 2019	3	19:00	10	1.10 ± 0.03	11.0
UA1 CI1	3 June 2019	1	17:30	10	9.02 ± 0.28	90.2
UA1 CI2	3 June 2019	2	16:30	10	8.99 ± 0.10	89.9
UA1 CI3	3 June 2019	3	18:30	10	9.10 ± 0.03	91.0
UA2 Imp1	4 June 2019	1	19:23	10	1.05 ± 0.05	10.5
UA2 Imp2	4 June 2019	2	17:34	10	1.00 ± 0.01	10.0
UA2 Imp3	4 June 2019	3	18:22	10	1.09 ± 0.03	10.9
UA2 CI1	4 June 2019	1	19:11	10	9.01 ± 0.08	90.1
UA2 CI2	4 June 2019	2	17:34	10	9.03 ± 0.03	90.3
UA2 CI3	4 June 2019	3	18:22	10	8.98 ± 0.04	89.8
UA3 Imp0a	21 August 2019	0	18:50	10	1.00 ± 0.03	10
UA3 Imp0b	21 August 2019	0	19:23	50	1.00 ± 0.03	50
UA3 CI0a	21 August 2019	0	18:50	10	8.92 ± 0.04	89.2
UA3 CI0b	21 August 2019	0	19:23	50	8.92 ± 0.04	446
UA4 Imp0	22 August 2019	0	20:01	50	1.07 ± 0.04	53.5
UA4 Imp1	22 August 2019	1	18:48	10	1.07 ± 0.04	10.7
UA4 Imp2	22 August 2019	2	18:28	10	1.07 ± 0.04	10.7
UA4 Imp3	22 August 2019	3	19:25	10	1.07 ± 0.04	10.7
UA4 CI0	22 August 2019	0	20:01	50	8.94 ± 0.06	447
UA5 Imp0	23 August 2019	0	19:54	10	1.08 ± 0.02	10.8
UA5 Imp1	23 August 2019	1	18:55	10	1.08 ± 0.02	10.8
UA5 Imp2	23 August 2019	2	19:10	10	1.08 ± 0.02	10.8
UA5 Imp3	23 August 2019	3	19:25	10	1.08 ± 0.02	10.8
UA5 CI0	23 August 2019	0	19:15	50	9.08 ± 0.06	454

3.4. Analytics

The analytical part of the thesis was split into two sections which include the analysis of the Imp samples (described in Section 3.4.1 and 3.4.2) and the analysis of the CI samples (described in Section 3.4.3 to 3.4.5).

3.4.1. Freezings Assays

In general, a heterogeneous freezing assay involves the analysis of a given particle ensemble interacting with water molecules and triggering the freezing process (e.g., by immersion freezing, pore condensation freezing, etc.) either *in-situ* or *in-vivo*. During this thesis, the focus was led on the analysis and characterization of IN within bioaerosols sampled with DAPSI. Thus, *in-vivo* immersion freezing assays were the method of choice. Two different assays have been applied to investigate environmental samples. The Vienna optical droplet crystallization analyzer (VODCA) enables a microscopic measurement of IN in a cloud-like emulsion on a cold stage (pL assay), while the twin-plate ice nucleation assay (TINA) provides a higher droplet volume (µL assay) and thus, a better method for samples with lower IN number concentration. Both methods are described in detail below.

Vienna Optical Droplet Crystallization Analyzer

To analyze the activity of IN in microscopic droplets, the VODCA setup provides a cold stage cooling technique, where an oil/water emulsion is created to observe freezing via a light-microscope (Olympus BX, Japan). A self-built cryo-cell was placed under a microscope. This cell, which is depict in Figure 3.9, includes a Peltier-element (High Tech Peltier-element, Quick-cool QC-31-1.4-3.7M, Qick-OHM Küpper and Co, Germany), that cools the sample during the analysis. The temperature of the surface from the Peltier-element is measured using a thermo-couple (PCE-T312 typ K, PCE, Germany) which is mounted with thermo-glue (Wärmeleitkleber, WLK DK10, Fischer Elektronik, Germany). The Peltier-element is driven by an external power supply (DP831 A LXI, Rigol, USA), which is controlled via a LabView© software. An additional cooling circuit is installed, to cool the heated side of the Peltier-element. This includes a cooling block made of copper (see Figure 3.9, A) and an aquarium pump (universal water pump, EHEIM, Germany), which transfers ice cooled water from a reservoir into the cryo-cell (the general circiut is shown in Figure 3.9, B). Within the closed cryo-cell (see Figure 3.9, C) an inert environment can be generated by flushing the cell with dry nitrogen gas. To avoid water condensation on the glass window during cooling a nozzle is placed at the outside of the cell directing compressed air onto the window. For performing a measurement, 2 µL of the sample are pipetted on a glass slide (Menzel-Gläser, VWR, international, USA). Thereafter, 4 µL of an oil mixture (90 wt.% paraffin, AppliChem, Germany and 10 wt.% lanoline, Acros Organics, USA) are added and an emulsion is created by stirring the phases with a pipette tip. The slide is placed onto

the surface of the Peltier-element and thereafter, the cryo-cell is closed and flushed with nitrogen gas for 5 minutes. After adjusting the focus of the microscope to a spot of interest, the cooling program is started and the experiment is recorded via a digital camera (MDC320 microQ L3CMOS, Hengtech, Germany). The cooling rate was chosen to be 10°C min^{-1}, assuming that immersion mode ice nucleation is a time independent process. The freezing of the droplets is observed manually by the change of the optical density (see Figure 3.10, A). High concentrated samples have been diluted prior to the measurement to evaluate the cumulative nuclei concentration as explained later.

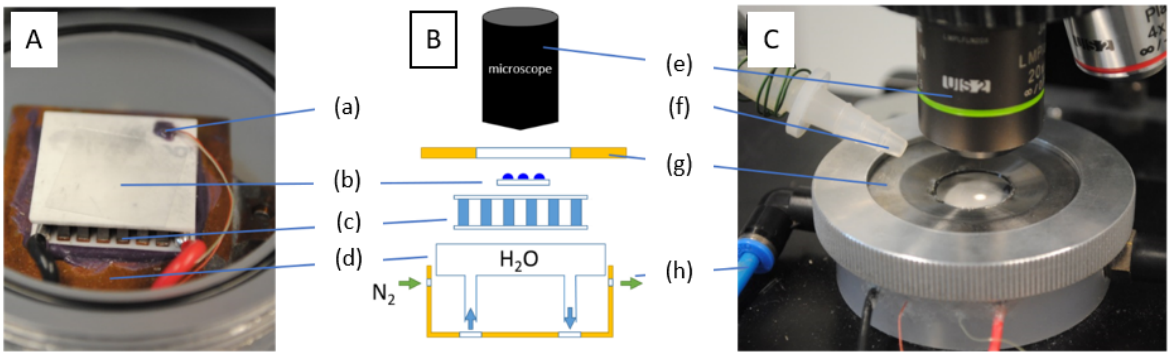

Figure 3.9.: The Vienna optical droplet crystallization analyzer (VODCA) setup: A) Peltier-element with glass slide, B) Schematic drawing and C) Closed cryo-cell during a measurement. Components: (a) Thermo-couple, (b) Glass-slide, (c) Peltier-element, (d) Copper block, (e) Microscope, (f) Air nozzle, (g) Cap of the cell with glass window, (h) Cooling circuit.

Twin-plate Ice Nucleation Assay

TINA is a freezing setup that enables the observation of ice nucleation in microliter-sized droplets. A detailed description of the setup is given in the paper Kunert et al., 2018 [126]. In brief, 96-well plates are used to cool droplet-aliquots (3 µL) of the sample solutions. The 96-well plates are cooled with an aluminum block that is tempered by fully automated refrigerant circulation loops in highest precision (uncertainty < 0.2 K). The cooling rate is set to 1°C min^{-1} and the end-temperature to -30°C. Freezing events are observed via an infrared camera, since every supercooled droplet releases latent heat when the freezing process is triggered (see Figure 3.10, B).

Filtration

Filtration experiments are performed to evaluate the sizes of IN present in the Imp samples. Therefore, the samples are pressed through a 0.1 µm syringe filter prior to the freezing experiment. To gain information about to content of macromolecular IN, the samples are filtered with 300 kDa and 100 kDa spin tube filters prior to the analysis with TINA.

Heat Treatment

Biological IN are typically heat unstable due to the degradation of heat sensitive biomolecules [12]. Thus, the biological content of the Imp sample can be estimated by measuring the ice nucleation activity before and after exposing the sample to heat treatment. To do so, an aliquote of the sample solutions is pipetted into Eppendorfer tubes and incubated for 1 h at 98°C in an incubation bath.

3.4.2. Evaluation of Freezing Assays

To evaluate the freezing experiments of both, VODCA and TINA, the droplets that froze at a given temperature are counted. In case of VODCA experiments, the fraction of frozen droplets, $f_{ice}(T)$, is evaluated manually by counting droplets with a diameter between 15 to 40 µm at the time the optical density changes, as shown in Figure 3.10, A (red circles).

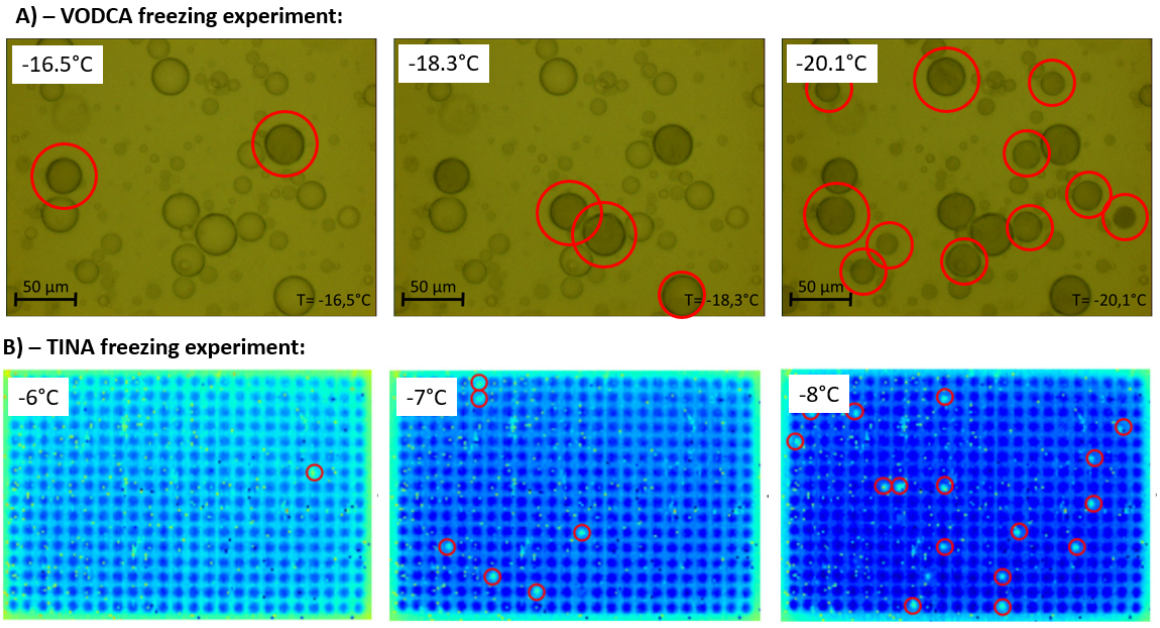

Figure 3.10.: Evaluation of the freezing assays: A) Droplets change their optical density when water turns to ice. Frozen droplets are counted (encircled red) via a microscope. B) Droplets release latent heat that can be detected via an infrared camera (encircled red). Figure adapted from Kunert el al., 2018, [126].

Thereafter, every time a droplet freezes, one data point, $f_{ice}(T_i)$, at a given temperature, T_i, is generated. An example spectrum is shown in Figure 4.2, A, in Section 4.1.2, whereat a differentiation between homogeneous freezing and heterogeneous freezing can be clearly made. The evaluation of a TINA experiment is quite similar, with the distinction that the droplets are detected via an infrared camera and counted fully automatically. Infrared pictures of the 96-well plate during a TINA experiment are shown in Figure 3.10, B. The

latent heat (light blue) of each droplet gets detected (encircled red) and frozen droplets are counted. An example of TINA spectra is given in Figure 4.6 where the background noise is higher due to the higher droplet volume compared to VODCA (more impurities in one droplet). Thus, the distinction between homogeneous and heterogeneous ice nucleation is rather difficult. However, the higher volume results in a better quantitative analytic for lower concentrated samples as seen later in Section 4.3.1.

To evaluate the number concentration of IN, the cumulative nucleus concentration $K(T)$ as explained by Vali, 1971, [127] is calculated by

$$K(T) = -\frac{ln(1 - f_{ice}(T))}{V_D} D \tag{3.2}$$

where V_D is the average volume of analyzed droplets in the freezing assay (8.2 pL for VODCA and 3 µL for TINA), D the dilution factor and $f_{ice}(T)$ the fraction of frozen droplets at a given temperature (ratio of frozen droplets at T to the total number of droplets at the end of the experiment). An example spectrum of the cumulative nuclei concentration is given in Figure 4.2, B. To refer $K(T)$ to the actual number concentration of IN in atmospheric air, Equation 3.2 is modified as

$$n_{IN} = -\frac{ln(1 - f_{ice}(T))}{V_D} D \frac{V_{Imp}}{V_{air}} \tag{3.3}$$

where V_{Imp} is the volume of water in the Imp (15 mL) and V_{air} is the volume of air that has been sampled. V_{air} is a function of the flow-rate and sampling time (calculated values of V_{air} are given for each sample in Table 3.1).

Background Correction

Since some samples froze in the region of the water background of the TINA instrument, we performed a background correction as explained by David et al., 2019 [128]. In a first step the fraction of frozen droplets obtained from the experiment was binned into 0.2 °C bins. Furthermore, the differential nucleus concentration, $k(T)$, [127] is calculated for the samples and the background water by

$$k(T) = -\frac{1}{V\Delta T} \ln(1 - \frac{\Delta N}{N(T)}) \tag{3.4}$$

where V is the volume of the droplets, ΔT is the temperature interval of the bins (0.2 °C), ΔN the number of droplets that froze in that interval and $N(T)$ is the number of unfrozen droplets at the beginning of a temperature bin.

Thereafter, the background values are subtracted from the sample nucleus concentration as followed by

$$k_{cor}(T) = k_{sample}(T) - k_{background}(T) \tag{3.5}$$

Hence, the corrected frozen fraction $f_{cor}(T)$ can be obtained by subtracting $k(T)$ from Equation 3.4 with the values obtained for $k_{cor}(T)$ and transformation of the equation. Finally, $f_{cor}(T)$ is using for the calculation of the number concentration as stated above in Equation 3.3.

Calculation of the Error

To calculate the uncertainties of the freezing assay one must include the counting error in an Gaussian error propagation. This was performed as described in detail by Kunert et al., 2018 [126]. The uncertainty is illustrated by error bars in the results of the quantitative investigations. Data points with uncertainties higher than 100% were excluded from the diagram.

3.4.3. Microscopy

The collected CI foils are analyzed using microscopic techniques, i.e., fluorescence microscopy and scanning electron microscopy (SEM). Since many biogenic aerosols show auto-fluorescent characteristics [129], no staining or amplification procedures are performed prior to the analysis. SEM requires the sample to be an conductor and thus, a sputtering procedure was necessary as explained in the subsection. We performed fluorescence microscopy with all samples (UA1 to UA5), while a particular day of interest (UA4) was chosen to be analyzed further via SEM.

Fluorescence microscopy

The experimental part of fluorescence microscopy was published in Bieber et al., 2020 and is adapted from the paper [120]: The used fluorescence microscope consists of a 100 W metal-halide light source (Nikon Eclipse Ci-L, Nikon, Japan), a color-digital camera (DS-Fi3, Nikon, Japan) and several objectives (Plan Apo, 10x and 40x, Nikon, Japan). A Nikon software (NIS-Elements) is used to control the camera. An epifluorescence unit is used with an excitation filter at 465 to 495 nm, a dichromatic mirror at 505 nm, and an emission filter at 515 to 555 nm. A blank sample (heat-treated foils without particles) was recorded and showed a dark background (see Appendix C, Figure C.1). Foils from the field campaign are analyzed with different objectives chosen to picture the particles of interest. Optical adjustments in greyscale are performed in analog and digital functions to optimize the intensity.

Theoretical note:

Fluorescence is known as the photo-physical process at which electrons get excited after the absorption of photons and photons get re-emitted with longer wavelength during the relaxation process of the electron. The Jablonski diagram of the corresponding energy states is shown in Figure 3.11, A. An electron, which is situated in a singlet ground state (S_0) absorbs the energy of an incoming photon ($h\nu_A$). Thereafter the electron gets excited to a higher quantum state (e.g., S_1 or S_2) and internal energy conversions (i.e., vibrational energy transfer) can take place. Afterwards, the electron relaxes to ground state and emits a fluorescence photon ($h\nu_F$). When intersystem crossings occurs, a triplet state gets occupied and after relaxation a phosphorecence photon is emitted ($h\nu_P$). A more detailed description is given in literature [130]. Fluorescence microscopy benefits from the energy shift between the excitation light beam and the emission light beam, called Stokes shift [131]. The apperature, which is drawn in Figure 3.11, B, focuses a polychromatic light beam from a lamp via aperture- and field-diaphragm to a filter cube. First, the light beams wavelength is filtered with the excitation filter. Then, the beam hits a dichromatic mirror which reflects the short wavelenghts to be focused on the microscopic table where the specimen is placed. Fluorescence molecules, that can either be from the sample itself (auto-fluorescence), or foreign fluorescence markers, emit light with higher wavelength, that is lead back to the filter cube and passes the dichromatic mirror. After passing an emission filter, the lightbeam is recognized via the operators eye or a camera suited on top of the microscope.

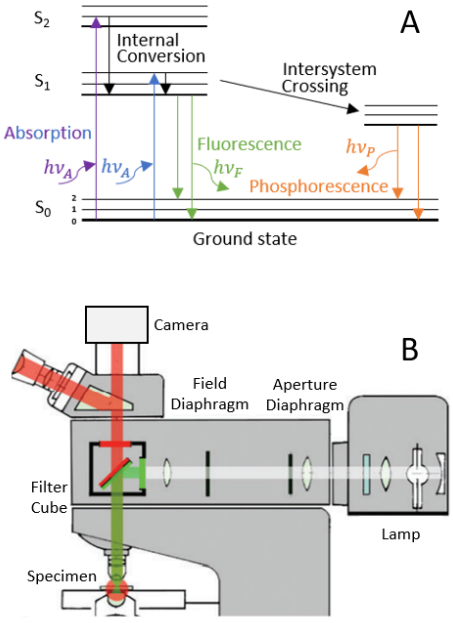

Figure 3.11.: Principles of fluorescence microscopy: A) Jablonski diagram of electrons that get excited by absorbing the energy of photons ($h\nu_A$) and emit fluorescence photons ($h\nu_F$) or phorsphorescence photons ($h\nu_P$) during relaxation. B) Principal construction of a fluorescence microscope, adapted from Lichtman and Conchello, 2005, [131].

Scanning Electron Microscopy

The CI samples of UA4 have been analyzed using SEM, since the number concentration of particles on the foils was the highest compared to other samples (observed via fluorescence microscopy). To analyze biological particles on the collected CI foils, the samples are sputtered with an Au/Pd layer. Afterwards, the samples are analyzed using a microscope of the type FEI Quanta^{TM}200 FEGSEM. In the following *Theoretical note* the principles and advantages of SEM are described.

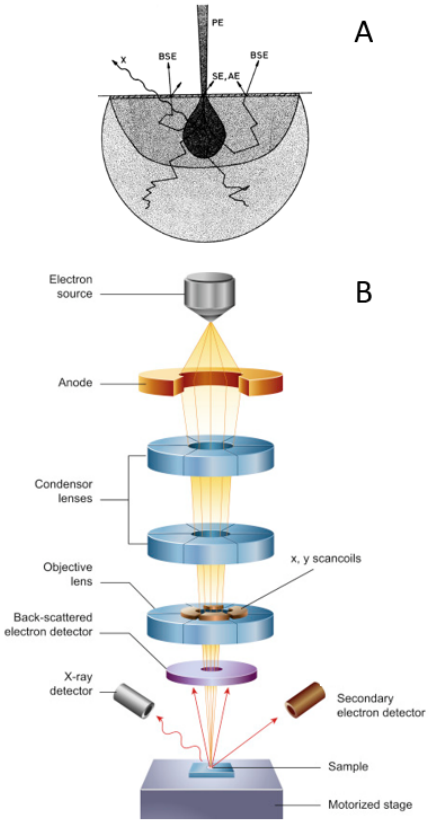

Figure 3.12.: Principles of scanning electron microscopy (SEM): A) Primary electrons (PE) interacting with matter and producing backscattered electrons (BSE), secondary electrons (SE), Auger electrons (AE) and X-rays (X), adapted from [132]. B) Principal construction of a SEM apperature, adapted from [133].

Theoretical note:

The maximal resolution of a microscope is limited by the point at which the observed beams of two objects start to interfere and the resulting observed signal is a result of interference. Thus, the Abbe diffraction limit, described by Ernst Abbe in 1873, is stated as

$$d = \frac{\lambda}{2n \sin \theta} \tag{3.6}$$

where λ is the wavelength of the interfering beams, n is the refractive index, θ the angle between the beams and d the minimum distance between two resolved points. With that limit, the resolution of microscopy using photons (e.g., $\lambda = 500$ nm for green light) as surface-probes is set to around 0.3 µm. The idea of SEM is the usage of electrons ($\lambda \approx 1$ pm) instead of photons to reduce the diffraction limit tremendously. When a focused beam of primary electrons (PE) interacts with matter, several phenomena can be observed as illustrated in Figure 3.12, A. As a result, back scattered electrons (BSE), inelastic scattered secondary electrons (SE), Auger electrons (AE) and X-ray photons (X) are emitted from the sample [132]. All generated signals can be measured while the collection of SE is the easiest due to their low exit energy. This is from general interest for microscopic surface imaging while the detection of X-rays, BSE or AE reveals chemical information of the specimen. Within the apperature of SEM, electromagnetic lenses (condensor lenses and objective lens) focus PE very sharp on a nanometer sized spot on the samples surface (as seen in Figure 3.12, B). By collecting SE from this particular spot and further scanning the surface with the PE beam in two dimensions, the observation of nm-sized objects becomes achievable. A more detailed description is given in literature [132–134].

3.4.4. Particle Distribution Analysis

Particles on CI foils of UA4 have been counted in several sections on the images to determine the concentration of aerosol particles in the sampled air and resolve the distribution of particle diameters. Therefore, the particles of three randomly picked 200 µm x 200 µm sections of the fluorescence and SEM images from PAC-UA4-A have been counted manually using the software ImageJ©. For stage D, the particle diameter was too small to measure it accurate with fluorescence images (limited by the Abbe diffraction limit). Thus, only SEM measurements were taken into account and one 10.2 µm x 6.8 µm zoomed SEM-image with high resolution from PAC-UA4-D was used to count particles. Encircling the particles and measuring the area with the software enabled the determination of the particle surface diameter (d). For stage A, the particles were counted in 1 µm bins while for stage D the bin interval was 50 nm. The counted number per area of the segment was multiplied by the overall area on which particles did impact (measured manually using ImageJ©) and furthermore divided through the volume of sampled air. To compare the observed aerosols with literature the concentration is normalized to the size of the bins ($dN/dlogp$) and a logNormal function is fitted using Origin©. Integrating the fitted LogNormal distribution functions gives the number concentration for coarse-mode (diameter of 1 µm to 10 µm) and accumulation-mode (diameter of 0.05 µm to 1 µm).

3.4.5. Single Particle Analysis

Microscopic images of fluorescence microscopy and SEM were overlapped using the software Gimp©. Therefore, images of both methods from the same spot were taken into account. The dark background of the fluorescence image was removed and turned into transparency. Afterwards, the images ware placed in the same position and the final image which is shown in Section 4.4.4, Figure 4.12 A was recorded. The original images can be seen in Appendix D, Figure D.1. Single particle analysis (SPA) was performed by characterizing particles into fluorescence and non-fluorescence particles. Fluorescent particles were subdivided by optical observations into different shape categories.

4. Results and Discussion

4.1. Sampling Efficiency

The sampling efficiency for the self-built Imp has been tested for coarse-mode (2.0 µm) and accumulation-mode (600 nm) PSL spheres and for biogenic IN, as explained in Section 3.2.

4.1.1. Polystyrene Latex Spheres

The recorded aerosol number concentration spectra for sampling PSL spheres, over a time interval of 10 min, are depicted in Figure 4.1, where in A the measured values for 2 µm PSL and in B the spectra for 600 nm PSL are shown. The blue lines represent the concentration which was measured without using an Imp in the flow-line, while the orange line states the concentration of the generated aerosol when using an Imp (i.e., the aerosol concentration at the exit of the impinging system). For both experiments the concentration decreased about one order of magnitude within the area of interest (marked with gray lines). The high concentration in spectra of A at small diameters (outside the interval) originates from either residues of the water which was used in the experiment or from PSL spheres that break during the aerosolization process leading to smaller fragments.

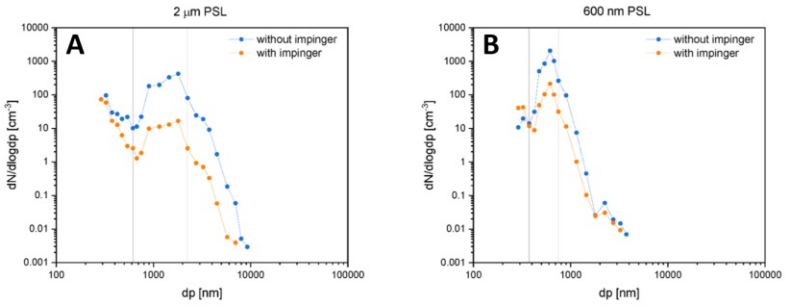

Figure 4.1.: Sampling efficiency of the impinger measured in the laboratory using A) 2 µm PSL and B) 600 nm PSL. Figures adapted from Bieber et al., 2020 [120].

Moreover, the efficiency can be calculated by integrating the concentration over the marked interval (vertical gray lines) and further by using

$$E = \left(1 - \frac{C_2}{C_1}\right) 100\% \tag{4.1}$$

where C_2 is the number concentration of the aerosol with Imp, C_1 is the concentration without using an Imp and E is the resulting sampling efficiency. For the coarse-mode,

the starting concentration was 116 cm^{-3} and the concentration after the Imp was 5 cm^{-3} resulting in an efficiency of **96% for 2.0 µm PSL**. For the accumulation-mode the efficiency was calculated with 263 cm^{-3} as starting number concentration and 28 cm^{-3} after the Imp, which led to an efficiency of **89% for 600 nm PSL**. Thus, a size dependency can be assumed for the developed system. However, the self-built Imp samples coarse-mode and accumulation-mode with sufficient efficiency. The results accompany with literature data of a similar impinging system that was introduced by Powers et al., 2018 where an efficiency of 99% and 75% was observed for 3.0 µm and 1.0 µm PSL spheres [113].

4.1.2. Biogenic Ice Nuclei

In addition to idealized aerosols, the efficiency was determined with biogenic aerosols that nucleate ice at heterogeneous temperatures (i.e., BPWW of *Betula pendula*). In contrast to the determination of the concentration of PSL, the concentration of IN in the sampled solution of two Imp in a row where compared to each other. In Figure 4.2, A, the freezing spectra are shown for the sample of the first Imp (blue), the second Imp (orange), for BPWW and pure water as reference (purple and gray). The cumulative nucleation spectra (calculated using Equation 3.2) are shown in Figure 4.2, B, where a difference between the blue (first Imp) and orange curve (second Imp) is observed. Using the cumulative concentration at the end of the freezing spectra (K_1(-34 °C) = 0.89 pL^{-1} and K_2(-34 °C) = 0.14 pL^{-1}) as concentration in Equation 4.1 results in a sampling efficiency of **84% for biogenic IN**.

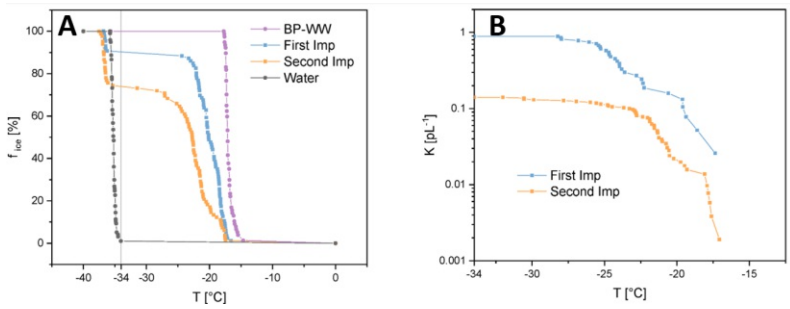

Figure 4.2.: Sampling efficiency of the Imp system measured in the laboratory using biological IN of *Betula pendula*. A) Freezing spectra of the first and second impinger (Imp) in a row. Water and birch pollen washing water (BPWW) are plotted as a homogeneous freezing and a heterogeneous freezing reference. B) Corresponding cumulative nuclei concentration ($K(T)$). Figures adapted from Bieber et al., 2020 [120].

4.2. Sensor Data

The data recorded during the flights of the impinging system included the particle mass concentration ($PM_{2.5}$ and PM_{10}), temperature, relative humidity and air pressure. One example of three flights from the second sampling day (UA2) is shown in Figure 4.3 where the recorded values are shown in lines with different colors over a time period that expanded over the sampling period (vertical gray lines).

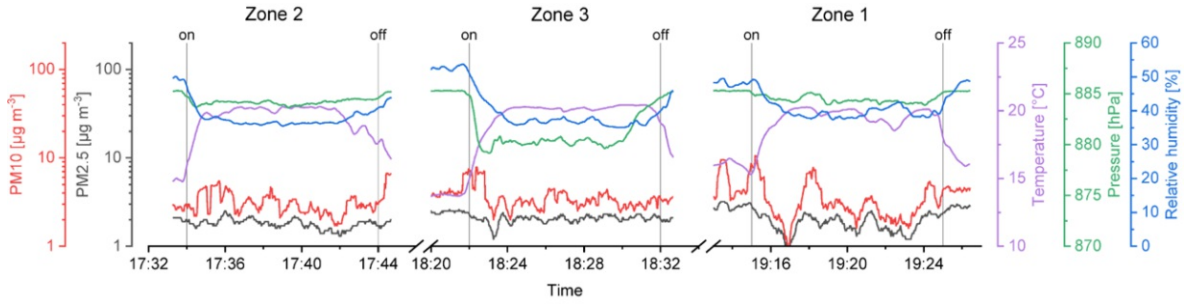

Figure 4.3.: Sensor data from the second sampling day (UA2) as an example. The measured values (PM_{10}, $PM_{2.5}$, temperature, relative humidity, pressure) are plotted as recorded against the time axis. Vertical lines mark the time boarders of the sampling interval. Figure adapted from Bieber et al., 2020 [120].

The measured particle concentrations vary between 1 and 10 µg m^{-3} for both, $PM_{2.5}$ and PM_{10}. The temperature increases when the flight starts and the UAV lifts off (pressure decreases). This effect is explained by the snow that covered the land surface during the first sampling days and cooled the air above the ground. Furthermore, the relative humidity decreased during the flight, supporting the theory about the snow leading to a cool wet air parcel above the snow surface. In Figure 4.4 all relevant data recorded with the ESM and the OPC during the campaign are summarized. In addition to the measured temperature and relative humidity, the calculated temperature and humidity gradient and the amount of rainfall are depicted (Figure 4.4, A and B) [a]. These data are calculated for the spot of interest in dependency of the historical weather data recorded with weather stations in the surrounding environment. The measured values broadly match the provided weather data. In more detail the maximal deviation of the relative humidity between the measured and calculated data ranges was 18% (UA3 Z0a) while the maximal temperature deviation was 3.0°C (UA1 Z2). Generally, the measured values tend to be lower than the calculated data. The deviations can be described by systematic errors of the ESM (3% according to the manufacturer) and/or errors in the calculated data. However, the general trend within one measurement day is predicted very precise by the onboard ESM, e.g., as seen for UA4 (Figure 4.4, B).

[a] Data provided by Meteoblue.

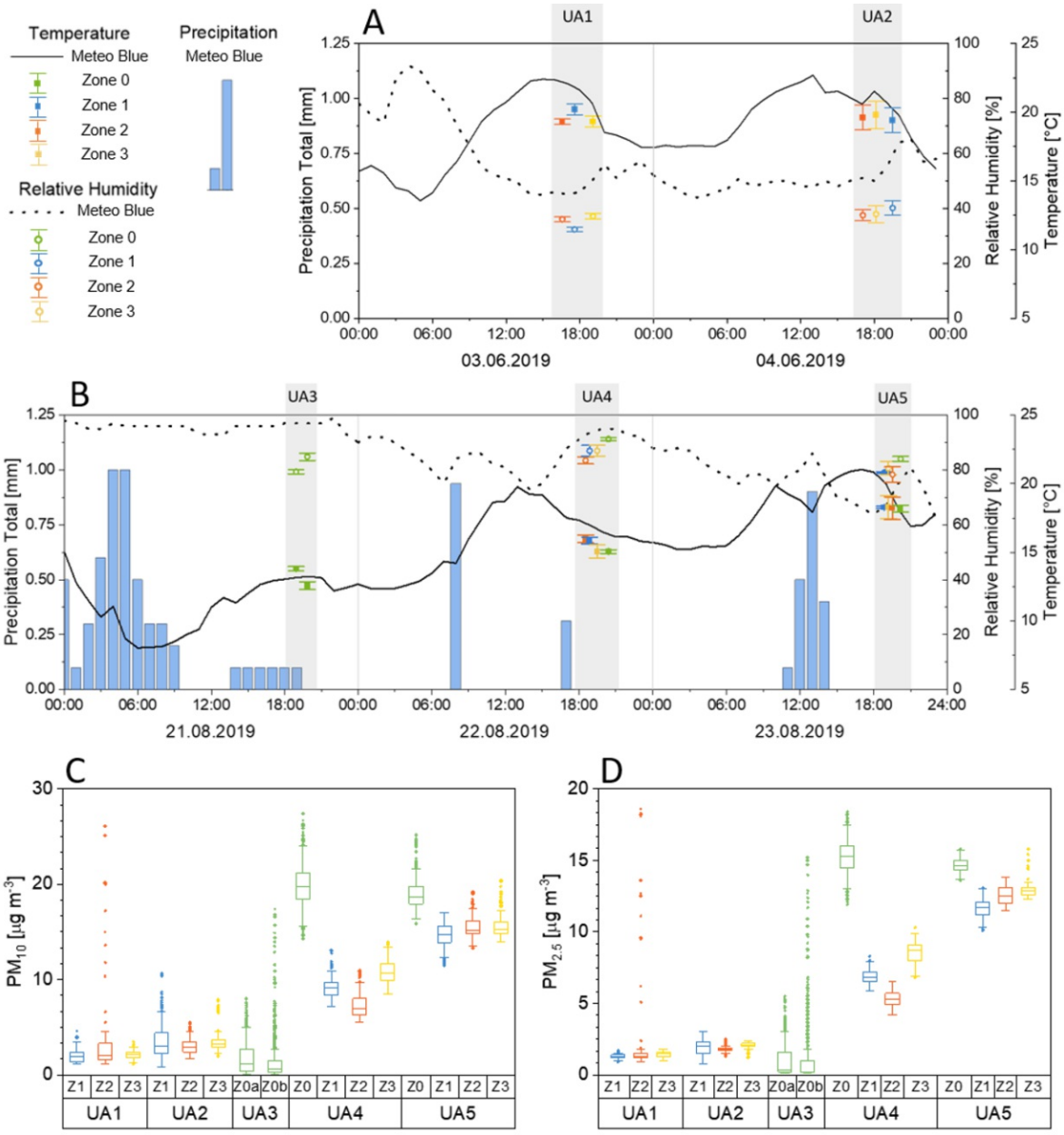

Figure 4.4.: A) and B) Graphs showing the temperature (black solid line), relative humidity (dashed lined) and precipitation (blue bars) gradient against the time of the days (3rd June 2019, 4th June 2019, 21st August 2019, 22nd August 2019 and 23rd August 2019). Data calculated in dependency of measured data in the area of interest was provided by Meteoblue. Measured sensor values and standard deviations of the sampling periods (marked with gray bars) are plotted as hollow circles for relative humidity and full circles for temperature. Sampling zones are marked in different colors (zone 0 = green, zone 1 = blue, zone 2 = orange and zone 3 = yellow). A) Data from the sampling periods UA1 and UA2; B) Data from the sampling periods UA3, UA4 and UA5; C) and D) Graphs showing the particulate matter (PM) sensor data (median, 25% and 75% quartiles, outliers). C) PM_{10}; and D) $PM_{2.5}$. Figures partly adapted from Seifried et al., 2021 [123].

On the first two days of the field campaign (UA1 and UA2) the temperatures were higher and the relative humidities were lower compared to UA3, UA4 and UA5 (Figure 4.4, A and B). On these early spring days the sky was cloudless and the sun was shining to the spot of sampling. During UA3, UA4 and UA5 the weather was dominated by rainfall events. In more detail, the strongest precipitation was observed on UA3, where the rainfall continued over the measurement periods (no drone flights were possible). On UA4 and UA5 the sampling took place directly after the rainfall periods when relative humidity started to increase (around 80%) and temperature decreased (< 20°C). Additionally, the sky was covered with clouds, reducing the radiation impact on the vegetation, and the environment above the location was foggy most of the sampling time.

The PM_{10} and $PM_{2.5}$ values for the campaign are shown in Figure 4.4, C and D as box plots. On the sunny spring days (UA1 and UA2) the measured values are around 2.5 µg m^{-3} for PM_{10} and around 1.5 µg m^{-3} for $PM_{2.5}$. A sharp increase of outliers was detected during UA1-Z2 (up to 120 µg m^{-3}, not completely shown in the diagram). This peak could originate from emissions of aerosols (bioaereols or mineral dust) induced either by natural wind or downwash from the drones' rotor blades. Furthermore, the PM_{10} values of UA1 and UA2 show a higher amount of outliers compared to $PM_{2.5}$, highlighting fluctuations of particles in the size range between 10 µm and 2.5 µm. During the rainfall the median PM_{10} values were < 2 µg m^{-3} and < 1 µg m^{-3} for $PM_{2.5}$. However, on this particular day the deviations and the amount of outliers was at its highest, highlighting turbulent fluctuations during the impact of rain droplets on the ground and vegetation surface. **After rainfall (UA4 and UA5) the PM_{10} and $PM_{2.5}$ concentrations increased tremendously.** The medians reached from around 5 µg m^{-3} to 15 µg m^{-3}. In particular, the concentration was highest during ground sampling (Z0) and decreased in the flight zones (Z1, Z2 and Z3), indicating that the land surface was the primary emission source causing these peaks. According to statistical testing (t-test inclusive Welch correction), the batched values of Z1, Z2 and Z3 from UA1 and UA2 differ significantly from UA4 and UA5, for both, PM_{10} and $PM_{2.5}$. A burst of biogenic aerosol concentrations after rainfall events has been described in various literature data [110, 124, 135–137] often linked to the theory of the bioprecipitation cycle [138]. Moreover, the concentration during the rainfall event (UA3-Z0a,b) was significant lower than after the rainfall (UA4-Z0 and UA5-Z0). This effect can be described by scavenging effects of rain showers on aerosols [139, 140], where aerosol particles are washed out during rainfall by rain droplets.

4.3. Ice Nucleation Activity of Atmospheric Samples

4.3.1. Freezing Behavior

The ice nucleation activity for the first sampling days (UA1 and UA2) was measured using the VODCA setup at TU Wien, whereas samples of the second sampling days (UA3, UA4 and UA5) where measured with the TINA setup by the Max Planck Institute (Section 3.4.1). The resulted spectra for all samples of UA1 and UA2 are shown in Figure 4.5 where several sample types (Imp1 to Imp3) are plotted in different colors. Blue color refers to Z0, green to Z1 and orange to Z3. The ratio of frozen droplets at a given temperature to the total number of observed droplets (f_{ice}) is plotted against the temperature T in a logarithmic scale. In addition to the samples, spectra of diluted BPWW (0.05 µg mL^{-1}) and ultra pure water are plotted as reference and blank. The vertical gray line marks the boundary between homogeneous and heterogeneous ice nucleation in this experiment. Four out of six samples showed heterogeneous ice nucleation (onset temperature between -27.4°C and -30.6°C) in a few droplets of the ice nucleation experiment (between 5.6% and 10.6%). Thus it can be confirmed, that active IN have been sampled during UA1 and UA2, above the lake and above the canopy of the birches, but primary biological IN show typically much higher onset temperatures. However, inorganic IN (e.g. mineral dust) or SOA could be responsible for the heterogeneous ice nucleation within the samples [141, 142]. For a quantification of the IN concentration the signal was too low since we chose the diluted BPWW as lowest limit of quantification (LOQ).

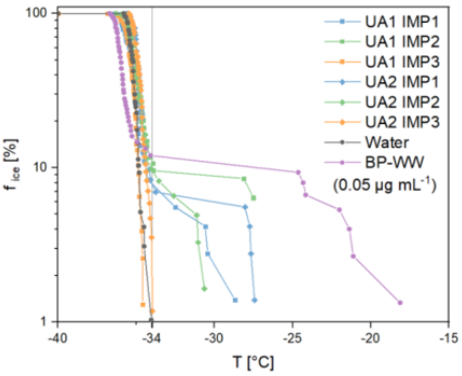

Figure 4.5.: Freezing spectra recorded with VODCA. Freezing events are plotted on a logarithmic scale against the temperature. Samples from several days and sampling zones (UA1 and UA2, Imp1 to Imp3) are shown in different colors. Additionally, the freezing curve of diluted birch pollen washing water (BPWW) and water from MilliQ system are plotted as references. Figure adopted from Bieber et al., 2020 [120].

During the second part of the field campaign (UA3, UA4 and UA5) no heterogeneous nucleation events were observed for samples measured with the VODCA technique. To increase the limit of detection (LOD) and the LOQ, measurements were performed using the TINA setup, whereat the droplet volume is higher by six orders of magnitudes. Thus, the number of IN in the experiment is higher, which results in an elevated ice nucleation activity. Hence, the ice nucleation activity of lower concentrated samples can be qualified and quantified more precisely. In Figure 4.6 A, B and C, the freezing spectra for the three sampling days (UA3, UA4 and UA5) are shown where again f_{ice} is plotted against T. Every day included samples with positive heterogeneous nucleation measurements. Even though the blank sample shows heterogeneous freezing with the TINA assay (lower LOD revels IN in the blank), the samples

UA3-Imp0b, UA4-Imp0, UA4-Imp2, UA4-Imp3, and UA5-Imp0 clearly distinguish from the background concentration. The onset temperature varied from about -14°C to -22°C, while the shape of the curves indicate that the samples from Z0 of day 4 and 5 froze completely heterogeneous without diluting the samples. The temperature level at which the fraction was frozen to 50% (T_{50}) was -26.3°C for UA3-Imp0b, -20.3°C for UA4-Imp0, -27.2°C for UA4-Imp2, -25.8°C for UA4-Imp3 and -21.8°C for UA5-Imp0. Furthermore, the samples from Z0 of UA4 and UA5 show a sharp increase around -20°C, indicating the main source of IN to be active around that temperature, while UA4-Imp2 and UA4-Imp3 show an increase at lower temperatures. The sample from UA3-Imp0b exhibits a lower gradient, however the presence of IN with high onset temperatures is highlighted.

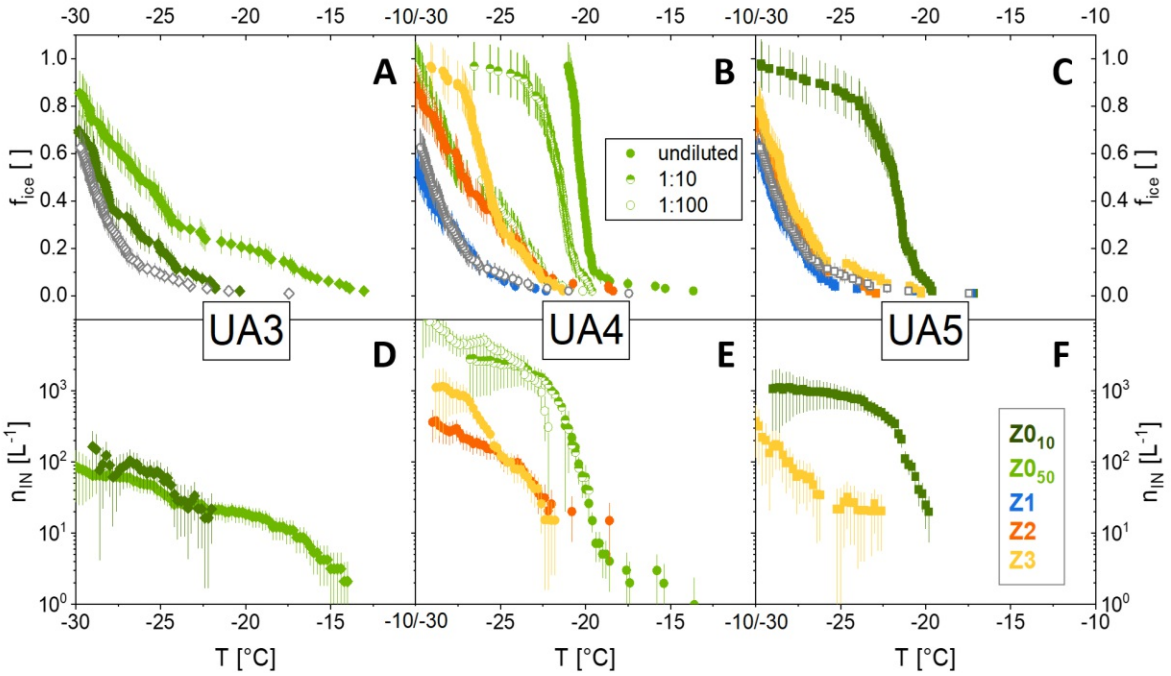

Figure 4.6.: Freezing spectra recorded with TINA. A),B) and C) Fraction of frozen droplets are plotted against the temperature. Samples from several days and sampling zones (UA3, UA4 and UA5 and Z0 to Z3) are shown in different colors. Additionally, the background corrected IN number concentration is plotted in D), E) and F). Figure partly adapted from Seifried et al., 2021, [123].

By using Equation 3.2 (stated in Section 3.4.2), the calculation of the cumulative nuclei concentration can be performed. By multiplying *K(T)* with the volume that was used in the Imp (15 mL) and further dividing through the sampled air volume (stated in Table 3.1) the concentration is referred to the environment (see Equation 3.3). Furthermore, a background correction was performed as stated in Section 3.4.2. Curves representing the corrected number concentrations of IN are shown in Figure 4.6, D, E and F. In the ground-based sample from day 3 (UA3-Imp0b), IN with high onset temperatures (> -15°C) are present at about 3.2 10^0 L^{-1}. At lower temperature (> -24°C) the cumulative number of IN reached 2.6 10^1 L^{-1}

for UA3-Imp0b, 2.2 10^3 L^{-1} for UA4-Imp0, 8.4 10^1 L^{-1} for UA4-Imp2, 7.8 10^1 L^{-1} for UA4-Imp3 and 7.5 10^2 L^{-1} for UA5-Imp0. At the end of the range which can be measured using TINA (-30 °C) the concentration reaches from 9.4 10^1 L^{-1} to 1.6 10^4 L^{-1} for the lowest concentrated sample that shows heterogeneous freezing above the blank (UA3-Imp0b) to the highest concentrated (UA4-Imp0). Comparing the days with each outer leads to the cognition that **on UA4 a plume of IN can be highlighted whereat IN_{-24} are emitted in high number concentrations (>10^3 L^{-1}) from the land surface (Z0) and diluted during transportation to the canopy (Z2) and above (Z3)**. The results of all active samples are summarized in Table 4.1 and literature data from measurements at several locations are selected and shown in the table. Even though those data represent mostly an average concentration over a longer measurement interval a general comparison can be drawn.

Table 4.1.: Number concentration of IN active above defined temperature limits (-20°C, -24°C and -30°C) from UA3-Imp0, UA4-Imp0,Imp2,Imp3 and UA5-ImpO compared with selected literature data.

Location	IN_{-20} [L^{-1}]	IN_{-24} [L^{-1}]	IN_{-30} [L^{-1}]
Marine environment	10^{-2} [143], 10^{-2}-10^{-1} [144]	10^{-1} [143, 144]	2.3 10^0 [143], 10^0-10^1 [144]
Rainforest, Brazil	10^0 [101]	3 10^0 [101]	10^1 [101]
Boreal forest, Finnland	3 10^{-1} [145]	5 10^0 [145]	1.1 10^1 [145]
Alps, Switzerland	10^{-3} [146]	10^{-2} [146]	3.0 10^0 - 1.8 10^2 [147]
Himalaya, India	10^{-2}-10^{-1} [148]	10^{-1}-10^{-0} [148]	10^0 [148]
Beijing, China	7.0 10^1 [149], 10^0 [150]	2.3 10^2 [149], 10^1 [150]	4.3 10^2 [149]
This study, UA3-Imp0b	1.8 10^1	2.6 10^1	9.4 10^1
This study, UA4-Imp0	2.6 10^1	2.2 10^3	1.6 10^4
This study, UA4-Imp2	1.5 10^1	8.4 10^1	3.6 10^2
This study, UA4-Imp3	< LOD	7.8 10^1	1.1 10^3
This study, UA5-Imp0	2.0 10^1	7.5 10^2	1.1 10^3
This study, average	2.0 10^1	6.3 10^2	3.7 10^3

Generally, in marine environment the number concentration is around 10^{-2} L^{-1} for IN_{-20}, 10^{-1} L^{-1} for IN_{-24} and 10^0 for IN_{-30} while near vegetation and above the canopy of trees (boreal and rainforest) the concentration increases by 1-2 orders of magnitude as seen for the amazon rainforest in Brazil or the boreal forest in Finland (see Table 4.1). On summits of mountains that reach the free troposphere (e.g., Jungerfernjoch in the Alps of Switzerland) the number concentration is generally lower than in the PBL, even though plumes from sea and land surface can increase the number of IN measured at high altitude stations [146, 147]. At other high elevated areas (e.g., in the Himalaya) the IN concentration is effected by surrounding environmental emissions [148], while in polluted cities, like Beijing, the number of IN is mostly high, reaching from 10^0 L^{-1} for -20°C to almost 10^3 L^{-1} for -30°C [149, 150]. Our results, measured in the environment of alpine vegetation (elevation around 1150 m) show a sharp increase at -20°C. Above that temperature the measured

values for active samples (UA3-Imp0b, UA4-Imp0,Imp2,Imp3 and UA5-Imp0) are significant higher than many literature data. This leads to the conclusion that the IN were sampled directly from emission events of plants, fungi and/or microbes and a direct observation of an emission plume after rainfall was achieved. Bursts of biogenic IN during and after rainfall have been reported previously in literature [110, 135]. Possible mechanisms causing such emissions are described by the impact of rain droplets on surfaces hosting biogenic cells or molecules [52] or by increased fungal spores ejection at high relative humidity [110, 125, 151]. Results of filtration and heat treatment experiments of the most active sample can further contribute to the interpretation of the IN burst recorded during this campaign.

4.3.2. Filtration and Heat Treatment

Filtration experiments of UA4-Imp0 revealed that about half of the IN_{-24} (51%) were smaller than 0.1 µm as seen in Figure 4.7. Furthermore, 5% passed a molecular filter at 300 kDa. However, the largest amount remained upon filtration, indicating that one majority had a size between 100 nm and ~9 nm (300 kDa for a spherical body) and another majority was above 100 nm. The 100 kDa filter finally cuts off the macromolecular IN and reveals a spectrum similar to the blank concentration as result (< 1% remains in the solution). The heat treatment of UA4-Imp0 indicates that the higher number of IN_{-24} (> 97%) was heat sensitive, which highlights the biological origin (heat denaturation of biological molecules). However, an increase in the curve is seen at around -24°C, pointing out the presence of heat stable IN in low concentrations within the sample mix (e.g. mineral dust).

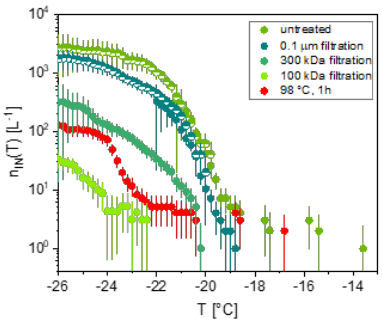

Figure 4.7.: Filtration and heat experiments of UA4-Imp0 measured with the TINA setup. Several number concentrations of IN are shown in colored dots plotted against the temperature. Figure adapted from Seifried et al., 2021 [123].

The characterization experiments reveal the IN sampled in UA4-Imp0 to be partly above and partly below 100 nm in size (including macromolecular material) and to be highly heat unstable. Many studies reported biogenic IN to be in the macromolecular size range [39, 57, 60, 67]. IN from silver birch (*Betula pendula*, as present at the sampling location), nucleate ice at similar temperatures (~ -20°C) [57]. Such IN can be extracted during rain fall and splashed off from the vegetation into the environment [123]. Moreover, airborne fungal spores [152], bacteria and mineral material have been reported to nucleate ice between -20°C and -25°C [153]. A further interpretation can be made after discussing microscopic images of CI samples.

4.4. Aerosol Particle Analysis

4.4.1. Fluorescent Particles

In Figure 4.8, selected images recorded with the fluorescence microscope are depicted. All other recorded pictures are attached in Appendix C. In general, during the first sampling period (e.g., UA1-CI3-D), the fraction of particles on stage D (cutoff 0.25 µm) was covering the substrate dense (Figure 4.8, A). This matter was below 1 µm in size and partly formed agglomerates on the surface of the aluminum foil. The concentration, observed optically, was equal for all sampling zones during UA1 and UA2. Similar fluorescence particles were found on ground-based samples in high concentrations after rainfall (UA4-CI0-D (seen in Figure 4.8, C and E) and UA5-CI0-D), while the concentration was lower during the rainfall event (UA3-CI0-D). Fluorescence particles in the accumulation-mode can consist of SOA [154] or organic material attached to dust particles [91]. Secondary organic matter formed out of vapor (e.g., isoprene or terpene) can also originate from higher tropospheric layers and get vertically transported to the PBL, e.g., during rainfall events [112]. Thus, no clear source appointment of accumulation-mode aerosol particles can be taken into consideration with the fluorescence data recorded during this study.

For the coarse-mode samples of UA1 and UA2 (Stage A, cutoff 2.5 µm), a few fluorescent particles were found occasionally on some spots of the substrate. In Figure 4.8, B one of those auto-fluorescent particles is shown, which is shaped like a pollen grain [155], e.g., pollen of *Betula pendula*. However, such observations during the spring sampling period remained the exception. On the other stages (B: cutoff 1 µm and C: cutoff 0.5 µm) almost no fluorescence particles were found for UA1 and UA2. During rainfall, the number concentration for coarse-mode was observable low, however a few large fluorescent particles (> 100 µm) were found on the impactor foils (see Appendix C, Figure C.2), highlighting the presence of plant debris or soil particles [51] possibly emitted during the impact of rain droplets on vegetation or soil. After rainfall events (UA4 and UA5) the aerosol concentration increased (as seen in Section 4.2) and a dense ensemble of fluorescence particles was observed for example on UA4-CI0-A (Figure 4.8, D and E). These particles are shaped in defined geometry (roundish and oval) and clearly indicate the cellular morphology of microorganisms. Such fluorescence cells could originate e.g., from fungi or bacteria (possible fluorophores: Calcium dipicolinate (CaDPA), nicotinamide adenine dinucleotide (NAD(P)H), neopertin and riboflavin [129, 156]). Furthermore, the fluorescence intensity is often higher at the cell wall, indicating the wall to be the main compartment of fluorophores [129, 155, 157]. Spores of both are known to increase in number concentration after rainfall events [124, 137]. Since the sample of Z0 from UA4 had the highest number concentration of IN further SEM images of the impactor foils were recorded to increase the resolution and identify aerosol particles based on their morphology.

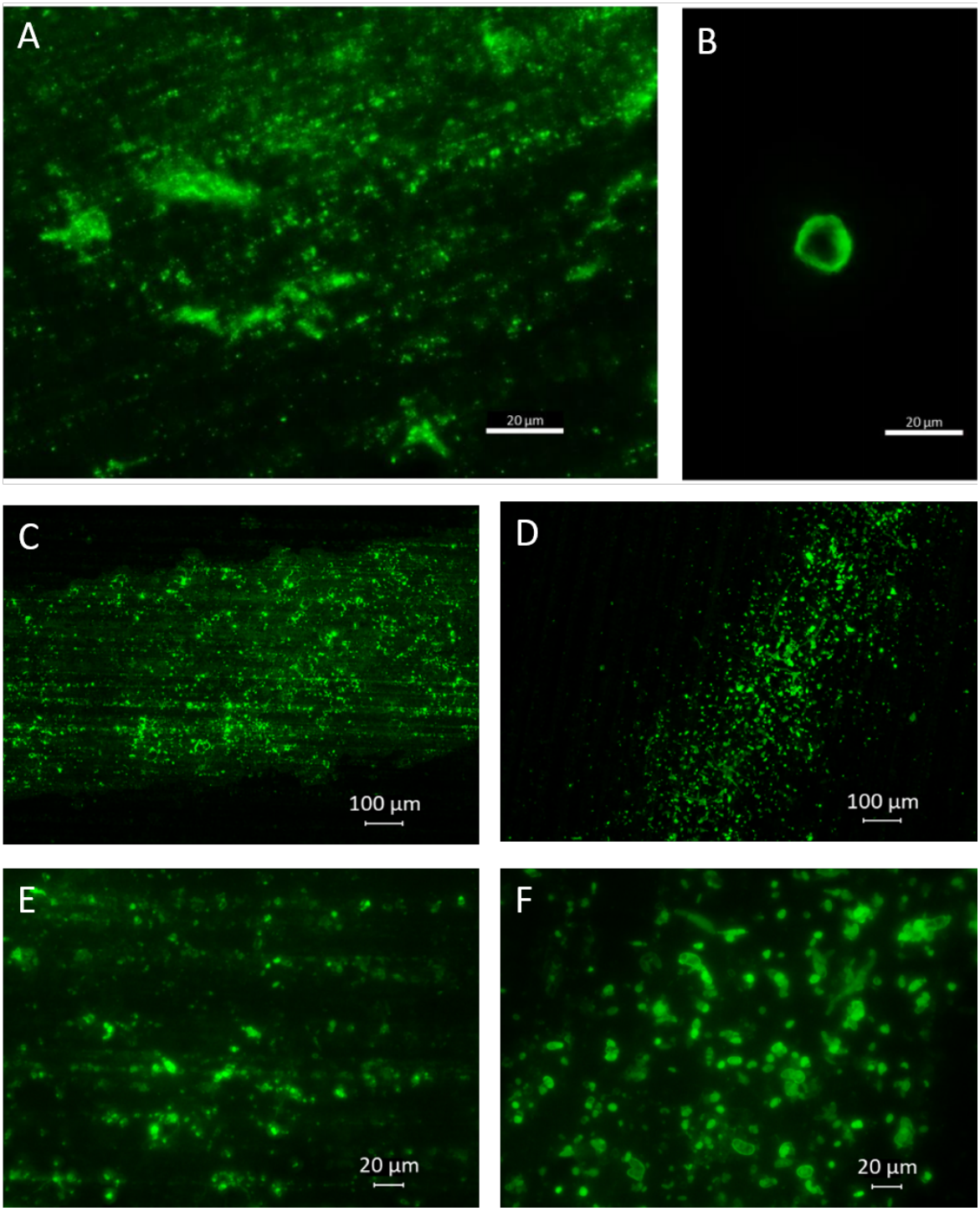

Figure 4.8.: Fluorescence microscopy of selected samples: A) First day, zone 3, stage D (UA1 CI3 D) x40; B) First day, zone 3, stage A (UA1 CI3 A) x40; C) Fourth day, zone 0, stage D (UA4 CI0 D) x10; D) Fourth day, zone 0, stage A (UA4 CI0 A) x10; E) Fourth day, zone 0, stage D, (UA4 CI0 D) x40; F) Forth day, zone 0, stage A, (UA4 CI0 A) x40.

4.4.2. Morphological Observations

The SEM images of stage D from UA4-CI0 are shown in Figure 4.9, where an overall view is given in the fist picture while two enlarged pictures offer a detailed view on the sampled ultra fine aerosol. It can be seen that the distribution is heterogeneously i.e., large particles (with a diameter around 1 µm) are observed on the microscopic image next to ultrafine aerosol (< 0.5 µm). Since stage D of the CI has a cutoff at 0.25 µm (aerodynamic diameter), those particles are far out of the range for the impaction stage and should have been collected at the previous stages. This could either be a result of deviations in the geometry (aerodynamic diameter does not match the optical observed diameter) or as a product of agglomeration processes on the aluminum foil during the sampling procedure. However, in the image with the highest magnification, the resolution is high enough to observe the true size of the sampled aerosol. That image was further proceeded in the analysis of the particle size distribution in Section 4.4.3.

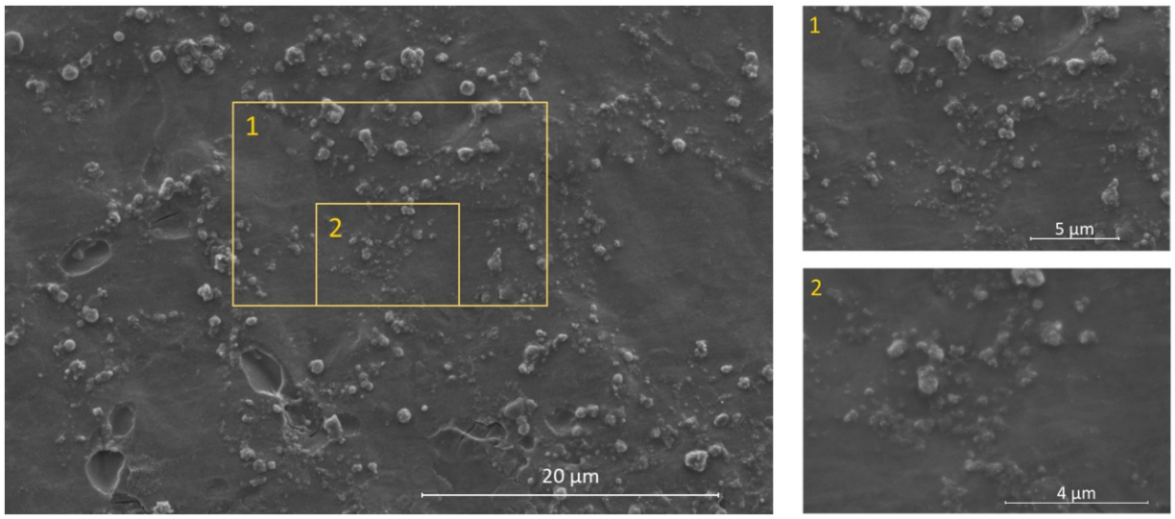

Figure 4.9.: SEM image from impactor stage D in 3 different magnifications from the 4th sampling day (UA4-PAC0-D). Figure adapted from Seifried et al., 2021 [123].

For the coarse-mode (UA4-CI0-A) the resolution was high enough to clearly distinguish between several morphologies. In Figure 4.10, A, an overview of the sample is depicted, where single cells can be observed as already seen for the fluorescence image (Section 4.4.1). With the power of electron microscopy, the morphology of the cellular-surfaces gets resolved. For example in Figure 4.10, B, two oval ornamented fungal spores can be clearly assigned, both of which grew parts of their hyphen after deposition on the aluminum foil. Figure 4.10, C shows a representative image of the general main composition of the aerosol including longitudinal and oval particles with smooth surfaces as reported in literature for several basidospores [158–160]. As highlights, an agglomerate of bacterial cells and a mineral dust particle were observed in Figure 4.10, D, a sporangia (i.e., a growth capsule of fungal spores) was seen in E and a perfectly spherical ornamented fungal spore in F (according to

comparisons with SEM images from other studies [160–164]). To get an overview of the size, a normal distribution analysis was performed (Section 4.4.3), while SPA revealed the main components of the sample regarding their shape (Section 4.4.4).

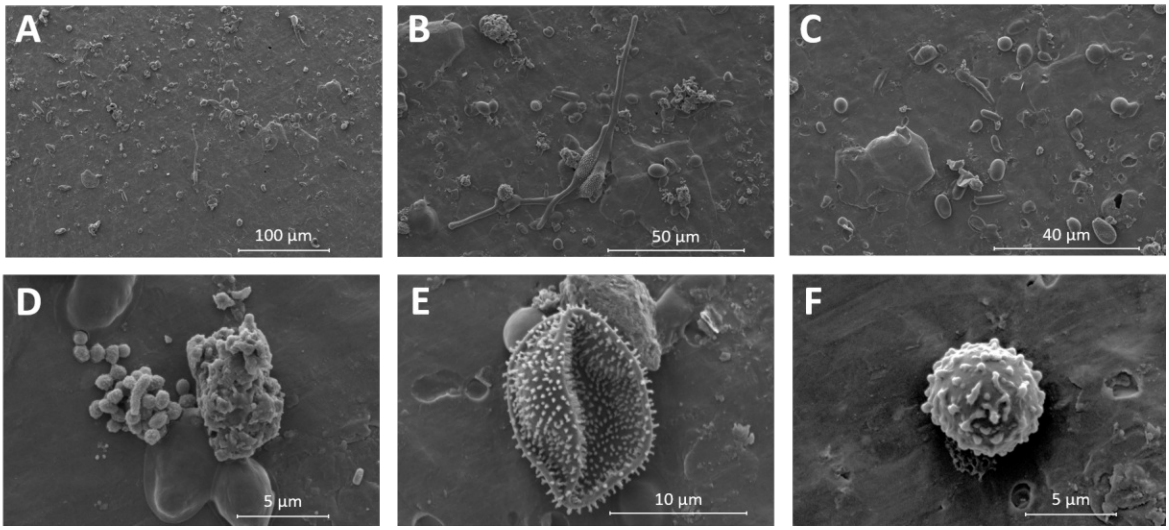

Figure 4.10.: SEM images from impactor stage A, 4th sampling day (UA4-CI0-A). Several pictures with different scales are shown from A) to F). Figures partly adapted from Seifried et al., 2021, [123].

4.4.3. Normal Distribution of Aerosol Particles

Overall 550 fluorescent particles and 654 particles from SEM images were counted for stage A and 181 particles for stage D. In Figure 4.11, A and B, the histograms of counted particles for stage D and for stage A are shown, whereat the mean particle diameter (i.e., surface diameter) is between 0.1 and 0.2 µm for the particles on stage D and between 3 and 4 µm for stage A. The percentage of coarse-mode particles with auto-florescent characteristics was 84%. The number concentration of the ultra-fine fraction from stage D (accumulation-mode) is three orders of magnitude higher than the coarse-mode fraction on stage A (Figure 4.11, C). The fitted logNormal distribution tends to expand to a higher logarithmic interval of diameters relative to stage A. Moreover the fluorescence curve (green line in Figure 4.11, C) is slightly shifted to higher diameters compared to the fitted function determined using SEM images (black line in Figure 4.11, C). This effect can be explained by taking into account that using fluorescence images to determine the diameters leads to an overestimation since the boarders of particles become blurred when fluorescence light is high. In Table 4.2 the concentrations which were achieved by integration of the fitted function are compared with literature data.

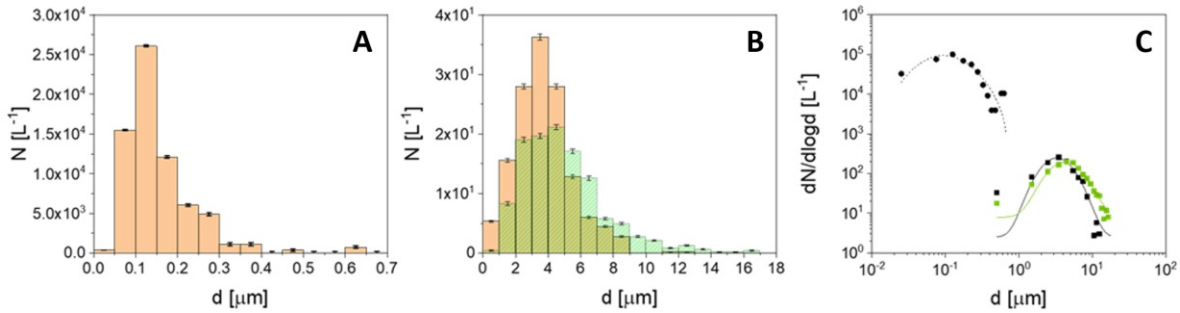

Figure 4.11.: Normal distribution of counted particles from sampling day 4 (UA4). A) Number of counted particles from SEM image of stage D in 0.05 µm diameter bins. B) Number of counted particles from SEM and fluorescence images in 1 µm diameter bins. C) Calculated dN/dlogd for stage A and stage D inclusive logNormal distribution fits. Figure adapted from Seifried et al., 2021 [123].

Table 4.2.: Number concentration of aerosols observed during this study (UA4-CI0) compared with literature data.

Location	$\mathbf{n_{coarse\ mode}}$ **[L^{-1}]**	$\mathbf{n_{accumulation\text{-}mode}}$ **[L^{-1}]**
Marine environment	10^3 [165]	7.0 10^4 [165]
Amazon Rainforest, Brazil	3 10^2 [109]	1 10^5 [109]
Boreal Forest, Hyytiälä, Finnland	1.2 10^3 [166]	3.3 10^5 [167], 8.3 10^5 [166]
Alps, Switzerland	5.2 10^1 [168]	1.1 10^5 [168]
Himalaya, Nepal	10^3-10^4 [169]	10^7 [170], 10^6 [169]
Beijing, China	7 10^3 [171]	7.8 10^6 [171]
This study, UA4-CI0	1.2 10^2	6.0 10^4

The measured values point out that the concentration of aerosol particles was lower than most results selected from literature. Generally, in polluted cities (for example in Beijing, China) the aerosol concentration is higher due to the emission of anthropocentric pollutants [171]. However, urban aerosol-pollutants do not influence the concentration of IN significantly [150]. In some mountainous regions, for example in the Himalaya, the number concentration of both, coarse and accumulation-mode, is highly effected by dust plums of the surrendered deserts [169]. The sampling location which was chosen in this study was not effected by pollutant-aerosol or dust plumes. Compared to an observation station in Switzerland, which is rather similar to the Austrian Alps, the coarse-mode section is slightly higher where the accumulation-mode number concentration is about half of the measured values [168]. In the vicinity of a boreal forest, the accumulation-mode and the coarse-mode tends to be one order of magnitude higher than the measurements [167], indicating that a dense vegetation increases the aerosol concentration (i.e., emission of primary biogenic aerosols). The results measured during this field campaign after rainfall (UA4-CI0) can be

interpreted a mixture of an alpine (free troposphere) and a forest environment for the aerosol number concentration. Considering this as just one measuring point and furthermore, taking into account that the CI might have a weak sampling efficiency for ultra-fine particles and the method of counting the particles on a SEM image to have a rather high error interval, the observed concentration has to be taken with caution.

4.4.4. Single Particle Analysis and Linkages to Biogenic Ice Nuclei

To gain qualitative information on the aerosol composition which was sampled during the second day of the field campaign (UA4-CI0) a SPA of the sampled coarse-mode aerosol was performed as explained in Section 3.4.5. The observed particles, which are shown in Figure 4.12, A, were counted and assigned to clusters of non-fluorescence and fluorescence particles. Fluorescence particles were divided further into clusters of different shapes (i.e., globe, ornamented, elongate, cylindric and undefined shape) [72]. The shape categories are shown in Figure 4.12, B, whereas the results of SPA are plotted as a bar graph in Figure 4.12, C.

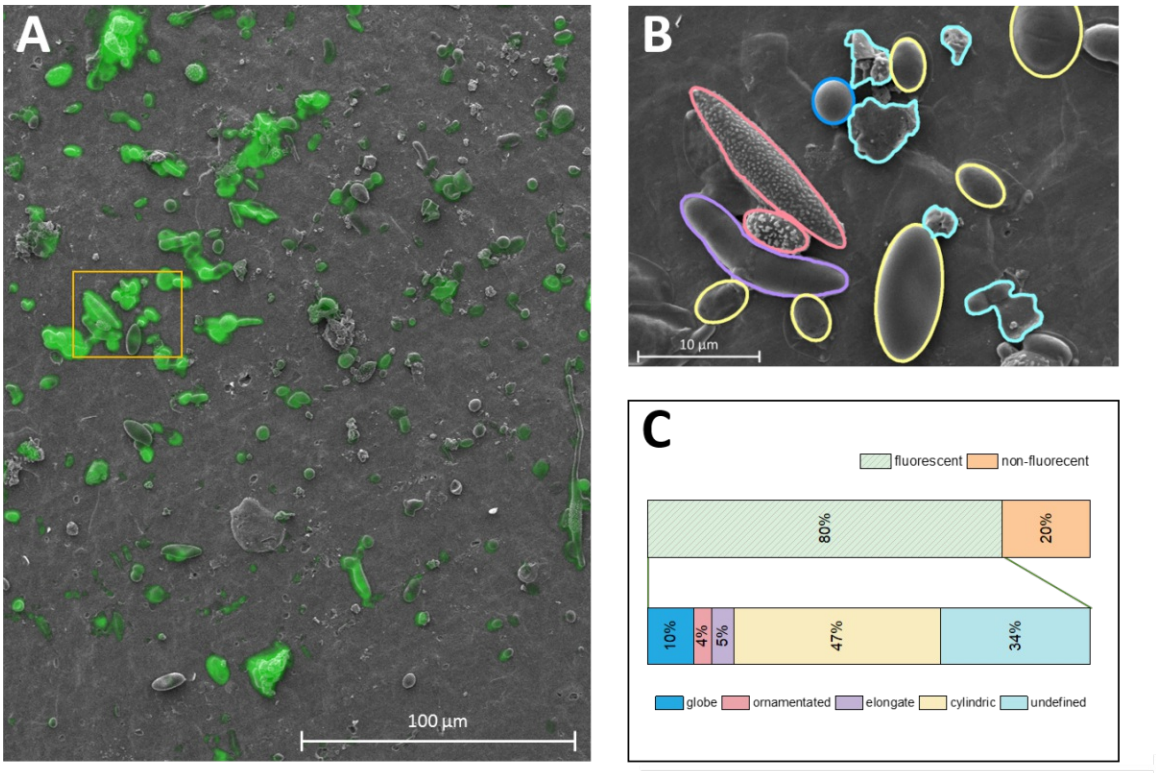

Figure 4.12.: Single particle analysis (SPA) of combined SEM and fluoresce observations. A) SEM image with overlapped corresponding fluorescence image. B) SEM image of different categories of particle shapes. C) Results of SPA as bar graph. Figure adapted from Seifried et al., 2021 [123].

In the SPA (Figure 4.12), **80% of the sampled particles showed auto-fluorescence characteristics**. Considering the shape of analyzed particles, **almost half of the fluorescence particles (47%) had a cylindrical shape**, whereat the minority was shaped elongated, global or ornamented (5%, 10% and 4%). Another majority (34%) had shapes, that could not been clustered in rational groups. Moreover, some particles (see Figure 4.12, B) had a fluorescence coating which is considered from organic consistence in literature [172]. Since it was not always clear on the recorded image, if particles were coated or not, no distinction has been made between non-coated and coated fluorescence particles.

Fungal spores can contribute to every analyzed shape according to their huge variance in morphology. Fungi of the genera basidomycota are known to form spores with cylindrical shapes as seen in the observed images [158–160]. For example *Agaricus bisporus*, *Amanita muscaria*, *Boletus zelleri* are three species of the class of Agaricomycetes that form cylindrical spores and furthermore, nucleate ice at heterogeneous temperatures [173]. Regarding the measured freezing temperature of the samples in Section 4.3.1, the fungus *Endocronartium harknessii* was reported to nucleate ice at rather similar temperatures (-21.4°C) [75]. This fungus forms elliptical spores and infects European pine species (e.g., *Pinus sylvestris, P. halepensis, P. nigra*) and alpine pines (i.e., *Pinus mugo*) such as present at the sampling location. Chang and Blenis, 1988, suggest that the spores have a relatively good ability to survive in an airborne state and furthermore, have the potential to be transported long distances [174]. Such spores would have an atmospheric impact on cloud glaciation in the free troposphere. Also bacteria are known to form spores of roundish or cylindrical shape as observed in the samples [175]. However, most ice nucleation active bacteria trigger freezing at much warmer temperatures [76]. An organic coating on aerosol particles is described in literature by Huffman et al., 2012 during a sampling campaign for fungal spores in the amazonas rainforest [172]. They report the coating to be likely from secondary origin, however with undefined source (either co-ejected during wet bioaerosol discharge or condensation of secondary organic material from vapor) [172]. We suggest, that an extraction of macromolecular IN from birch [123] or pine could lead to the organic coating on fungal and/or bacterial spores and other undefined aerosol particles. This coating, which was observed in the SEM images of this study, could stack to aerosol particles when getting airborne. Such particles would be shuttles for nano-IN during wet bioaerosol generation [52] and have an intense impact on atmospheric cloud glaciation, i.e., on the Earth's climate.

5. Conclusions and Outlook

To conclude the findings of this thesis, five bullet points can be summarized:

1. DAPSI is a flexible system usable to sample aerosol particles in the vicinity of emission sources, which cannot be reached directly by airplanes or from ground measurement stations. The sampling efficiency for the self-built impinging system is above 80% for airborne IN and around 90% for PSL.

2. IN were detected at a remote sampling location suited in the Austrian Alps, below and above the canopy of vegetation and up to 45 m of altitude. After rainfall, the freezing temperature (T_{50}) is similar to extracts from birches analyzed in previous studies [70].

3. Fluorescent coarse-mode particles of biogenic origin (e.g., fungal spores, bacteria, etc.) where emitted as plumes during rainy days with high humidity while the concentration of fluorescent accumulation-mode particles was relatively stable during the whole sampling campaign. Some particles appeared to be coated with an organic film.

4. Compared to literature the concentration of IN (active above -24°C) was high after rainfall when humidity increased (up to 2.2 10^3 L^{-1}) while the concentration of sampled aerosol particles was comparable with literature data from alpine environment (1.2 10^2 L^{-1} for coarse-mode and 6.0 10^4 L^{-1} for accumulation-mode).

5. The sampled IN were rather heat sensible and had a majority size between 9 nm (300 kDa) and 100 nm.

I conclude that DAPSI is an efficient tool for tropospheric research on aerosol emissions. The weight is kept at the upper limit capable for small-scale UAVs, enabling to sample with two different methods (Imp and CI) and measure environmental parameters and PM concentrations. In combination with small rotary-wing drones, the operation during windy days is limited and the sampling time interval (10 min) is rather short. Especially, the CI-setup is difficult to control airborne in a safe way. Hence, it was not launched during the second half of the campaign. Short sampling intervals further limit the minimal concentration of aeorsols to be observed and thus, the minimal number concentration of IN to detect freezing in the laboratory. By using a freezing assay with µL droplets, the qualitative detection and quantitative evaluation of IN emissions is achieved. However, some samples showed the same freezing spectra as the blank, indicating the concentration of IN to be to low to get detected using DAPSI in combination with small UAVs. However, using

DAPSI with larger UAVs could enable a broad spectra of opportunities (longer flight times, higher range of possible altitudes, etc.). Moreover, Imp samples could provide a basis for microbiological characterization (e.g., cultivation of microbes, shotgun metagenomics, etc.) regarding bioaerosol research. Also the microscopic analysis of CI foils is expandable (e.g., Raman microscopy, fluorescence staining, etc.).

The results observed during the field campaign show a sharp increase of coarse-mode aerosol after rainfall in the Austrian Alps. These emissions are from biological origin as determined by microscopic observations (fluorescence microscopy and SEM). Characterization experiments of IN (heat treatment and size filtration) support the suggestion that the ice nucleation activity is linked to biogenic nano-IN. Such IN can be present as primary biological particle (e.g., fungal spores, bacteria, etc.) but also originate from organic coating observed on collected coarse mode particles. Biogenic ice nucleating macromocules (e.g, extracted from birch, pine, fungi, etc.) can contribute to the ice nucleation activity of the coating. Plumes of biogenic IN, directly linked to vegetation, can influence cloud glaciation in the free troposphere. However, it is difficult to quantify such phenomena since the chemical composition of IN, the seasonal and temporal abundance and the emission mechanisms largely remain unexplained. Further research has to be based on bioaerosol emissions to estimate the impact on Earth's climate. However, I strongly suggest that drastic changes in alpine vegetation due to climate change can further alter regional weather and climate. When expanding bioaerosol emission from frost resistant vegetation to a larger scale (e.g., boreal forest) one would also expect an influence on the global climate system.

Appendix

A. Circuit Diagram

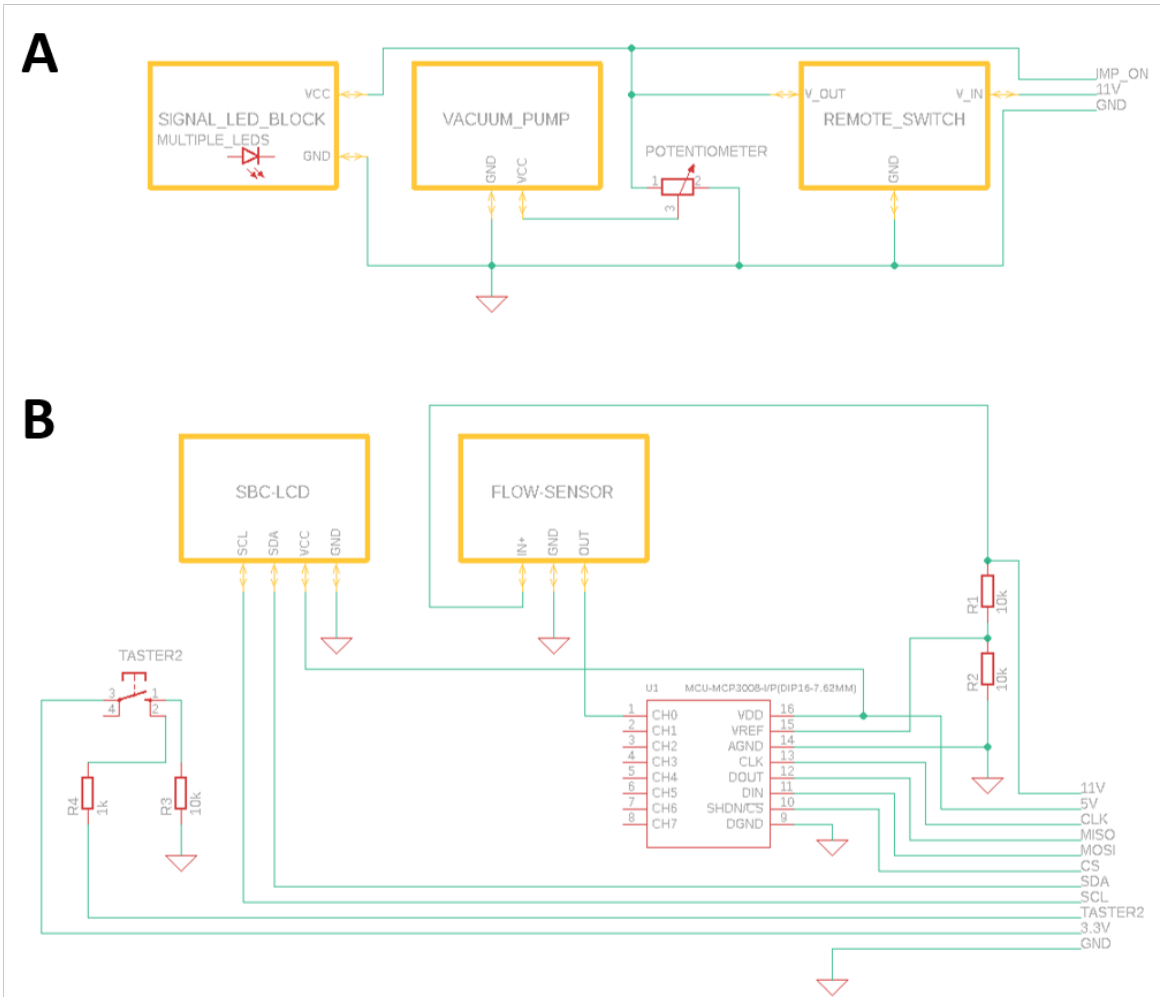

Figure A.1.: Circuit diagram for the vacuum pump in A and for the flowmeter in B.

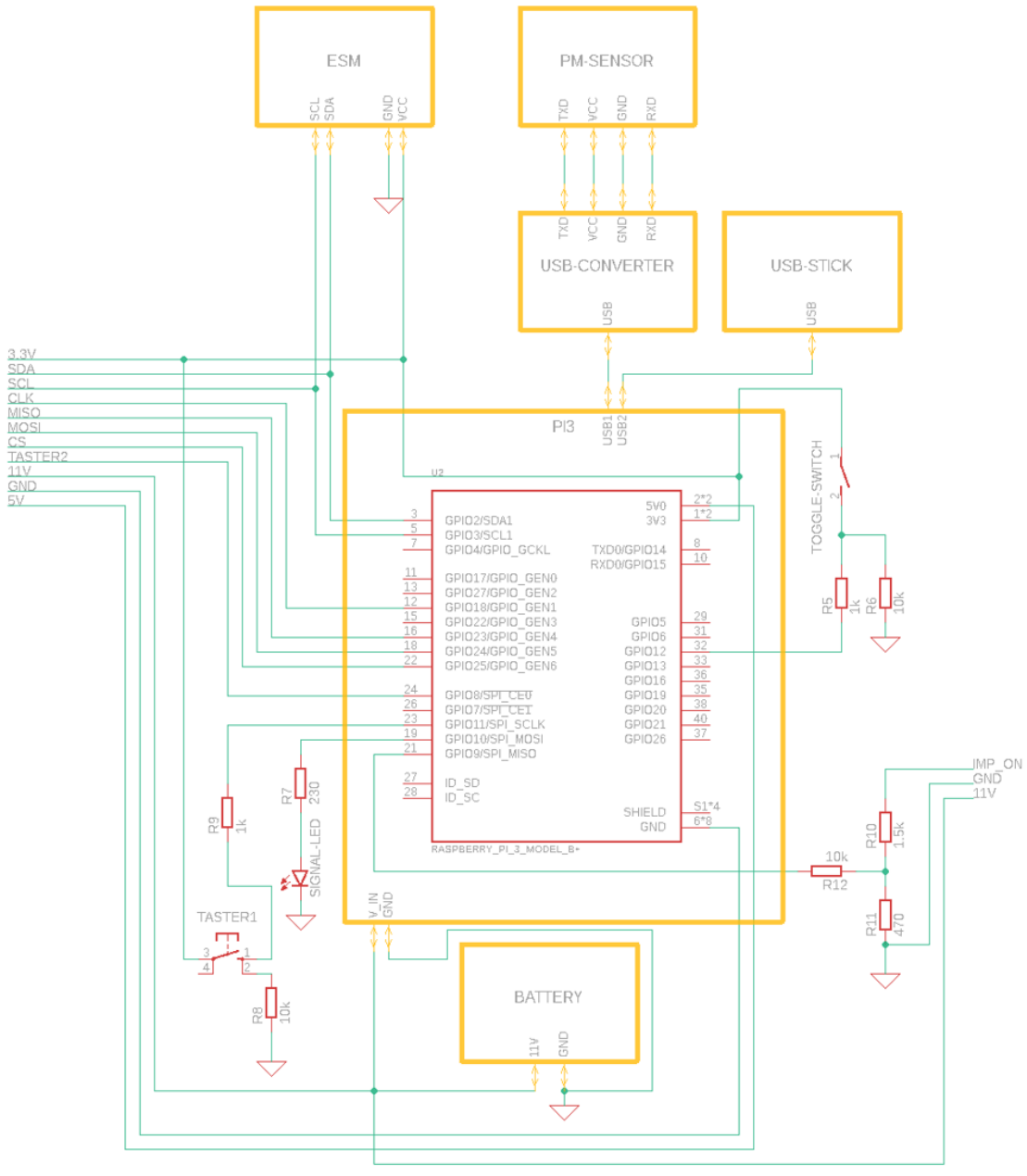

Figure A.2.: Circuit diagram for the Raspberry Pi.

B. Software

```
#Paul Bieber/ drone measurements/ temperature, pressure, realative humidity and gas resistance with BME680 sensor / Flowmeter inclusive LCD-display
#script of sensor calibration and data evaluation according to examples/read-all file
#script of PM sensor https://gist.github.com/kadamski/92653913a53baf9dd1a8
#script of LCD display according to https://tutorials-raspberrypi.de/hd44780-lcd-display-per-i2c-mit-dem-raspberry-pi-ansteuern/
#script of MCP3008 - I/P / analog to digital converter for flow measurements according to https://learn.adafruit.com/raspberry-pi-analog-to-digital-converters/mcp3008

from __future__ import print_function
import serial, struct, sys, time, json
import bme680
import time
import RPi.GPIO as GPIO

# Import SPI library (for hardware SPI) and MCP3008 library.
import Adafruit_GPIO.SPI as SPI
import Adafruit_MCP3008

# Import lcddriver
import lcddriver

#init for controll modules
GPIO.setmode(GPIO.BCM)
ImpON = (0)
LED = (1)
taster = (2)
taster2 = (3)
toggle_switch = (4)
signal = [9,10,11,8,12]
GPIO.setup(signal[ImpON], GPIO.IN)
GPIO.setup(signal[taster], GPIO.IN)
GPIO.setup(signal[taster2], GPIO.IN)
GPIO.setup(signal[toggle_switch], GPIO.IN)
GPIO.setup(signal[LED], GPIO.OUT, initial = False)

# Software SPI configuration
CLK  = 18
MISO = 23
MOSI = 24
```

```
CS   = 25
mcp = Adafruit_MCP3008.MCP3008(clk=CLK, cs=CS, miso=MISO, mosi=MOSI)

#init for PM sensor
DEBUG = 0
CMD_MODE = 2
CMD_QUERY_DATA = 4
CMD_DEVICE_ID = 5
CMD_SLEEP = 6
CMD_FIRMWARE = 7
CMD_WORKING_PERIOD = 8
MODE_ACTIVE = 0
MODE_QUERY = 1

ser = serial.Serial()
ser.port = "/dev/ttyUSB0"
ser.baudrate = 9600

ser.open()
ser.flushInput()

byte, data = 0, ""

def dump(d, prefix=''):
  print(prefix + ' '.join(x.encode('hex') for x in d))

def construct_command(cmd, data=[]):
  assert len(data) <= 12
  data += [0,]*(12-len(data))
  checksum = (sum(data)+cmd-2)%256
  ret = "\xaa\xb4" + chr(cmd)
  ret += ''.join(chr(x) for x in data)
  ret += "\xff\xff" + chr(checksum) + "\xab"

  if DEBUG:
  dump(ret, '> ')
  return ret

def process_data(d):
  r = struct.unpack('<HHxxBB', d[2:])
  pm25 = r[0]/10.0
  pm10 = r[1]/10.0
  checksum = sum(ord(v) for v in d[2:8])%256
  return [pm25, pm10]

def process_version(d):
  r = struct.unpack('<BBBHBB', d[3:])
  checksum = sum(ord(v) for v in d[2:8])%256
  print("Y: {}, M: {}, D: {}, ID: {}, CRC={}".format(r[0], r[1], r[2], hex(r
    [3]), "OK" if (checksum==r[4] and r[5]==0xab) else "NOK"))
```

```
87
88  def read_response():
89    byte = 0
90    while byte != "\xaa":
91      byte = ser.read(size=1)
92
93    d = ser.read(size=9)
94
95    if DEBUG:
96      dump(d, '< ')
97    return byte + d
98
99  def cmd_set_mode(mode=MODE_QUERY):
100   ser.write(construct_command(CMD_MODE, [0x1, mode]))
101   read_response()
102
103 def cmd_query_data():
104   ser.write(construct_command(CMD_QUERY_DATA))
105   d = read_response()
106   values = []
107   if d[1] == "\xc0":
108     values = process_data(d)
109   return values
110
111 def cmd_set_sleep(sleep=1):
112   mode = 0 if sleep else 1
113   ser.write(construct_command(CMD_SLEEP, [0x1, mode]))
114   read_response()
115
116 def cmd_set_working_period(period):
117   ser.write(construct_command(CMD_WORKING_PERIOD, [0x1, period]))
118   read_response()
119
120 def cmd_firmware_ver():
121   ser.write(construct_command(CMD_FIRMWARE))
122   d = read_response()
123   process_version(d)
124
125 def cmd_set_id(id):
126   id_h = (id>>8) % 256
127   id_l = id % 256
128   ser.write(construct_command(CMD_DEVICE_ID, [0]*10+[id_l, id_h]))
129   read_response()
130
131
132 print("""Display Temperature, Pressure, Humidity and Gas
133
134 Press Ctrl+C to exit
135
136 """)
```

```
137
138 #init for temperature sensor
139 try:
140   sensor = bme680.BME680(bme680.I2C_ADDR_PRIMARY)
141 except IOError:
142   sensor = bme680.BME680(bme680.I2C_ADDR_SECONDARY)
143
144 # These calibration data can safely be commented
145 # out, if desired.
146
147 print('Calibration data:')
148 for name in dir(sensor.calibration_data):
149
150 if not name.startswith('_'):
151   value = getattr(sensor.calibration_data, name)
152
153   if isinstance(value, int):
154     print('{}: {}'.format(name, value))
155
156 # These oversampling settings can be tweaked to
157 # change the balance between accuracy and noise in
158 # the data.
159
160 sensor.set_humidity_oversample(bme680.OS_2X)
161 sensor.set_pressure_oversample(bme680.OS_4X)
162 sensor.set_temperature_oversample(bme680.OS_8X)
163 sensor.set_filter(bme680.FILTER_SIZE_3)
164 sensor.set_gas_status(bme680.ENABLE_GAS_MEAS)
165
166 print('\n\nInitial reading:')
167 for name in dir(sensor.data):
168   value = getattr(sensor.data, name)
169
170   if not name.startswith('_'):
171     print('{}: {}'.format(name, value))
172
173 sensor.set_gas_heater_temperature(320)
174 sensor.set_gas_heater_duration(150)
175 sensor.select_gas_heater_profile(0)
176
177 # Up to 10 heater profiles can be configured, each
178 # with their own temperature and duration.
179 # sensor.set_gas_heater_profile(200, 150, nb_profile=1)
180 # sensor.select_gas_heater_profile(1)
181
182 print('\n\nPolling:')
183
184 measurement = False
185
186 #LED signal to say READY
```

```
187
188 GPIO.output(signal[LED], True)
189 time.sleep(0.25)
190 GPIO.output(signal[LED], False)
191 time.sleep(0.25)
192 GPIO.output(signal[LED], True)
193 time.sleep(0.25)
194 GPIO.output(signal[LED], False)
195 time.sleep(0.25)
196 GPIO.output(signal[LED], True)
197 time.sleep(0.25)
198 GPIO.output(signal[LED], False)
199 time.sleep(0.25)
200
201 try:
202
203 #main program code
204
205   while True:
206
207 #taster to start the measurement has to be pressed here
208
209     if GPIO.input(signal[taster]) == True and measurement == False:
210       time.sleep(0.5)
211       measurement = True
212       fb = open('/media/pi/INTENSO/field-measurements/Measurements.txt','a+')
213       a = str('measurement starts')
214       fb.write(a)
215       fb.write('\n')
216       a = str('impinger status (ON/OFF), PM2.5 (ug/m3), PM10(ug/m3),
    temperature (C), pressure (hPa), relative humidity (%), gas resistance (
    ohm)')
217       fb.write(a)
218       fb.write('\n')
219       fb.close()
220       print ('measurement starts')
221       print ('impinger status (ON/OFF), PM2.5 (ug/m3), PM10(ug/m3),
    temperature (C), pressure (hPa), relative humidity (%), gas resistance (
    ohm)')
222       time.sleep(0.5)
223
224 #measurement runs after the taster has been pressed once
225
226     while (measurement == True):
227
228 #starting the PM-sensor
229
230       cmd_set_sleep(0)
231       cmd_set_mode(1);
232
```

```
      if sensor.get_sensor_data():
        output = '{0:.2f} ,{1:.2f} ,{2:.2f} '.format(
          sensor.data.temperature,
          sensor.data.pressure,
          sensor.data.humidity)

        if sensor.data.heat_stable:

#ImpON is the 12V signal which is active when the Impinger is active
#ON and OFF signal is printed to the data according to the signal
#getting values from the PM-sensor

          values = cmd_query_data();

          if GPIO.input(signal[ImpON]) == True and values is not None:

            print('ON,', values [0], values [1], '{0},{1} '.format(
              output,
              sensor.data.gas_resistance))
            fb = open('/media/pi/INTENSO/field-measurements/Measurements.txt',
    'a+')
            a = str ('ON, ')
            fb.write(a)
            a = str(values [0])
            fb.write(a)
            a = str(', ')
            fb.write(a)
            a = str(values [1])
            fb.write(a)
            a = str(', ')
            fb.write(a)
            a = str('{0},{1} '.format(
              output,
              sensor.data.gas_resistance))
            fb.write(a)
            fb.write('\n')
            fb.close()

          if GPIO.input(signal[ImpON]) == False and values is not None:

            print('OFF,', values [0], values [1], '{0},{1} '.format(
              output,
              sensor.data.gas_resistance))
            fb = open('/media/pi/INTENSO/field-measurements/Measurements.txt',
    'a+')
            a = str('OFF, ')
            fb.write(a)
            a = str(values [0])
            fb.write(a)
            a = str(', ')
```

```
            fb.write(a)
            a = str(values [1])
            fb.write(a)
            a = str(', ')
            fb.write(a)
            a = str('{0},{1} '.format(
              output,
              sensor.data.gas_resistance))
            fb.write(a)
            fb.write('\n')
            fb.close()

        else:
          print(output)

#according to status of the measurement, the LED is off (no measurement),
    blinking (measurement without impinger sampling) or on (measurement with
    impinger sampling)

      if GPIO.input(signal[ImpON]) == True:

        GPIO.output(signal[LED], True)
        time.sleep(2)

      if GPIO.input(signal[ImpON]) == False:

        GPIO.output(signal[LED], True)
        time.sleep(0.5)
        GPIO.output(signal[LED], False)
        time.sleep(0.5)
        GPIO.output(signal[LED], True)
        time.sleep(0.5)
        GPIO.output(signal[LED], False)
        time.sleep(0.5)

#pressing the taster one more time ends the measurement

      if GPIO.input(signal[taster]) == True and measurement == True:
      time.sleep(0.5)
        fb = open('/media/pi/INTENSO/field-measurements/Measurements.txt','a+'
    )
        a = str('measurement ends')
        fb.write(a)
        fb.write('\n')
        print ('measurement ends')
        measurement = False
        time.sleep(0.5)

    while GPIO.input(signal[toggle_switch]) == True:
      mean_flow = [0]*10
```

```
328         for j in range(10):
329 # Read all the ADC channel values in a list.
330           values = [0]*8
331           for i in range(8):
332 # The read_adc function will get the value of the specified channel (0-7).
333             values[i] = mcp.read_adc(i)
334 # Print the ADC value for channel 2. values get substituted by 204.6 and
    devided through 81.8 to get l/min
335           flow0 = float('{0:>4}'.format(*values))
336           flow1 = float('{1:>4}'.format(*values))
337           flow2 = float('{2:>4}'.format(*values))
338           flow3 = float('{3:>4}'.format(*values))
339           flow4 = float('{4:>4}'.format(*values))
340           flow5 = float('{5:>4}'.format(*values))
341           flow6 = float('{6:>4}'.format(*values))
342           flow7 = float('{7:>4}'.format(*values))
343           mean_flow[j] = (flow0)
344           time.sleep(0.1)
345
346
347         mean_flow0 = float('{0:>4}'.format(*mean_flow))
348         mean_flow1 = float('{1:>4}'.format(*mean_flow))
349         mean_flow2 = float('{2:>4}'.format(*mean_flow))
350         mean_flow3 = float('{3:>4}'.format(*mean_flow))
351         mean_flow4 = float('{4:>4}'.format(*mean_flow))
352         mean_flow5 = float('{5:>4}'.format(*mean_flow))
353         mean_flow6 = float('{6:>4}'.format(*mean_flow))
354         mean_flow7 = float('{7:>4}'.format(*mean_flow))
355         mean_flow8 = float('{8:>4}'.format(*mean_flow))
356         mean_flow9 = float('{9:>4}'.format(*mean_flow))
357
358         mean_mean_flow = ((mean_flow0 + mean_flow1 + mean_flow2 + mean_flow3 +
    mean_flow4 + mean_flow5 + mean_flow6 + mean_flow7 + mean_flow8 +
    mean_flow9)/10)
359
360
361         flow_in_l_per_min = ((mean_mean_flow -204.6)/81.8)
362         print (flow_in_l_per_min)
363         flow_as_string = str(flow_in_l_per_min)
364         lcd = lcddriver.lcd()
365         lcd.lcd_clear()
366         lcd.lcd_display_string('air flow (l/min):',1)
367         lcd.lcd_display_string(flow_as_string,2)
368
369
370         if  GPIO.input(signal[taster2]) == False:
371           GPIO.output(signal[LED], False)
372
373         if  GPIO.input(signal[taster2]) == True:
374           GPIO.output(signal[LED], True)
```

```
375         fb = open('/media/pi/INTENSO/field-measurements/Measurements-flow.txt'
    ,'a+')
376         fb.write(flow_as_string)
377         fb.write('\n')
378         fb.close()
379 
380 except KeyboardInterrupt:
381   pass
```

C. Fluorescence Images

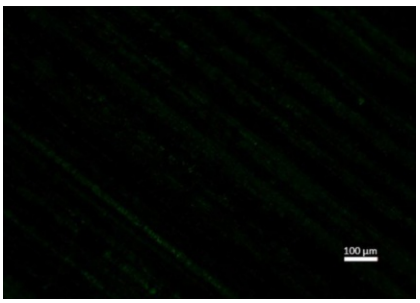

Figure C.1.: Background of an aluminum foil under the fluorescence microscope. Picture adapted from Bieber et al., 2020 [120]

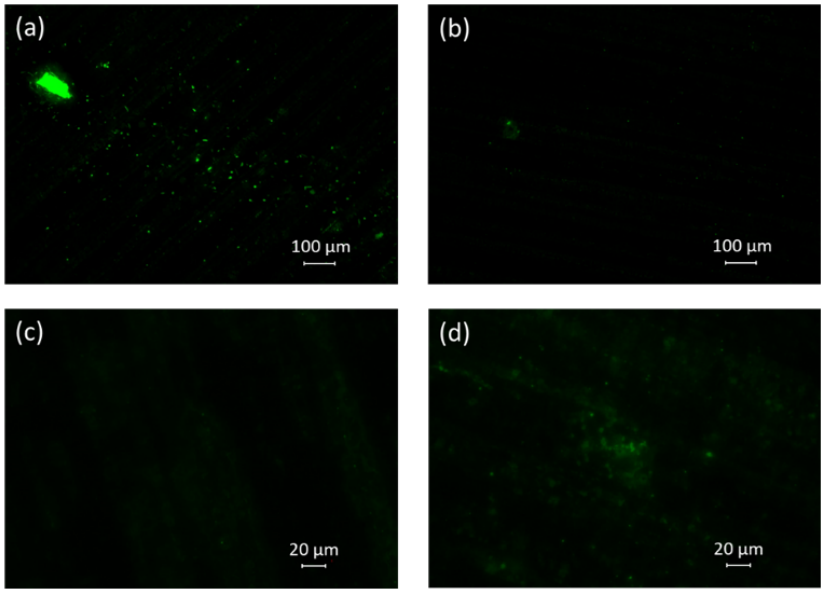

Figure C.2.: Fluorescence images of UA3. (a) stage A; (b) stage B, (c) stage C; (d) stage D. Adapted from Seifried et al., 2021 [123].

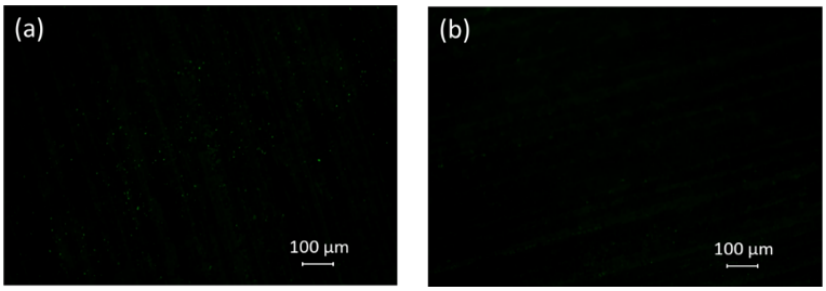

Figure C.3.: Fluorescence images of UA3. (a) stage B; (b) stage C. Adapted from Seifried et al., 2021 [123].

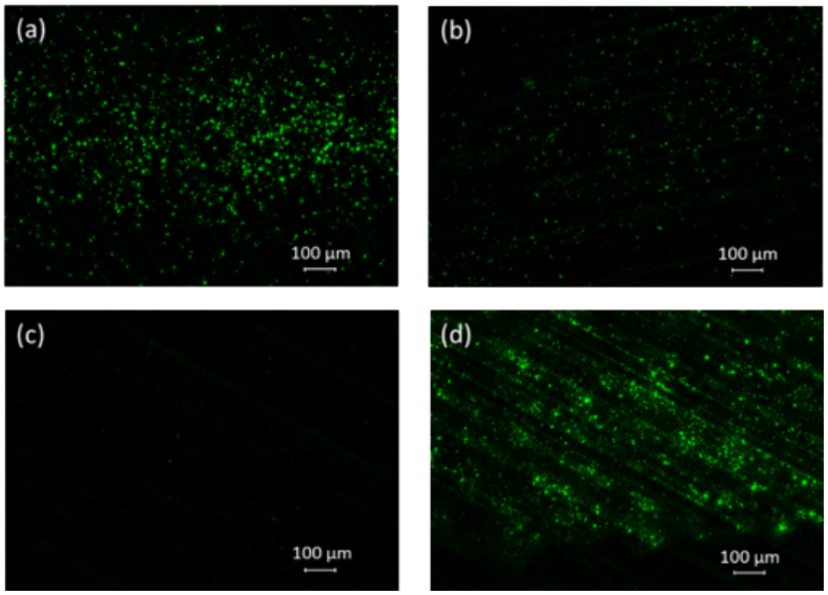

Figure C.4.: Fluorescence images of UA3. (a) stage A; (b) stage B, (c) stage C; (d) stage D. Adapted from Seifried et al., 2021 [123].

D. Single Particle Analysis

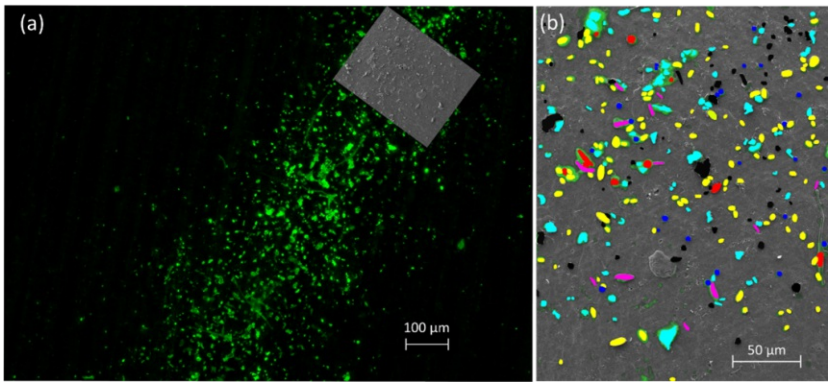

Figure D.1.: a) Single particles analysis with overlapping raw images, b) Resulting image and data evaluation. Figures adapted from Seifried et al., 2021 [123].

List of Abbreviations

AE	auger electrons
BPWW	birch pollen washing water
BSE	back scattered electrons
CaDPA	Calcium dipicolinate
CCN	cloud condensation nuclei
CI	cascade impactor
CUCI	controlling unit for the CI
CUImp	controlling unit for the Imp
Da	Dalton
DAPSI	Drone-based aerosol sampling impinger/impactor
EK	Eiskeim
ESM	electric sensor module
FMU	flow meter unit
I2C	inter-integrated circuit
Imp	impinger
IN	ice nuclei
IPCC	Intergovernmental Panel on Climate Change
LCD	liquid crystal display
LED	light-emitted diode
LOD	limit of detection
LOQ	limit of quantification
LR	long-wave radiation
MFT	mean freezing temperature
NAD(P)H	nicotinamide adenine dinucleotide
OPC	optical particle counter
PBL	planetary boundary layer
PE	primary electrons
PM	particulate matter
PSL	polystyrene latex
PVC	polyvinyl chloride
RS	remote switch
SD	standard deviation
SE	secondary electrons
SEM	Scanning Electron Microscopy
SOA	secondary organic aerosol
SPA	single particle analysis
SPP	sub-pollen-particles

SR	solar radiation
SU	sensor unit
TINA	twin-plate ice nucleation assay
UA	Upper Austria
UAVs	unoccupied aerial vehicles
USB	universal serial bus
VOC	volatile organic compounds
VODCA	Vienna optical droplet crystallization analyzer
X	X-rays
Z(0,1,2,3)	sampling zone (0,1,2,3)

List of Figures

List of Tables

Bibliography

[1] V. J. Schäfer. The production of ice crystals in a cloud of supercooled water droplets. *Science*, 104(2707):457–459, 1946.

[2] V. J. Schäfer. The formation of ice crystals in the laboratory and the atmosphere. *Chemical Reviews*, 44(2):291–320, 1949.

[3] B. Vonnegut. The nucleation of ice formation by silver iodide. *Journal of Applied Physics*, 18(7):593–595, 1947.

[4] R. M. Rauber, B. Geerts, L. Xue, J. French, K. Friedrich, R. M. Rasmussen, S. A. Tessendorf, D. R. Blestrud, M. L. Kunkel, and S. Parkinson. Wintertime orographic cloud seeding—a review. *Journal of Applied Meteorology and Climatology*, 58(10):2117–2140, 2019.

[5] N. H. Fletcher. Ice crystal nucleation by aerosol particles. *Discussions of the Faraday Society*, 30:39, 1960.

[6] N. H. Fletcher. Active sites and ice crystal nucleation. *Journal of the Atmospheric Sciences*, 26(6):1266–1271, 1969.

[7] R. C. Schnell and G. Vali. Atmospheric ice nuclei from decomposing vegetation. *Nature*, 236(5343):163–165, 1972.

[8] R. C. Schnell and G. Vali. World-wide source of leaf-derived freezing nuclei. *Nature*, 246(5430):212–213, 1973.

[9] L. R. Maki, E. L. Galyan, M. Chang-Chien, and D. R. Caldwell. Ice nucleation induced by pseudomonas syringae. *Applied microbiology*, 28(3):456–459, 1974.

[10] S. E. Lindow, D. C. Arny, and C. D. Upper. Bacterial ice nucleation: A factor in frost injury to plants. *Plant Physiology*, 70(4):1084–1089, 1982.

[11] S. P. Graether and Z. Jia. Modeling pseudomonas syringae ice-nucleation protein as beta-helical protein. *Biophysical Journal*, 80(3):1169–1173, 2001.

[12] B. J. Murray, D. O'Sullivan, J. D. Atkinson, and M. E. Webb. Ice nucleation by particles immersed in supercooled cloud droplets. *Chemical Society Reviews*, 41(19):6519, 2012.

[13] N. H. Fletcher. *The physics of rainclouds*. Cambridge University Press, 2011.

[14] W. A. Cooper. Ice initiation in natural clouds. In *Precipitation enhancement, A scientific challenge*, pages 29–32. Springer, 1986.

[15] M. P. Meyers, P. J. DeMott, and W. R. Cotton. New primary ice-nucleation parameterizations in an explicit cloud model. *Journal of Applied Meteorology*, 31(7):708–721, 1992.

[16] P. J. DeMott, A. J. Prenni, X. Liu, S. M. Kreidenweis, M. D. Petters, C. H. Twohy, M. S. Richardson, T. Eidhammer, and D. C. Rogers. Predicting global atmospheric ice nuclei distributions and their impacts on climate. *Proceedings of the National Academy of Sciences*, 107(25):11217–11222, 2010.

[17] J. S. Seinfeld, C. Bretherton, K. S. Carslaw, H. Coe, P. J. DeMott, E. J. Dunlea, G. Feingold, S. Ghan, A. B. Guenther, R. Kahn, I. Kraucunas, S. M. Kreidenweis, M. J. Molina, A. Nenes, J. E. Penner, K. A. Prather, V. Ramanathan, V. Ramaswamy, P. J. Rasch, A. R. Ravishankara, D. Rosenfeld, G. Stephens, and R. Wood. Improving our fundamental understanding of the role of aerosol-cloud interactions in the climate system. *Proceedings of the National Academy of Sciences*, 113(21):5781–5790, 2016.

[18] E. N. Lorenz. Section of planetary sciences: The predictability of hydrodynamic flow. *Transactions of the New York Academy of Sciences*, 25(4 Series II):409–432, 1963.

[19] N. Borduas and N. M. Donahue. The natural atmosphere. In *Green Chemistry*, pages 131–150. Elsevier, 2018.

[20] V. Ramanathan, R. D. Cess, E. F. Harrison, P. Minnis, B. R. Barkstorm, E. Ahmad, and D. Hartmann. Cloud-radiative forcing and climate: Results from the earth radiation budget experiment. *Science*, 243(4887):57–63, 1989.

[21] J. H. Seinfeld and S. N. Pandis. *Atmospheric chemistry and physics: from air pollution to climate change*, pages 6–9. John Wiley & Sons, 1998.

[22] J. H. Seinfeld and S. N. Pandis. *Atmospheric chemistry and physics: from air pollution to climate change*, pages 338–340. John Wiley & Sons, 1998.

[23] A. Zaragoza, M. M. Conde, J. R. Espinosa, C. Valeriani, C. Vega, and E. Sanz. Competition between ices ih and ic in homogeneous water freezing. *The Journal of Chemical Physics*, 143(13):134504, 2015.

[24] M. Volmer and A. Weber. Keimbildung in uebersaettigten gebilden. *Zeitschrift fÃ¼r Physikalische Chemie*, 119U(1), 1926.

[25] L. Farkas. Keimbildungsgeschwindigkeit in übersÃ¤ttigten dämpfen. *Zeitschrift fÃ¼r Physikalische Chemie*, 125U(1), 1927.

[26] R. Becker and W. Döring. Kinetische behandlung der keimbildung in Ã¼bersÃ¤ttigten daempfen. *Annalen der Physik*, 416(8):719–752, 1935.

[27] R. Eötvös. Über den zusammenhang der oberflächenspannung der flüssigkeiten mit ihrem molekularvolumen. *Annalen der Physik und Chemie*, 263(3):448–459, 1886.

[28] J. H. Seinfeld and S. N. Pandis. *Atmospheric chemistry and physics: from air pollution to climate change*, pages 545–595. John Wiley & Sons, 1998.

[29] J. H. Seinfeld and S. N. Pandis. *Atmospheric chemistry and physics: from air pollution to climate change*, pages 809–812. John Wiley & Sons, 1998.

[30] M. D. Petters and S. M. Kreidenweis. A single parameter representation of hygroscopic growth and cloud condensation nucleus activity. *Atmospheric Chemistry and Physics*, 7(8):1961–1971, 2007.

[31] D. A. Hegg and P. V. Hobbs. Cloud condensation nuclei in the marine atmosphere: A review. *Nucleation and atmospheric aerosols*, pages 181–192, 1992.

[32] J. H. Seinfeld and S. N. Pandis. *Atmospheric chemistry and physics: from air pollution to climate change*, pages 777–840. John Wiley & Sons, 1998.

[33] H. R. Pruppacher. A new look at homogeneous ice nucleation in supercooled water drops. *Journal of the Atmospheric Sciences*, 52(11):1924–1933, 1995.

[34] H. R. Pruppacher and J. D. Klett. *Microphysics of Clouds and Precipitation (pp. 287-360)*. Kluwer Academic Publishers, 1993.

[35] O. D. Robert, C. Marcolli, J. Fahrni, Y. Qiu, Y. A. Perez Sirkin, V. Molinero, F. Mahrt, D. Brühwiler, U. Lohmann, and Z. A. Kanji. Pore condensation and freezing is responsible for ice formation below water saturation for porous particles. *Proceedings of the National Academy of Sciences*, 116(17):8184–8189, 2019.

[36] N. Fukuta. Experimental studies of organic ice nuclei. *Journal of the Atmospheric Sciences*, 23(2):191–196, 1966.

[37] D. Niedermeier, R. A. Shaw, S. Hartmann, H. Wex, T. Clauss, J. VoigtlÃ¤nder, and F. Stratmann. Heterogeneous ice nucleation: exploring the transition from stochastic to singular freezing behavior. *Atmospheric Chemistry and Physics*, 11(16):8767–8775, 2011.

[38] A. V. Kajava and S. E. Lindow. A model of the three-dimensional structure of ice nucleation proteins. *Journal of Molecular Biology*, 232(3):709–717, 1993.

[39] B. G. Pummer, C. Budke, S. Augustin-Bauditz, D. Niedermeier, L. Felgitsch, C. J. Kampf, R. G. Huber, K. R. Liedl, T. Loerting, T. Moschen, M. Schauperl, M. Tollinger, C. E. Morris, H. Wex, H. Grothe, U. Poeschl, T. Koop, and J. Froehlich-Nowoisky. Ice nucleation by water-soluble macromolecules. *Atmospheric Chemistry and Physics*, 15(8):4077–4091, 2015.

[40] G. C. Sosso, T. F. Whale, M. A. Holden, P. Pedevilla, B. J. Murray, and A. Michaelides. Unravelling the origins of ice nucleation on organic crystals. *Chemical Science*, 9(42):8077–8088, 2018.

[41] J. H. Seinfeld and S. N. Pandis. *Atmospheric chemistry and physics: from air pollution to climate change*, pages 1113–1192. John Wiley & Sons, 1998.

[42] A. Gillard. On the terminology of biosphere and ecosphere. *Nature*, 223(5205):500–501, 1969.

[43] T. Gold. The deep, hot biosphere. *Proceedings of the National Academy of Sciences*, 89(13):6045–6049, 1992.

[44] Y. Yang, S. Itahashi, S. Yokobori, and A. Yamagishi. UV-resistant bacteria isolated from upper troposphere and lower stratosphere. *Biological Sciences in Space*, 22(1):18–25, 2008.

[45] N. R. Pace. A molecular view of microbial diversity and the biosphere. *Science*, 276(5313):734–740, 1997.

[46] K. Junge, C. Krembs, J. Deming, A. Stierle, and H. Eicken. A microscopic approach to investigate bacteria under in situ conditions in sea-ice samples. *Annals of Glaciology*, 33:304–310, 2001.

[47] E. J. Carpenter, S. Lin, and D. G. Capone. Bacterial activity in south pole snow. *Applied and Environmental Microbiology*, 66(10):4514–4517, 2000.

[48] S. H. Zhang, S. G. Hou, G. L. Yang, and J. H. Wang. Bacterial community in the east rongbuk glacier, mt. qomolangma (everest) by culture and culture-independent methods. *Microbiological Research*, 165(4):336–345, 2010.

[49] H.-C. Flemming and J. Wingender. The biofilm matrix. *Nature reviews microbiology*, 8(9):623–633, 2010.

[50] J. Fröhlich-Nowoisky, C. J. Kampf, B. Weber, J. A. Huffman, C. Poehlker, M. O. Andreae, N. Lang-Yona, S. M. Burrows, S. S. Gunthe, W. Elbert, H. Su, P. Hoor, E. Thines, T. Hoffmann, V. R. Despres, and U. Pöschl. Bioaerosols in the earth system: Climate, health, and ecosystem interactions. *Atmospheric Research*, 182:346–376, 2016.

[51] V. R. Després, J. A. Huffman, S. M. Burrows, C. Hoose, A. S. Safatov, G. Buryak, J. Fröhlich-Nowoisky, W. Elbert, M. O. Andreae, U. Pöschl, and R. Jaenicke. Primary biological aerosol particles in the atmosphere: a review. *Tellus B: Chemical and Physical Meteorology*, 64(1):15598, 2012.

[52] Y. S. Joung, Z. Ge, and C. R. Buie. Bioaerosol generation by raindrops on soil. *Nature Communications*, 8(1):1–10, 2017.

[53] C. Hoose, J. E. Kristjánsson, and S. M. Burrows. How important is biological ice nucleation in clouds on a global scale? *Environmental Research Letters*, 5(2):024009, 2010.

[54] C. Darwin. *On the origin of species: A facsimile of the first edition*. Harvard University Press, 1964.

[55] K. E. Zachariassen and E. Kristiansen. Ice nucleation and antinucleation in nature. *Cryobiology*, 41(4):257–279, 2000.

[56] A. Sakai and W. Larcher. *Frost survival of plants: responses and adaptation to freezing stress*, volume 62. Springer Science & Business Media, 1987.

[57] L. Felgitsch, P. Baloh, J. Burkart, M. Mayr, M. E. Momken, T. M. Seifried, P. Winkler, D. G. Schmale III, and H. Grothe. Birch leaves and branches as a source of ice-nucleating macromolecules. *Atmospheric Chemistry and Physics*, 18(21):16063–16079, 2018.

[58] L. Felgitsch, M. Bichler, J. Burkart, B. Fiala, T. Häusler, R. Hitzenberger, and H. Grothe. Heterogeneous freezing of liquid suspensions including juices and extracts from berries and leaves from perennial plants. *Atmosphere*, 10(1):37, 2019.

[59] S. E. Lindow, S. S Hirano, W. R. Barchet, D. C. Arny, and C. D. Upper. Relationship between ice nucleation frequency of bacteria and frost injury. *Plant physiology*, 70(4):1090–1093, 1982.

[60] A. T. Kunert, M. L. Pöhlker, K. Tang, K. S. Krevert, C. Wieder, K. R. Speth, L. E. Hanson, C. E. Morris, D. G. Schmale III, U. Pöschl, and J. Fröhlich-Nowoisky. Macromolecular fungal ice nuclei in fusarium: effects of physical and chemical processing. *Biogeosciences*, 16(23):4647–4659, 2019.

[61] W. C. Hinds. *Aerosol technology: properties, behavior, and measurement of airborne particles*, pages 1–13. John Wiley & Sons, 1999.

[62] W. C. Hinds. *Aerosol technology: properties, behavior, and measurement of airborne particles*, pages 42–73. John Wiley & Sons, 1999.

[63] P. H. McMurry. Aerosols observations and measurements. In *Encyclopedia of Atmospheric Sciences*, pages 53–65. Elsevier, 2015.

[64] M. Kalberer. Aerosol physics and chemistry. In *Encyclopedia of Atmospheric Sciences*, pages 23–31. Elsevier, 2015.

[65] J. Burkart, J. Gratzl, T. M. Seifried, P. Bieber, , and H. Grothe. Subpollen particles (spp) of birch as carriers of ice nucleating macromolecules. *Biogeoscience Discuss.*, [preprint], 2021. in review.

[66] K. Diehl, S. Matthias-Maser, R. Jaenicke, and S. K. Mitra. The ice nucleating ability of pollen: Part ii. laboratory studies in immersion and contact freezing modes. *Atmospheric Research*, 61(2):125–133, 2002.

[67] B. G. Pummer, H. Bauer, J. Bernardi, S. Bleicher, and H. Grothe. Suspendable macromolecules are responsible for ice nucleation activity of birch and conifer pollen. *Atmospheric Chemistry and Physics*, 12(5):2541–2550, 2012.

[68] P. E. Taylor, R. C. Flagan, A. G. Miguel, R. Valenta, and M. M. Glovsky. Birch pollen rupture and the release of aerosols of respirable allergens. *Clinical & Experimental Allergy*, 34(10):1591–1596, 2004.

[69] E. Gute and J. P. D. Abbatt. Ice nucleating behavior of different tree pollen in the immersion mode. *Atmospheric Environment*, 231:117488, 2020.

[70] T. M. Seifried, P. Bieber, L. Felgitsch, J. Vlasich, F. Reyzek, D. G. Schmale III, and H. Grothe. Surfaces of silver birch (betula pendula) are sources of biological ice nuclei: In-vivo and in-situ investigationssurfaces of silver birch (betula pendula) are sources of biological ice nuclei: In-vivo and in-situ investigations. *Biogeoscience*, 2020.

[71] J. Fröhlich-Nowoisky, D. A. Pickersgill, V. R. Despres, and U. Pöschl. High diversity of fungi in air particulate matter. *Proceedings of the National Academy of Sciences*, 106(31):12814–12819, 2009.

[72] S. Calhim, P. Halme, J. H. Petersen, T. Læssøe, C. Bössler, and J. Heilmann-Clausen. Fungal spore diversity reflects substrate-specific deposition challenges. *Scientific Reports*, 8(1):1–9, 2018.

[73] S. Pouleur, C. Richard, J.-G. Martin, and H. Antoun. Ice nucleation activity in fusarium acuminatum and fusarium avenaceum. *Applied and Environmental Microbiology*, 58(9):2960–2964, 1992.

[74] J. Fröhlich-Nowoisky, T. C. J. Hill, B. G. Pummer, G. D. Franc, and U. Pöschl. Ice nucleation activity in the widespread soil fungus mortierella alpina. *Biogeosciences Discussions*, 11(8):12697–12731, 2014.

[75] D. I. Haga, R. Iannone, M. J. Wheeler, R. Mason, E. A. Polishchuk, T. Fetch, B. J. van der Kamp, I. G. McKendry, and A. K. Bertram. Ice nucleation properties of rust and bunt fungal spores and their transport to high altitudes, where they can cause heterogeneous freezing. *Journal of Geophysical Research: Atmospheres*, 118(13):7260–7272, 2013.

[76] P. K. Wolber. Bacterial ice nucleation. *Advances in microbial physiology*, 34:203–203, 1993.

[77] Y. Vasebi, M. E. Mechan Llontop, R. Hanlon, D. G. Schmale III, R. Schnell, and B. A. Vinatzer. Comprehensive characterization of an aspen (populus tremuloides) leaf litter sample that maintained ice nucleation activity for 48 years. *Biogeosciences*, 16(8):1675–1683, 2019.

[78] H. Bauer, A. Kasper-Giebl, M. Löflund, H. Giebl, R. Hitzenberger, F. Zibuschka, and H. Puxbaum. The contribution of bacteria and fungal spores to the organic carbon content of cloud water, precipitation and aerosols. *Atmospheric Research*, 64(1-4):109–119, 2002.

[79] A. M. Womack, B. J. M. Bohannan, and J. L. Green. Biodiversity and biogeography of the atmosphere. *Philosophical Transactions of the Royal Society B: Biological Sciences*, 365(1558):3645–3653, 2010.

[80] R. B. Pietsch, B. A. Vinatzer, and D. G. Schmale III. Diversity and abundance of ice nucleating strains of pseudomonas syringae in a freshwater lake in virginia, USA. *Frontiers in Microbiology*, 8, 2017.

[81] J. Benson, R. Hanlon, T. Seifried, P. Baloh, C. Powers, H. Grothe, and D. G. Schmale III. Microorganisms collected from the surface of freshwater lakes using a drone water sampling system (DOWSE). *Water*, 11(1):157, 2019.

[82] P. Baloh, N. Els, R. O. David, C. Larose, K. Whitmore, B. Sattler, and H. Grothe. Assessment of artificial and natural transport mechanisms of ice nucleating particles in an alpine ski resort in obergurgl, austria. *Frontiers in Microbiology*, 10, 2019.

[83] C. L. Monteil, M. Bardin, and C. E. Morris. Features of air masses associated with the deposition of pseudomonas syringae and botrytis cinerea by rain and snowfall. *The ISME Journal*, 8(11):2290–2304, 2014.

[84] M. Joly, E. Attard, M. Sancelme, L. Deguillaume, C. Guilbaud, C. E. Morris, P. Amato, and A.-M. Delort. Ice nucleation activity of bacteria isolated from cloud water. *Atmospheric Environment*, 70:392–400, 2013.

[85] D. V. Spracklen and C. L. Heald. The contribution of fungal spores and bacteria to regional and global aerosol number and ice nucleation immersion freezing rates. *Atmospheric Chemistry and Physics*, 14(17):9051–9059, 2014.

[86] C. A. Suttle. Viruses in the sea. *Nature*, 437(7057):356–361, 2005.

[87] T. W. Whon, M.-S. Kim, S. W. Roh, N.-R. Shin, H.-W. Lee, and J.-W. Bae. Metagenomic characterization of airborne viral DNA diversity in the near-surface atmosphere. *Journal of Virology*, 86(15):8221–8231, 2012.

[88] J. Y. Aller, M. R. Kuznetsova, C. J. Jahns, and P. F. Kemp. The sea surface microlayer as a source of viral and bacterial enrichment in marine aerosols. *Journal of Aerosol Science*, 36(5-6):801–812, 2005.

[89] K. Junge and B. D. Swanson. High-resolution ice nucleation spectra of sea-ice bacteria: implications for cloud formation and life in frozen environments. *Biogeosciences*, 5(3):865–873, 2008.

[90] I. Reche, G. D'Orta, N. Mladenov, D. M. Winget, and C. A. Suttle. Deposition rates of viruses and bacteria above the atmospheric boundary layer. *The ISME Journal*, 12(4):1154–1162, 2018.

[91] F. Conen, C. E. Morris, J. Leifeld, M. V. Yakutin, and C. Alewell . Biological residues define the ice nucleation properties of soil dust. *Atmospheric Chemistry and Physics*, 11(18):9643–9648, 2011.

[92] D. O/Sullivan, B. J. Murray, J. F. Ross, T. F. Whale, H. C. Price, J. D. Atkinson, N. S. Umo, and M. E. Webb. The relevance of nanoscale biological fragments for ice nucleation in clouds. *Scientific Reports*, 5(1), 2015.

[93] M. Shiraiwa, L. D. Yee, K. A. Schilling, C. L. Loza, J. S. Craven, A. Zuend, P. J. Ziemann, and J. H. Seinfeld. Size distribution dynamics reveal particle-phase chemistry in organic aerosol formation. *Proceedings of the National Academy of Sciences*, 110(29):11746–11750, 2013.

[94] A. G. Carlton, C. Wiedinmyer, and J. H. Kroll. A review of secondary organic aerosol (SOA) formation from isoprene. *Atmospheric Chemistry and Physics*, 9(14):4987–5005, 2009.

[95] M. Hallquist, J. C. Wenger, U. Baltensperger, Y. Rudich, D. Simpson, M. Claeys, J. Dommen, N. M. Donahue, C. George, A. H. Goldstein, J. F. Hamilton, H. Herrmann, T. Hoffmann, Y. Iinuma, M. Jang, M. E. Jenkin, J. L. Jimenez, A. Kiendler-Scharr, W. Maenhaut, G. McFiggans, Th. F. Mentel, A. Monod, A. S. H. Prévôt, J. H. Seinfeld, J. D. Surratt, R. Szmigielski, and J. Wildt. The formation, properties and impact of secondary organic aerosol: current and emerging issues. *Atmospheric Chemistry and Physics*, 9(14):5155–5236, 2009.

[96] A. Limbeck. Secondary organic aerosol formation in the atmosphere via heterogeneous reaction of gaseous isoprene on acidic particles. *Geophysical Research Letters*, 30(19), 2003.

[97] J. K. Holopainen and J. Gershenzon. Multiple stress factors and the emission of plant VOCs. *Trends in Plant Science*, 15(3):176–184, 2010.

[98] M. O. Andreae. Atmospheric aerosols: Biogeochemical sources and role in atmospheric chemistry. *Science*, 276(5315):1052–1058, 1997.

[99] J. Ofner, H.-U. Krüger, H. Grothe, P. Schmitt-Kopplin, K. Whitmore, and C. Zetzsch. Physico-chemical characterization of SOA derived from catechol and guaiacol a model substance for the aromatic fraction of atmospheric HULIS. *Atmospheric Chemistry and Physics*, 11(1):1–15, 2011.

[100] B. Wang, A. T. Lambe, P. Massoli, T. B. Onasch, P. Davidovits, D. R. Worsnop, and D. A. Knopf. The deposition ice nucleation and immersion freezing potential of amorphous secondary organic aerosol: Pathways for ice and mixed-phase cloud formation. *Journal of Geophysical Research: Atmospheres*, 117(D16):n/a–n/a, 2012.

[101] A. J. Prenni, M. D. Petters, S. M. Kreidenweis, C. L. Heald, S. T Martin, P. Artaxo, R. M. Garland, A. G. Wollny, and Ulrich Poeschl. Relative roles of biogenic emissions and saharan dust as ice nuclei in the amazon basin. *Nature Geoscience*, 2(6):402–405, 2009.

[102] W. J. Ripple, C. Wolf, T. M. Newsome, P. Barnard, and W. R. Moomaw. World scientists' warning of a climate emergency. *BioScience*, 2019.

[103] A. Arneth, F. Denton, F. Agus, A. Elbehri, K. H. Erb, B. O. Elasha, M. Rahimi, M. Rounsevell, A. Spence, R. Valentini, et al. Framing and context. In *Climate Change and Land: an IPCC special report on climate change, desertification, land degradation, sustainable land management, food security, and greenhouse gas fluxes in terrestrial ecosystems*, pages 1–98. Intergovernmental Panel on Climate Change (IPCC), 2019.

[104] M.R. Allen, O.P. Dube, W. Solecki, F. Aragon-Durand, W. Cramer, S. Humphreys, M. Kainuma, J. Kala, N. Mahowald, Y. Mulugetta, R. Perez, M.Wairiu, , and K. Zickfeld. Framing and context. In *Framing and Context. In: Global Warming of 1.5°C. An IPCC Special Report on the impacts of global warming of 1.5Â °C above pre-industrial levels and related global greenhouse gas emission pathways, in the context of strengthening the global response to the threat of climate change, sustainable development, and efforts to eradicate poverty*, pages 49—91. Intergovernmental Panel on Climate Change (IPCC), 2018.

[105] A. J. Hansen, R. P. Neilson, V. H. Dale, C. H. Flather, L. R. Iverson, D. J. Currie, S. Shafer, R. Cook, and P. J. Bartlein. Global change in forests: Responses of species, communities, and biomes. *BioScience*, 51(9):765, 2001.

[106] A. Gobiet, S. Kotlarski, M. Beniston, G Heinrich, J. Rajczak, and M. Stoffel. 21st century climate change in the european alps—a review. *Science of The Total Environment*, 493:1138–1151, 2014.

[107] O. Boucher, D. Randall, P. Artaxo, C. Bretherton, G. Feingold, P. Forster, V.-M. Kerminen, Y. Kondo, H. Liao, U. Lohmann, et al. Clouds and aerosols. In *Climate change 2013: the physical science basis. Contribution of Working Group I to the Fifth*

Assessment Report of the Intergovernmental Panel on Climate Change, pages 571–657. Cambridge University Press, 2013.

[108] K. S. Carslaw, L. A. Lee, C. L. Reddington, K. J. Pringle, A. Rap, P. M. Forster, G. W. Mann, D. V. Spracklen, M. T. Woodhouse, L. A. Regayre, and J. R. Pierce. Large contribution of natural aerosols to uncertainty in indirect forcing. *Nature*, 503(7474):67–71, 2013.

[109] U. Pöschl, S. T. Martin, B. Sinha, Q. Chen, S. S. Gunthe, J. A. Huffman, S. Borrmann, D. K. Farmer, R. M. Garland, G. Helas, J. L. Jimenez, S. M. King, A. Manzi, E. Mikhailov, T. Pauliquevis, M. D. Petters, A. J. Prenni, P. Roldin, D. Rose, J. Schneider, H. Su, S. R. Zorn, P. Artaxo, and M. O. Andreae. Rainforest aerosols as biogenic nuclei of clouds and precipitation in the amazon. *Science*, 329(5998):1513–1516, 2010.

[110] J. A. Huffman, A. J. Prenni, P. J. DeMott, C. Pöhlker, R. H. Mason, N. H. Robinson, J. Fröhlich-Nowoisky, Y. Tobo, V. R. Després, E. Garcia, D. J. Gochis, E. Harris, I. Müller-Germann, C. Ruzene, B. Schmer, B. Sinha, D. A. Day, M. O. Andreae, J. L. Jimenez, M. Gallagher, S. M. Kreidenweis, A. K. Bertram, and U. Pöschl. High concentrations of biological aerosol particles and ice nuclei during and after rain. *Atmospheric Chemistry and Physics*, 13(13):6151–6164, 2013.

[111] K. A. Pratt, P. J. DeMott, J. R. French, Z. Wang, D. L. Westphal, A. J. Heymsfield, C .H. Twohy, A. J. Prenni, and K. A. Prather. In situ detection of biological particles in cloud ice-crystals. *Nature Geoscience*, 2(6):398–401, 2009.

[112] J. Wang, R. Krejci, S. Giangrande, C. Kuang, H. M. J. Barbosa, J. Brito, S. Carbone, X. Chi, J. Comstock, F. Ditas, J. Lavric, H. E. Manninen, F. Mei, D. Moran-Zuloaga, C. Pöhlker, M. L. Pöhlker, J. Saturno, B. Schmid, R. A. F. Souza, S. R. Springston, J. M. Tomlinson, T. Toto, D. Walter, D. Wimmer, J. N. Smith, M. Kulmala, L. A. T. Machado, P. Artaxo, M. O. Andreae, T. Petäjä, and S. T. Martin. Amazon boundary layer aerosol concentration sustained by vertical transport during rainfall. *Nature*, 539(7629):416–419, 2016.

[113] C. W. Powers, R. Hanlon, H. Grothe, A. J. Prussin, L. C. Marr, and D. G. Schmale III. Coordinated sampling of microorganisms over freshwater and saltwater environments using an unmanned surface vehicle (USV) and a small unmanned aircraft system (sUAS). *Frontiers in Microbiology*, 9:1668, 2018.

[114] M. T. Chiliński, K. M. Markowicz, and M. Kubicki. Uas as a support for atmospheric aerosols research: Case study. In *Pageoph Topical Volumes*, pages 185–202. Springer International Publishing, oct 2018.

[115] D. G. Schmale III, B. R. Dingus, and C. Reinholtz. Development and application of an autonomous unmanned aerial vehicle for precise aerobiological sampling above agricultural fields. *Journal of Field Robotics*, 25(3):133–147, 2008.

[116] B. Lin, A. Bozorgmagham, S. D. Ross, and D. G. Schmale III. Small fluctuations in the recovery of fusaria across consecutive sampling intervals with unmanned aircraft 100 m above ground level. *Aerobiologia*, 29(1):45–54, 2012.

[117] B. Lin, S. D. Ross, A. J. Prussin, and D. G. Schmale III. Seasonal associations and atmospheric transport distances of fungi in the genus fusarium collected with unmanned aerial vehicles and ground-based sampling devices. *Atmospheric Environment*, 94:385–391, 2014.

[118] C. Jimenez-Sanchez, R. Hanlon, K. A. Aho, C. Powers, C. E. Morris, and D. G. Schmale III. Diversity and ice nucleation activity of microorganisms collected with a small unmanned aircraft system (sUAS) in france and the united states. *Frontiers in Microbiology*, 9, 2018.

[119] C. Crazzolara, M. Ebner, A. Platis, T. Miranda, J. Bange, and A. Junginger. A new multicopter-based unmanned aerial system for pollen and spores collection in the atmospheric boundary layer. *Atmospheric Measurement Techniques*, 12(3):1581–1598, 2019.

[120] P. Bieber, T. M. Seifried, J. Burkart, J. Gratzl, A. Kasper-Giebl, D. G. Schmale III, and H. Grothe. A drone-based bioaerosol sampling system to monitor ice nucleation particles in the lower atmosphere. *Remote Sensing*, 12(3):552, 2020.

[121] W. C. Hinds. *Aerosol technology: properties, behavior, and measurement of airborne particles*, pages 111–140. John Wiley & Sons, 1999.

[122] W. C. Hinds. *Aerosol technology: properties, behavior, and measurement of airborne particles*, pages 206–231. John Wiley & Sons, 1999.

[123] T. M. Seifried, P. Bieber, A. T. Kunert, D. G. Schmale III, K. Whitmore, J. Fröhlich-Nowoisky, and Hinrich Grothe. Ice nucleation activity of alpine bioaerosol emitted in vicinity of a birch forest. *Atmosphere*, 12(6):779, 2021.

[124] S. M. Kang, K. J. Heo, and B. U. Lee. Why does rain increase the concentrations of environmental bioaerosols during monsoon? *Aerosol and Air Quality Research*, 15(6):2320–2324, 2015.

[125] T. P. Wright, J. D. Hader, G. R. McMeeking, and M. D. Petters. High relative humidity as a trigger for widespread release of ice nuclei. *Aerosol Science and Technology*, 48(11):i–v, 2014.

[126] A. T. Kunert, M. Lamneck, F. Helleis, U.h Pöschl, M. L. Pöhlker, and J. Fröhlich-Nowoisky. Twin-plate ice nucleation assay (TINA) with infrared detection for high-throughput droplet freezing experiments with biological ice nuclei in laboratory and field samples. *Atmospheric Measurement Techniques*, 11(11):6327–6337, 2018.

[127] G. Vali. Quantitative evaluation of experimental results an the heterogeneous freezing nucleation of supercooled liquids. *Journal of the Atmospheric Sciences*, 28(3):402–409, 1971.

[128] R. O. David, M. Cascajo-Castresana, K. P. Brennan, M. Roesch, N. Els, J. Werz, V. Weichlinger, L. S. Boynton, S. Bogler, N. Borduas-Dedekind, C. Marcolli, and Z. A. Kanji. Development of the droplet ice nuclei counter zurich (DRINCZ): validation and application to field-collected snow samples. *Atmospheric Measurement Techniques*, 12(12):6865–6888, 2019.

[129] C. Pöhlker, J. A. Huffman, and U. Pöschl. Autofluorescence of atmospheric bioaerosols – fluorescent biomolecules and potential interferences. *Atmospheric Measurement Techniques*, 5(1):37–71, 2012.

[130] J. R. Lakowicz. *Principles of fluorescence spectroscopy*. Springer science & business media, 2006.

[131] J. W. Lichtman and J.-A. Conchello. Fluorescence microscopy. *Nature methods*, 2(12):910–919, 2005.

[132] L. Reimer. Scanning electron microscopy: physics of image formation and microanalysis, 2000.

[133] B. J. Inkson. Scanning electron microscopy (sem) and transmission electron microscopy (tem) for materials characterization. In *Materials characterization using nondestructive evaluation (NDE) methods*, pages 17–43. Elsevier, 2016.

[134] J. .I Goldstein, D. E. Newbury, J. R. Michael, N. W. Ritchie, J. H. J. Scott, and D. C. Joy. *Scanning electron microscopy and X-ray microanalysis*. Springer, 2017.

[135] Y. Tobo, A. J. Prenni, P. J. DeMott, J. A. Huffman, C. S. McCluskey, G. Tian, C. Pöhlker, U. Pöschl, and S. M. Kreidenweis. Biological aerosol particles as a key determinant of ice nuclei populations in a forest ecosystem. *Journal of Geophysical Research: Atmospheres*, 118(17):10,100–10,110, 2013.

[136] C. M. Rathnayake, N. Metwali, T. Jayarathne, J. Kettler, Y. Huang, P. S. Thorne, P. T. O'Shaughnessy, and E. A. Stone. Influence of rain on the abundance of bioaerosols in fine and coarse particles. *Atmospheric Chemistry and Physics*, 17(3):2459–2475, 2017.

[137] K. J. Heo, H. B. Kim, and B. U. Lee. Concentration of environmental fungal and bacterial bioaerosols during the monsoon season. *Journal of Aerosol Science*, 77:31–37, 2014.

[138] C. E. Morris, F. Conen, J. A. Huffman, V. Phillips, U. Pöschl, and D. C. Sands. Bioprecipitation: a feedback cycle linking earth history, ecosystem dynamics and land use

through biological ice nucleators in the atmosphere. *Global Change Biology*, 20(2):341–351, 2013.

[139] Z. Liu, L. Shen, C. Yan, J. Du, Y. Li, and H. Zhao. Analysis of the influence of precipitation and wind on PM2.5 and PM10 in the atmosphere. *Advances in Meteorology*, 2020:1–13, 2020.

[140] D.M. Chate and T.S. Pranesha. Field studies of scavenging of aerosols by rain events. *Journal of Aerosol Science*, 35(6):695–706, 2004.

[141] M. Niemand, O. Möhler, B. Vogel, H. Vogel, C. Hoose, P. Connolly, H. Klein, H. Bingemer, P. DeMott, J. Skrotzki, and T. Leisner. A particle-surface-area-based parameterization of immersion freezing on desert dust particles. *Journal of the Atmospheric Sciences*, 69(10):3077–3092, 2012.

[142] T. Häusler, P. Gebhardt, D. Iglesias, C. Rameshan, S. Marchesan, D. Eder, and H. Grothe. Ice nucleation activity of graphene and graphene oxides. *The Journal of Physical Chemistry C*, 122(15):8182–8190, 2018.

[143] C. S. McCluskey, J. Ovadnevaite, M. Rinaldi, J. Atkinson, F. Belosi, D. Ceburnis, S. Marullo, T. C. J. Hill, U. Lohmann, Z. A. Kanji, C. O'Dowd, S. M. Kreidenweis, and P. J. DeMott. Marine and terrestrial organic ice-nucleating particles in pristine marine to continentally influenced northeast atlantic air masses. *Journal of Geophysical Research: Atmospheres*, 123(11):6196–6212, 2018.

[144] C. S. McCluskey, T. C. J. Hill, F. Malfatti, C. M. Sultana, C. Lee, M. V. Santander, C. M. Beall, K. A. Moore, G. C. Cornwell, D. B. Collins, K. A. Prather, T. Jayarathne, E. A. Stone, F. Azam, S. M. Kreidenweis, and P. J. DeMott. A dynamic link between ice nucleating particles released in nascent sea spray aerosol and oceanic biological activity during two mesocosm experiments. *Journal of the Atmospheric Sciences*, 74(1):151–166, 2017.

[145] G. C. E. Porter, S. N. F. Sikora, M. P. Adams, U. Proske, A. D. Harrison, M. D. Tarn, I. M. Brooks, and B. J. Murray. Resolving the size of ice-nucleating particles with a balloon deployable aerosol sampler: the SHARK. *Atmospheric Measurement Techniques*, 13(6):2905–2921, 2020.

[146] J. M. Creamean, C. Mignani, N. Bukowiecki, and F. Conen. Using freezing spectra characteristics to identify ice-nucleating particle populations during the winter in the alps. *Atmospheric Chemistry and Physics*, 19(12):8123–8140, 2019.

[147] L. Lacher, U. Lohmann, Y. Boose, A. Zipori, E. Herrmann, N. Bukowiecki, M. Steinbacher, and Z. A. Kanji. The horizontal ice nucleation chamber (hinc): Inp measurements at conditions relevant for mixed-phase clouds at the high altitude research station jungfraujoch. pages 15199–15224, 2017.

[148] S. Yadav, R. E. Venezia, R. W. Paerl, and M. D. Petters. Characterization of ice-nucleating particles over northern india. *Journal of Geophysical Research: Atmospheres*, 124(19):10467–10482, 2019.

[149] K. Bi, G. R. McMeeking, D. P. Ding, E. J. T. Levin, P. J. DeMott, D. L. Zhao, F. Wang, Q. Liu, P. Tian, X. C. Ma, Y. B. Chen, M. Y. Huang, H. L. Zhang, T. D. Gordon, and P. Chen. Measurements of ice nucleating particles in beijing, china. *Journal of Geophysical Research: Atmospheres*, 124(14):8065–8075, 2019.

[150] J. Chen, Z. Wu, S. Augustin-Bauditz, S. Grawe, M. Hartmann, X. Pei, Z. Liu, D. Ji, and H. Wex. Ice-nucleating particle concentrations unaffected by urban air pollution in beijing, china. *Atmospheric Chemistry and Physics*, 18(5):3523–3539, 2018.

[151] T. R. Rockett and C. L. Kramer. Periodicity and total spore production by lignicolous basidiomycetes. *Mycologia*, 66(5):817–829, 1974.

[152] K. Jayaweera and P. Flanagan. Investigations on biogenic ice nuclei in the arctic atmosphere. *Geophysical Research Letters*, 9(1):94–97, 1982.

[153] C. Hoose and O. Möhler. Heterogeneous ice nucleation on atmospheric aerosols: a review of results from laboratory experiments. *Atmospheric Chemistry and Physics*, 12(20):9817–9854, 2012.

[154] H. J. Lee, A. Laskin, J. Laskin, and S. A. Nizkorodov. Excitation-emission spectra and fluorescence quantum yields for fresh and aged biogenic secondary organic aerosols. *Environmental Science & Technology*, 47(11):5763–5770, 2013.

[155] C. Pöhlker, J. A. Huffman, J.-D. Förster, and U. Pöschl. Autofluorescence of atmospheric bioaerosols: spectral fingerprints and taxonomic trends of pollen. *Atmospheric Measurement Techniques*, 6(12):3369–3392, 2013.

[156] S. C. Hill, Y.-L. Pan, C. Williamson, J. L. Santarpia, and H. H. Hill. Fluorescence of bioaerosols: mathematical model including primary fluorescing and absorbing molecules in bacteria. *Optics Express*, 21(19):22285, 2013.

[157] D. A. Healy, J. A. Huffman, D. J. O'Connor, C. Pöhlker, U. Pöschl, and J. R. Sodeau. Ambient measurements of biological aerosol particles near killarney, ireland: a comparison between real-time fluorescence and microscopy techniques. *Atmospheric Chemistry and Physics*, 14(15):8055–8069, 2014.

[158] E. Levetin. Identification and concentration of airborne basidiospores. *Grana*, 30(1):123–128, 1991.

[159] I. Hosen and T.-H. Li. Two new species of phylloporus from bangladesh, with morphological and molecular evidence. *Mycologia*, 109(2):277–286, 2017.

[160] A. E. Valsan, R. Ravikrishna, C. V. Biju, C. Pöhlker, V. R. Després, J. A. Huffman, U. Pöschl, and S. S. Gunthe. Fluorescent biological aerosol particle measurements at a tropical high-altitude site in southern india during the southwest monsoon season. *Atmospheric Chemistry and Physics*, 16(15):9805–9830, 2016.

[161] A. S. Sánchez-López, M. González-Chávez, A. Del Carmen, F. A. Solís-Domínguez, R. Carrillo-González, and G. H. Rosas-Saito. Leaf epiphytic bacteria of plants colonizing mine residues: Possible exploitation for remediation of air pollutants. *Frontiers in Microbiology*, 9, 2018.

[162] R. Agnihotri, S. K. Mishra, P. Yadav, S. Singh, R. Rashmi, M.V.S.N. Prasad, C. Sharma, and B. C. Arya. Bulk level to individual particle level chemical composition of atmospheric dust aerosols (PM5) over a semi-arid urban zone of western india (rajasthan). *Aerosol and Air Quality Research*, 15(1):58–71, 2015.

[163] D. W. Anthony, H. C. Chapman, and E. I. Hazard. Scanning electron microscopy of the sporangia of species of coelomomyces (blastocladiales: Coelomomycetaceae). *Journal of Invertebrate Pathology*, 17(3):395–403, 1971.

[164] P. Heikkilä, M. Kotimaa, T. Tuomi, T. Salmi, and K. Louhelainen. Identification and counting of fungal spores by scanning electron microscope. *The Annals of Occupational Hygiene*, 1988.

[165] C. D. O'Dowd, M. H. Smith, I. E. Consterdine, and J. A. Lowe. Marine aerosol, sea-salt, and the marine sulphur cycle: a short review. *Atmospheric Environment*, 31(1):73–80, 1997.

[166] P. Aalto, K. Hämeri, E. Becker, R. Weber, J. Salm, J. M. Mäkelä, C. Hoell, C. D. O'dowd, H. Hansson, M. VÃ¤kevÃ¤, I. K. Koponen, G. Buzorius, and M. Kulmala. Physical characterization of aerosol particles during nucleation events. *Tellus B: Chemical and Physical Meteorology*, 53(4):344–358, 2001.

[167] M. Kulmala, A. Luoma, K.and Virkkula, T. Petäjä, P. Paasonen, V. Kerminen, W. Nie, X. Qi, Y. Shen, X. Chi, et al. On the mode-segregated aerosol particle number concentration load: contributions of primary and secondary particles in hyytiälä and nanjing. *Boreal Environment Research*, 2016.

[168] S. Nyeki, F. Li, E. Weingartner, N. Streit, I. Colbeck, H. W. Gaeggeler, and U. Baltensperger. The background aerosol size distribution in the free troposphere: An analysis of the annual cycle at a high-alpine site. *Journal of Geophysical Research: Atmospheres*, 103(D24):31749–31761, 1998.

[169] P. Hegde, P. Pant, M. Naja, U. C. Dumka, and R. Sagar. South asian dust episode in june 2006: Aerosol observations in the central himalayas. *Geophysical Research Letters*, 34(23), 2007.

[170] P. Shrestha, A. P. Barros, and A. Khlystov. Chemical composition and aerosol size distribution of the middle mountain range in the nepal himalayas during the 2009 pre-monsoon season. *Atmospheric Chemistry and Physics*, 10(23):11605–11621, 2010.

[171] Z. Wu, M. Hu, P. Lin, S. Liu, B. Wehner, and A. Wiedensohler. Particle number size distribution in the urban atmosphere of beijing, china. *Atmospheric Environment*, 42(34):7967–7980, 2008.

[172] J. A. Huffman, B. Sinha, R. M. Garland, A. Snee-Pollmann, S. S. Gunthe, P. Artaxo, S. T. Martin, M. O. Andreae, and U. Pöschl. Size distributions and temporal variations of biological aerosol particles in the amazon rainforest characterized by microscopy and real-time UV-APS fluorescence techniques during AMAZE-08. *Atmospheric Chemistry and Physics*, 12(24):11997–12019, 2012.

[173] D. I. Haga, S. M. Burrows, R. Iannone, M. J. Wheeler, R. H. Mason, J. Chen, E. A. Polishchuk, U. Pöschl, and A. K. Bertram. Ice nucleation by fungal spores from the classes agaricomycetes, ustilaginomycetes, and eurotiomycetes, and the effect on the atmospheric transport of these spores. *Atmospheric Chemistry and Physics*, 14(16):8611–8630, 2014.

[174] K.-F. Chang and P. V. Blenis. Survival of endocronartium harknessii teliospores in a simulated airborne state. *Canadian Journal of Botany*, 67(3):928–932, 1989.

[175] L. A. Bulla, G. S. Julian, R. A. Rhodes, and C. W. Hesseltine. Scanning electron and phase-contrast microscopy of bacterial spores. *Applied microbiology*, 18(3):490–495, 1969.